

# **Focusing of Electromagnetic Waves**

by

S.H. Wiersma



VRIJE UNIVERSITEIT

**Focusing of Electromagnetic Waves**

ACADEMISCH PROEFSCHRIFT

ter verkrijging van de graad van doctor aan  
de Vrije Universiteit te Amsterdam,  
op gezag van de rector magnificus  
prof. dr. T. Sminia,  
in het openbaar te verdedigen  
ten overstaan van de promotiecommissie  
van de faculteit der exacte wetenschappen\ natuurkunde en sterrenkunde  
op donderdag 7 september 2000 om 13.45 uur  
in het hoofdgebouw van de universiteit,  
De Boelelaan 1105

door

**Sjoerd Haije Wiersma**

geboren te Haarlemmermeer

Promotor: prof. dr. D. Lenstra  
Copromotor: dr. T.D. Visser

*Aan mijn familie*



# Contents

<b>1</b>	<b>Introduction</b>	<b>1</b>
1.1	Scalar diffraction theory . . . . .	2
1.2	Vectorial focusing theory . . . . .	9
1.3	The structure of this thesis . . . . .	10
<b>2</b>	<b>Defocusing of a converging electromagnetic wave by a plane dielectric interface</b>	<b>15</b>
2.1	Introduction . . . . .	16
2.2	The field on the interface . . . . .	18
2.3	The m-theory . . . . .	22
2.4	The diffraction integral . . . . .	26
2.5	Results . . . . .	28
2.6	Conclusions . . . . .	32
<b>3</b>	<b>Comparison of different theories for focusing through a plane interface</b>	<b>35</b>
3.1	Introduction . . . . .	36
3.2	The electric vector in the second medium . . . . .	37
3.3	The diffraction optics solutions . . . . .	39
3.3.1	Plane wave solution . . . . .	39
3.3.2	The m-theory solution . . . . .	41
3.4	The geometrical optics approximation . . . . .	44
3.5	Numerical results . . . . .	46
3.6	Consequences for 3-D imaging . . . . .	50
3.7	Conclusions . . . . .	52

<b>4</b>	<b>Annular focusing through a dielectric interface: Scanning and confining the intensity</b>	<b>53</b>
4.1	Introduction . . . . .	54
4.2	The effect of an interface on an unobscured focused beam . . . . .	55
4.3	Stationary phase and geometrical optics . . . . .	57
4.4	Annular illumination: Localizing the intensity . . . . .	60
4.5	Conclusions . . . . .	64
<b>5</b>	<b>Reflection-induced spectral changes of the pulsed radiation emitted by a point source. Part I: Theory</b>	<b>69</b>
5.1	Introduction . . . . .	70
5.2	Description of the configuration . . . . .	71
5.3	The modified Cagniard method . . . . .	74
5.4	The reflected wave in $\mathcal{D}_1$ . . . . .	78
5.5	The on-axis response . . . . .	85
<b>6</b>	<b>Reflection-induced spectral changes of the pulsed radiation emitted by a point source. Part II: Application</b>	<b>89</b>
6.1	Introduction . . . . .	90
6.2	Numerical results . . . . .	90
6.3	Conclusions . . . . .	98
	<b>Bibliography</b>	<b>99</b>
	<b>Samenvatting (summary in Dutch)</b>	<b>107</b>
	<b>Dankwoord</b>	<b>111</b>

# Chapter 1

## Introduction

The theory of the focusing of light, though rich in history, generally assumes an important idealization, namely that the focusing takes place in a homogeneous portion of space. In practice, however, the focusing will typically be from air into a dielectric medium. When an electromagnetic wave is focused into a medium with different dielectric properties, i.e. when there is an interface between the lens which produces a converging spherical wave and the point of observation, the intensity distribution will be altered. Knowledge of this intensity distribution in the focal region is of great interest for many practical purposes. In, for example, optical recording and lithography one would like to have a well-defined intensity peak with a high maximum; for optical trapping knowledge of the shape of the intensity distribution is of prime importance. For three-dimensional microscopy an optimal resolution in the direction of the optical axis is desired. Also, the intensity distribution needs to be scanned along that axis.

This thesis provides an answer to questions like: “To what extent does the second medium impair the sharpness of the focal intensity distribution?”, “Is there a way to minimize this degradation?”, and “How can an optimized intensity distribution be scanned through the second medium?”. As will be seen, the use of a fully vectorial diffraction theory to analyze the electromagnetic field in the focal region is required if it is to describe the features of the diffracted field in high aperture angle systems.

In the following section the various ingredients of diffraction theory will be described starting with scalar theory, which for many diffraction problems is a sufficiently accurate model. However, the particular focus-

ing problems that are the subject of this thesis require the development of a vectorial theory, as described in Section 1.2.

Apart from focusing through a dielectric interface, this thesis also treats another effect of the presence of such an interface: namely, the spectral changes of a propagating wave emitted by a pulsed point source upon reflection at a half-space.

## 1.1 Scalar diffraction theory

To put the subject of this thesis into perspective we give a short outline of the main contributions to scalar diffraction theory.

A wave theory of light was first formulated in the seventeenth century [HUYGENS, 1690]: *But we must also investigate in more detail the origin of these waves and the way in which they propagate. Just like in the flame of a candle where one can distinguish the points A, B and C; the concentric circles around each of those points represent the waves which emanate from those points. First it follows from what has been said about the production of light that each little part of a luminous body like the Sun, a candle or an ember, emits waves from which it is the centre. And one should picture this likewise for each point of the surface and a part of the interior of that flame.* [translated by SHW]<sup>1</sup> (see Fig. 1.1). In modern-day terminology this is phrased as: *Each element of a wave front may be regarded as the center of a secondary disturbance which gives rise to spherical wavelets. The position of the wave front at any later time is the envelope of all such wavelets* [BORN AND WOLF, 1999]. We note that the concept of a wavelength was not yet part of Huygens' ideas.

Because of the monumental stature of Newton, who formulated his rival corpuscular theory of light, it took around one century before the wave theory was taken up again. Fresnel and Young greatly improved the predictivity of Huygens' ideas by adding to it the principle of interference. Fresnel

---

<sup>1</sup>Apparently, Huygens was in doubt whether or not light originated from the entire interior of the flame. This follows from the presence of a "disclaimer" in the original manuscript "comme je crois" ["as I believe"] which was added later but did not appear in the printed book.

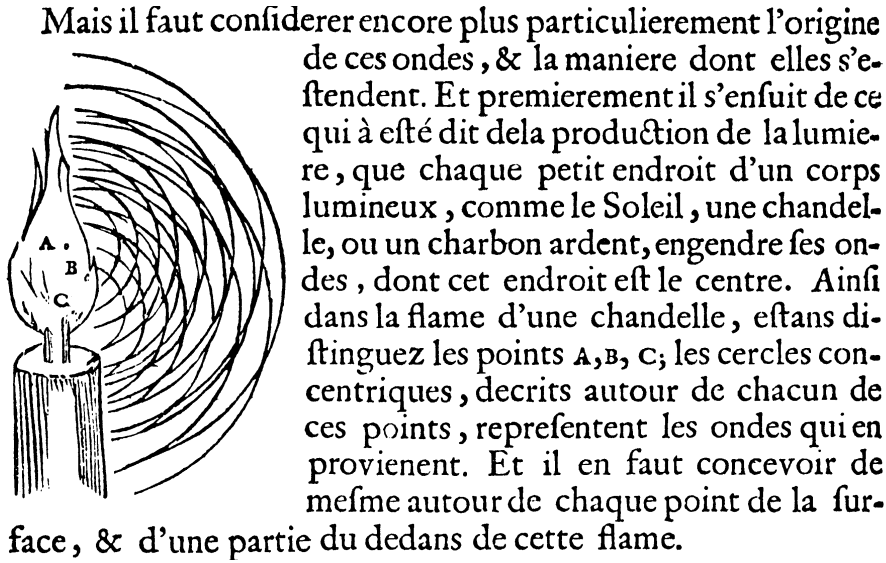


Figure 1.1: Fragment of *Traité de la lumière*, in which Huygens formulated what has since become known as Huygens' Principle.

derived the formula

$$dU(P) = K(\chi)A \frac{e^{ikr_0}}{r_0} \frac{e^{iks}}{s} dS \quad (1.1)$$

(see Fig. 1.2) where the total amplitude or disturbance  $U$  at the point of observation  $P$  is found by adding (in accordance with Huygens' Principle) all contributions of surface elements  $dS$  which together make up the wavefront  $S$ . He postulated a direction-dependent factor, the obliquity factor  $K(\chi)$ , to account for the "efficiency" of propagation, which is maximum in the forward direction  $\chi = 0$  and zero for  $\chi = \pi/2$ .

The theory of diffraction was further developed by Kirchhoff in 1880. By applying Green's theorem to solutions of the Helmholtz equation he showed that the disturbance  $U$  at a point  $\mathbf{x}$  can be written as an integral over a *closed* surface  $S$ , which contains  $\mathbf{x}$  in its interior:

$$U_{\text{HK}}(\mathbf{x}) = \frac{1}{4\pi} \iint_S \left[ U(\mathbf{p}) \frac{\partial}{\partial n} (G_{\text{HK}}(\mathbf{p}, \mathbf{x})) - G_{\text{HK}}(\mathbf{p}, \mathbf{x}) \frac{\partial U}{\partial n}(\mathbf{p}) \right] dS. \quad (1.2)$$

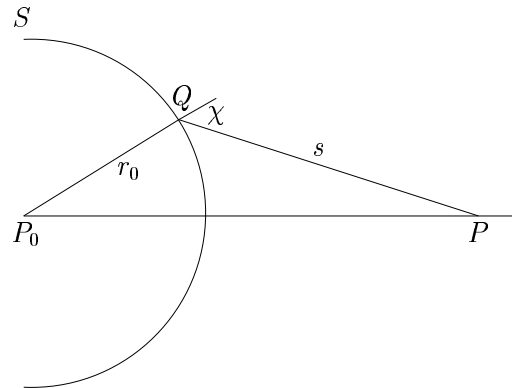


Figure 1.2: Illustration of Fresnel's formula. A source located at  $P_0$  produces a wave front  $S$ . The contribution  $dU(P)$  due to the element  $dS$  at  $Q$  to the field at the observation point  $P$  is given by Eq. (1.1).  $k = 2\pi/\lambda$  is the wavenumber.

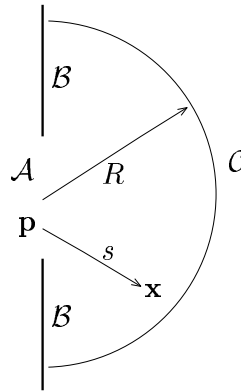


Figure 1.3: Kirchhoff's construction.

Here  $\partial/\partial n$  denotes differentiation in the direction of the inward normal  $\mathbf{n}$  to the surface  $S$  and  $s$  is the distance between  $\mathbf{x}$  and the point of integration  $\mathbf{p}$ . Furthermore,  $G_{\text{HK}}(\mathbf{p}, \mathbf{x}) = e^{iks}/s$  is the free-space Green's function. This result is known as the Helmholtz–Kirchhoff integral theorem (HK). Kirchhoff applied this result to the diffraction at an aperture in a plane screen (Fig. 1.3). The surface of integration  $S$  is made up of three parts: the aperture  $\mathcal{A}$ , the unilluminated side of the screen  $\mathcal{B}$ , and the semi-sphere  $\mathcal{C}$  with radius  $R$ . In order to simplify Eq. (1.2) Kirchhoff adopted the following Ansatz for the field and its derivative:

1. Across the aperture surface  $\mathcal{A}$ , the field and its normal derivative are the same as they would be in the absence of the screen,

$$U(\mathbf{p}) = U_{\text{inc}}(\mathbf{p}), \quad \frac{\partial U(\mathbf{p})}{\partial n} = \frac{\partial U(\mathbf{p})}{\partial n} \Big|_{\text{inc}}, \quad \text{if } p \in \mathcal{A}, \quad (1.3)$$

where the suffix inc refers to the incident field.

2. Across the portion  $\mathcal{B}$ , which lies in the geometrical shadow of the screen, the field and its normal derivative are identically zero,

$$U(\mathbf{p}) = 0, \quad \frac{\partial U(\mathbf{p})}{\partial n} = 0, \quad \text{if } p \in \mathcal{B}. \quad (1.4)$$

Furthermore, by taking the radius  $R$  of the semi-sphere  $\mathcal{C}$  to infinity, it can be shown that for outgoing waves the contribution of  $\mathcal{C}$  to the integral (1.2) goes to zero. This condition is known as the Sommerfeld radiation condition and is satisfied for outgoing spherical waves. Now the integral over the closed surface  $S$  is reduced to an integral over the aperture  $\mathcal{A}$  only:

$$U_{\text{K}}(\mathbf{x}) = \frac{1}{4\pi} \iint_{\mathcal{A}} \left[ U_{\text{inc}}(\mathbf{p}) \frac{\partial}{\partial n} \left( \frac{e^{iks}}{s} \right) - \frac{e^{iks}}{s} \frac{\partial U(\mathbf{p})}{\partial n} \Big|_{\text{inc}} \right] dS. \quad (1.5)$$

This diffraction integral has some serious shortcomings. First, one could question the physical reality of the boundary conditions. The presence of the screen will always introduce a scattered field in the immediate neighbourhood of the rim of the aperture. Second, when the point of observation  $\mathbf{p}$  is brought to the interface, the field at  $\mathbf{p}$  does not reproduce the prescribed boundary value. This was explained by Poincaré [BAKER AND COPSON, 1950], who pointed out that prescribing *both* the field and its normal derivative simultaneously overspecifies the solution  $U$ . Despite these inconsistencies the Kirchhoff diffraction integral produces remarkably accurate results. We shortly return to this point.

To circumvent the inconsistencies inherent to Kirchhoff's representation, Rayleigh and Sommerfeld (RS) considered the Helmholtz–Kirchhoff integral (1.2) and noted that if it were possible to choose a Green's function such that *either*  $G$  or  $\partial G/\partial n$  would vanish across the aperture  $\mathcal{A}$ , it would do away with the need to prescribe *both*  $U$  and  $\partial U/\partial n$  simultaneously on

$\mathcal{A}$ . For the case of an aperture in a plane screen they indeed found a pair of Green's functions doing exactly this:

$$G_1(\mathbf{p} - \mathbf{x}) = \frac{e^{iks}}{s} - \frac{e^{ik\tilde{s}}}{\tilde{s}}, \quad (1.6)$$

$$G_2(\mathbf{p} - \mathbf{x}) = \frac{e^{iks}}{s} + \frac{e^{ik\tilde{s}}}{\tilde{s}}, \quad (1.7)$$

where  $s$  is (as before) the distance between  $\mathbf{x}$  and  $\mathbf{p}$  and  $\tilde{s}$  is the distance between  $\mathbf{x}$  and the mirror image of  $\mathbf{p}$  in the aperture plane. If we substitute from (1.6) into (1.2) only the field  $U$  has to be prescribed on  $\mathcal{A}$ . On substituting from (1.7) into (1.2) only the normal derivative  $\partial U/\partial n$  has to be prescribed on  $\mathcal{A}$ . The resulting expressions for the field now read

$$U_{\text{RS1}}(\mathbf{x}) = \frac{1}{4\pi} \iint_{\mathcal{A}} U(\mathbf{p}) \frac{\partial G_1}{\partial n} dS, \quad (1.8)$$

$$U_{\text{RS2}}(\mathbf{x}) = -\frac{1}{4\pi} \iint_{\mathcal{A}} G_2 \frac{\partial U}{\partial n}(\mathbf{p}) dS. \quad (1.9)$$

Despite their manifest consistency, Eqs. (1.8) and (1.9) still suffer from the problem that in practice one does not know exactly the field distribution across the aperture. Just as in the Kirchhoff approach [Eq. (1.5)], one usually resorts to the approximation  $U(\mathbf{p}) = U_{\text{inc}}(\mathbf{p})$  in Eq. (1.8), and  $\partial U/\partial n(\mathbf{p}) = \partial U/\partial n|_{\text{inc}}$  in Eq. (1.9).

A different approach to cure Kirchhoff's integral (1.5) was taken by Kottler [KOTTLER, 1965]. He showed that (1.5), when applied to diffraction at a black screen, is a rigorous solution, not to a boundary value problem, but to a 'saltus problem', i.e. a problem where the boundary values of the field are discontinuous across the screen. In essence, one might say that Kottler used a different definition of 'blackness'.

Maggi and Rubinowicz [BAKER AND COPSON, 1950] introduced the concept of a 'boundary diffraction wave' for diffraction at a black screen. This dates back to a physically appealing idea of Thomas Young, who considered diffraction at an aperture to be the result of interference between the uninterrupted incident wave and the wave scattered by the rim of the aperture. Maggi and Rubinowicz showed that the Kirchhoff diffraction integral (1.5) can indeed be written as the sum of a geometrical optics term (the

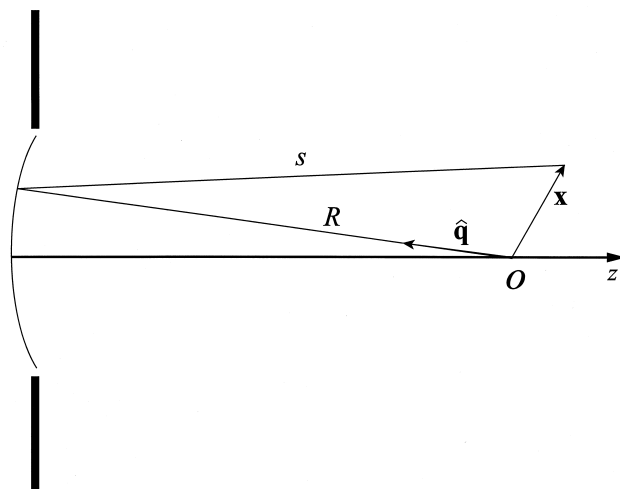


Figure 1.4: Illustration of the Debye approximation.

propagated incident field) and a boundary term (the field scattered by the rim of the aperture). It was later found [MARCHAND AND WOLF, 1962] that for the Rayleigh–Sommerfeld diffraction integrals (1.8), (1.9) too a boundary diffraction wave term can be derived.

So now three different descriptions for the field diffracted by an aperture in a plane screen have emerged, Eqs. (1.5), (1.8) and (1.9). Detailed investigations as to which of the three best predicts the outcome of an actual experiment have been carried out by several authors [SILVER, 1962; MARCHAND AND WOLF, 1966; STAMNES, 1986]. From these studies one can conclude that in the proximity of the aperture the Kirchhoff theory [Eq. (1.5)] agrees quite well, RS2 [Eq. (1.9)] agrees reasonably well, but RS1 [Eq. (1.8)] is in poor agreement with the experiments. In the far field all three converge to the same result. See also [J.W. GOODMAN, 1996].

In a classical paper Debye [1909] studied the diffraction pattern of *converging* waves emanating from an aperture. He introduced an approximation to the Green's function in the Kirchhoff integral (1.5) which is of great practical use (see Fig. 1.4). Approximating  $s \approx R - \hat{\mathbf{q}} \cdot \mathbf{x}$ , the Green's function  $G = e^{iks}/s$  can be written as

$$G(\mathbf{p}, \mathbf{x}) \approx \frac{1}{R} \exp[-ik(R - \hat{\mathbf{q}} \cdot \mathbf{x})] = \frac{e^{-ikR}}{R} e^{ik\hat{\mathbf{q}} \cdot \mathbf{x}}. \quad (1.10)$$

This approximation is justified for points close to the focus and far from the aperture. He found that for such points  $\mathbf{x}$

$$U(\mathbf{x}) = \frac{ik}{2\pi} \int_{\Omega} e^{ik\hat{\mathbf{q}}\cdot\mathbf{x}} d\Omega, \quad (1.11)$$

where  $d\Omega$  is the element of the solid angle  $\Omega$  that  $dS$  subtends at the focus. It is seen that the diffracted field is thus a superposition of plane waves (with direction  $\hat{\mathbf{q}}$ ), rather than the spherical Huygens wavelets of, for example, Eq. (1.5). Being composed of elementary plane waves, Eq. (1.11) is a rigorous solution of the wave equation. As the integration is limited to the solid angle  $\Omega$ , only waves with propagation directions lying in the geometrical light cone contribute. In other words, the angular spectrum representation of the diffracted field has a finite support  $\Omega$ , and is discontinuous for the polar angle equal to the semi-aperture angle.

### Focusing at low Fresnel numbers

According to Eq. (1.11), the intensity near the focus is symmetric about the geometrical focal plane. It was found by Farnell in 1958 while studying microwaves that in practice this is not always true [FARNELL, 1958]. It turned out that the point of maximum intensity can lie in between the focusing lens and the geometrical focus. This phenomenon is nowadays referred to as the focal shift.

It was not until 1981 that it was pointed out by Stamnes that the above symmetry is connected with the Debye approximation, and is not a consequence of the Kirchhoff and Rayleigh–Sommerfeld expressions (1.8) and (1.9) [STAMNES AND SPJELKAVIK, 1981]. In the same year Wolf and Li showed that the Debye approximation is only valid if

$$N := \frac{a^2}{\lambda f} \gg 1, \quad (1.12)$$

where  $N$  is the Fresnel number,  $a$  the radius of the aperture,  $\lambda$  the wavelength, and  $f$  the focal length [WOLF AND LI, 1981]. When, e.g., a laser beam is very weakly focused, this condition is not always satisfied and the focal shift occurs. A theoretical analysis of the intensity distribution in the focal region for  $N \approx 1$  was developed by the same authors [LI AND

WOLF, 1981; LI AND WOLF, 1982; LI AND WOLF, 1984; LI, 1987]. In a study using lasers rather than masers, Li and Platzner showed this theory to be in good agreement with experimental results [LI AND PLATZER, 1983].

## 1.2 Vectorial focusing theory

The first rigorous presentation of a vectorial focusing theory was given by Wolf and co-workers [WOLF, 1959; RICHARDS AND WOLF, 1959; BOIVIN AND WOLF, 1965; BOIVIN ET AL., 1967]. Using the Debye approximation they carried out an extensive study of the field near the focus of a converging electromagnetic wave, resulting in an integral representation in the form of an angular spectrum of plane waves. Their results can be regarded as the electromagnetic analogue of the scalar expression (1.11). Special emphasis was placed on the electric energy density and the Poynting vector. Richards and Wolf found a diffraction pattern that is symmetric around the focal plane, which, as mentioned earlier, is a result of the use of the Debye approximation. As a consequence, the theory of Richards and Wolf is valid for high Fresnel number systems. Also, these authors were the first to identify the Airy rings in the focal plane as phase singularities [BOIVIN ET AL., 1967]. Experimental observations of these phase singularities were recently made [KARMAN ET AL., 1997].

Visser and Wiersma [VISSER AND WIERSMA, 1991; VISSER AND WIERSMA, 1992] used the Stratton–Chu diffraction integral [STRATTON AND CHU, 1939] to study the electromagnetic field in the focal region of a high aperture lens with spherical aberration and defocus. The aberrations induced by a non-perfect lens were taken into account by integrating over the aberrated wavefront in the exit pupil. It was found that the axial intensity distribution is no longer symmetric around the focal plane. In [VISSER AND WIERSMA, 1991] an expression for the diffracted field was derived of which the vectorial Richards and Wolf theory (for high Fresnel number systems) and the scalar paraxial theory of Li and Wolf [LI AND WOLF, 1981; LI AND WOLF, 1982] (for low Fresnel number systems) are special cases.

A more exhaustive overview of scalar focusing theory can be found in [BORN AND WOLF, 1999]. For a review of electromagnetic diffraction theory the reader is referred to [BOUWKAMP, 1954].

### 1.3 The structure of this thesis

This thesis is based on the following publications:

1. *Defocusing of a converging electromagnetic wave by a plane dielectric interface*, by S.H. Wiersma and T.D. Visser, *J. Opt. Soc. Am. A* **13**, pp. 320–325 (1996).
2. *Comparison of different theories for focusing through a plane interface*, by S.H. Wiersma, P. Török, T.D. Visser and P. Varga, *J. Opt. Soc. Am. A* **14**, pp. 1482–1490 (1997).
3. *Focusing through an interface: Scanning and localizing the intensity*, by S.H. Wiersma, T.D. Visser and P. Török, *Opt. Lett.* **23**, pp. 415–417 (1998).
4. *Annular focusing through a dielectric interface: Scanning and confining the intensity*, by S.H. Wiersma, T.D. Visser and P. Török, *Pure Appl. Opt.* **7**, pp. 1237–1248 (1998).
5. *Reflection-induced spectral changes of the pulsed radiation emitted by a point source, Part I: Theory*, by S.H. Wiersma, T.D. Visser and A.T. de Hoop, submitted for publication.
6. *Reflection-induced spectral changes of the pulsed radiation emitted by a point source, Part II: Application*, by S.H. Wiersma, T.D. Visser and A.T. de Hoop, submitted for publication.

#### **Chapter 2: Defocusing of a Converging Electromagnetic Wave by a Plane Dielectric Interface**

The usual treatment of the focusing of light assumes that the process takes place in a homogeneous portion of space. In practice, however, one focuses the light into a medium with a different refractive index. In, for example, optical microscopy a lens produces a converging spherical wave in air (with a refractive index equal to 1). This wave is then incident on a biological specimen with a refractive index typically of 1.35. The same situation applies in optical recording, optical trapping, lithography, and in clinical applications such as the hyperthermia treatment of cancer. It is the aim of this

Chapter to analyze the intensity distribution within the medium into which the light is focused. Therefore a study is carried out of the effect of a plane dielectric interface on a converging spherical electromagnetic wave. The process is examined in three stages.

First, it is described how a lens changes an incident linearly polarized plane wave into an outgoing converging spherical wave. The field on the spherical wavefront in the exit pupil of the lens is derived using the classical analysis of Richards and Wolf [1959]. Second, it is calculated how this field propagates in medium 1 onto the interface. With the field on one side of the interface known, we can apply a suitable plane wave expansion and obtain the field on the other side of the interface by using the Fresnel transmission coefficients. In the transmission process phase differences are introduced between waves emerging from different polar angles  $\theta$ . The amplitude also changes as a function of  $\theta$ . Third, the field distribution just behind the interface in the second medium thus obtained, propagates through medium 2 to produce a diffraction pattern. The diffraction pattern is calculated by employing the so-called m-theory of diffraction [SMYTHE, 1947; TORALDO DI FRANCIA, 1955]. The m-theory, based on the observation that the field in a homogeneous half-space is completely determined by the tangential component of either the magnetic or the electric field across its bounding plane [STRATTON, 1941], satisfies Maxwell's equations and reproduces the imposed boundary conditions. Because of the explicit use of mirror symmetry in the derivation of the relevant Green's function, it can be regarded as the electromagnetic equivalent of the Rayleigh–Sommerfeld diffraction integrals (Eqs. (1.8) and (1.9)).

Numerical calculations of the diffraction integral are carried out for observation points both along the optical axis and in planes perpendicular to it. It is found that the presence of an interface has a strong broadening effect on the intensity distribution, making it highly asymmetric. The peak value of the intensity profile is sharply reduced, compared to the case where there is no interface present. Examples are presented for various refractive index contrasts and depths of focus. We note that our analysis is also valid for lenses with a large angular aperture.

An issue of great practical interest is how the position of the diffraction pattern changes when the converging lens is moved with respect to the interface. Often (and erroneously!) these two displacements are taken to be

the same. From elementary geometrical reasoning an expression is derived relating the shift of the lens to the actual shift of the intensity profile. It is shown that the ratio of these two shifts equals  $n_1/n_2$ , where  $n_i$  denotes the index of refraction of medium  $i$ . In other words, an axial displacement of the lens causes an axial displacement of the diffraction pattern that is  $n_1/n_2$  times larger. This explains the anomalous volumes reported from confocal microscopy experiments, as noted in [VISSER AND OUD, 1994].

### Chapter 3: Comparison of Different Theories for Focusing through a Plane Interface

At the time that Chapter 2 was written, an independent investigation into the same problem was carried out [TÖRÖK ET AL., 1995A]. This naturally raised the question of how these two approaches compare. It is the aim of this Chapter to compare the two studies, and to further analyze the structure of the electromagnetic field in the second medium.

We note that slightly later even a third group started publishing on interface focusing [DHAYALAN AND STAMNES, 1998; STAMNES AND JIANG, 1998].

In this Chapter a comparison is presented between two diffraction theories: the one outlined in Chapter 2 and the theory put forward by Török *et al.* [1995a]. In the latter, the electric field is calculated by a series of coordinate transformations which handle the  $s$ - and  $p$ -polarized components separately. Although both theories use different approaches they predict axial distributions with very little difference.

The focusing through an interface is also studied from a geometrical optics point of view. It is shown that the intensity distribution is restricted to a part of the optical axis only, limited by so-called shadow boundaries, the positions of which are given in terms of the refractive indices and the position of the interface relative to the lens. The boundary corresponding to the intersection of rays making small angles with the optical axis is seen to give a fairly good approximation for the position of the intensity peak. Also the shape of the intensity distribution agrees well with the vectorial diffraction optics results.

Finally, the implications for three-dimensional imaging of the presence of the dielectric interface are discussed. There are two main causes for

errors in the measurements of volumes: (a) the difference in the axial displacement of the lens with respect to the interface, and the axial displacement of the intensity distribution; and (b) the width of the intensity distribution which may be comparable to that of the object which is imaged. A simple formula is presented to extract the ‘true’ size of an object from its measured ‘apparent’ size.

#### **Chapter 4. Annular Focusing through a Dielectric Interface: Scanning and Confining the Intensity**

As was discussed in the two previous Chapters, the focusing of light through an interface leads to an aberrated intensity distribution that is considerably spread out and which has a relatively low peak intensity. For many applications this situation is undesirable.

We present a method, using a well-chosen annular (ring-shaped) aperture, which can greatly improve the localization of the intensity around a prescribed point on the axis. Also, the intensity at that point can be increased significantly.

The analysis employs the method of stationary phase to study the relevant diffraction integrals. In addition, the connection between the optimization of the annular aperture (with respect to the local intensity) and geometrical optics is analyzed.

A new scanning mechanism is proposed to continuously move the intensity peak axially through the second medium. This is achieved by smoothly varying the two radii of the annular aperture. This mechanism may be applied in, e.g., lithography, 3-D imaging and optical trapping.

#### **Chapters 5 and 6: Reflection-induced Spectral Changes of the Pulsed Radiation Emitted by a Point Source**

In the last few years there has been a great interest in mechanisms which alter the power spectrum of electromagnetic or acoustic radiation. In addition to long known causes such as the Doppler effect and the influence of absorption and dispersion, it was predicted by Wolf in 1987 that the spectrum emitted by a source can even change on propagation through free space. This change is caused by the coherence of the source [WOLF, 1987].

These correlation-induced spectral changes have since been confirmed experimentally [BOCKO ET AL., 1987]. A closely related phenomenon is the scattering of a wavefield by a random medium. The coherence properties of the medium cause the power spectrum of the scattered field to differ from the one of the incident field [MANDEL AND WOLF, 1995; WOLF AND JAMES, 1996].

In contrast to the other chapters of this thesis, Chapters 5 and 6 contain an analysis in the time domain. It deals with spectral changes in the power density spectrum emitted by a pulsed point source. The source is located above a half-space with a wavespeed that differs from the wavespeed of the half-space in which the source is embedded. The new cause of spectral changes which is chartered here is reflection at an interface. It is studied how reflection at the planar interface between the two media with different wavespeeds changes the spectrum of a propagating scalar wave field emitted by a pulsed point source. The effect is studied both as a function of the two wavespeeds, and as a function of the point of observation.

To analyze the pulse propagation in our layered configuration the modified Cagniard method [DE HOOP, 1960] is used. This method has – apart from its mathematical beauty – the advantage that analytic expressions for the Green's function of the reflected field are obtained. It allows us to clearly distinguish the contributions of the body-waves and the head-waves to the reflected field [MINTROP, 1930]. The total field in the time domain is then subjected to a Fourier transform with respect to time to obtain the power spectrum.

In the numerical examples the parameters are taken from acoustics. In addition, the pulse time widths are chosen such that within the spectral regime dispersion may be neglected. It is found that the changes in the observed power spectrum can be significant. These results clearly establish reflection at an interface as an independent cause of spectral changes.

## Chapter 2

# Defocusing of a converging electromagnetic wave by a plane dielectric interface

*based on* S.H. Wiersma and T.D. Visser,  
J. Opt. Soc. Am. 13, pp. 320–325 (1996)

We study how a converging spherical wave gets distorted by a plane dielectric interface. The fields in the second medium are obtained by evaluating the “m-theory” diffraction integral on the interface. The loss of intensity and the form of the intensity distribution are investigated. Examples are presented for various refractive index contrasts and depths of focus. In general the intensity gets spread out over a volume that is large compared to the case without refractive index contrast. It was found that moving the focusing lens a distance  $d$  towards the interface does not result in an equal shift of the intensity profile. This latter point has important practical implications.

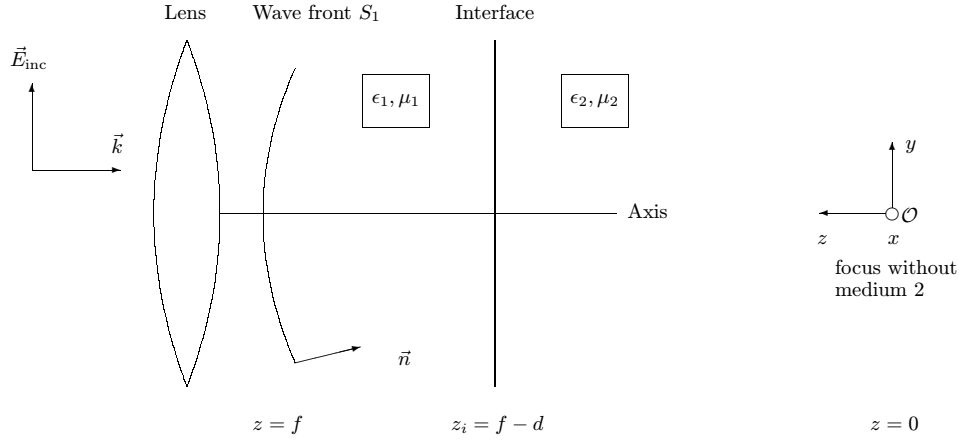


Figure 2.1: Definition of the coordinate system. Shown on the left are the unit wave vector  $\hat{k}$  and the electric vector  $\vec{E}_{\text{inc}}$ , both before refraction by an objective with semi aperture angle  $\Omega$ . The incoming wave propagates perpendicular to the interface in the  $-z$ -direction. The origin is placed at a distance  $f$  from the exit pupil.  $\hat{n}$  is the unit wave vector after refraction by the lens. The polar angle  $\theta$  is the angle between  $\hat{n}$  and the positive  $z$ -axis.

## 2.1 Introduction

The focusing of a plane electromagnetic wave by a lens has been the subject of several studies [SMYTHE, 1947; BAKER AND COPSON, 1950; SEVERIN, 1951; BOUWKAMP, 1954; TORALDO DI FRANCA, 1955; RICHARDS AND WOLF, 1959; WOLF, 1959; LUNEBURG, 1964; KOTTLER, 1965; BOIVIN AND WOLF, 1965; KARCZEWSKI AND WOLF, 1966A; KARCZEWSKI AND WOLF, 1966B; KOTTLER, 1967; VISSER AND WIER-SMA, 1992]. In this paper we study the more complex situation of focused waves incident on a plane interface. That is, a lens in medium 1 produces a converging spherical wave that after crossing an interface with medium 2 gets distorted (see Fig. 2.1). Both media are assumed to be linear, homogeneous, isotropic, and non-conducting. It is the aim of this study to describe the influence of the interface on the intensity and on the form of the diffraction pattern. The intensity is found to be no longer localized in a small region, as is the case when there is just one medium, but is rather spread out over a larger volume. Our results have implications, e.g., for microscopy with immersion-fluid objectives where the interface separates

the immersion-oil/cover glass region from the (usually watery) object. As will be discussed, the difference in refractive indices results in a severe loss of resolution. A very relevant issue is how the diffraction pattern changes when the focusing lens is moved with respect to the interface. We shall demonstrate that, in general, the intensity profile is shifted over a distance that differs a constant factor from that over which the lens is moved.

A closely related problem has been studied by Ling and Lee [LING AND LEE, 1984; STAMNES, 1986]. Whereas we consider a converging spherical wave in medium 1 that gets distorted in medium 2, they calculated which (non-spherical) form the wave front in the first medium must have to produce a perfectly spherical wave in the second medium. Their study has applications in the field of hyperthermia treatment where a maximum intensity (and hence a spherical wave) is desired in medium 2. Unlike us, Ling and Lee limited themselves to lossless media (i.e. with electric permittivities  $\varepsilon_1$  and  $\varepsilon_2$  both real).

Another study of interest [NEMOTO, 1988] uses a scalar theory in the paraxial approximation to calculate the waist shift of a Gaussian beam caused by a dielectric interface.

Also worth mentioning is a paper by Gasper *et al.* [1976] in which asymptotic approximations for the transmitted and reflected fields are given.

Our approach is as follows. An incoming plane wave, propagating perpendicular to the interface, is converted by a perfect lens obeying the sine condition [BORN AND WOLF, 1997], into a converging spherical wave (see Fig. 2.1). In the exit pupil the electromagnetic field on the emerging wave front  $S_1$  is determined. As will be justified, the effects of refraction on the polarization are neglected. Neither the form of the wave front, nor the directions of the (time-independent parts of the) electromagnetic vectors are assumed to change while travelling to the interface (ray approximation). This too will be justified. Since the wave converges towards the interface, its amplitude will have increased by an amount determined by the distance travelled, which depends on the polar angle  $\theta$ . Additionally, a phase factor which is also  $\theta$ -dependent is introduced. Having determined the incident fields on the interface, the transmitted field is derived with the help of Fresnel coefficients. The so-called m-theory of diffraction can then be used to calculate the energy density in the region of focus in the second medium. No paraxial approximation is necessary for the developed formalism. The

m-theory is due to several authors, namely Smythe [1947], Severin [1951] and Toraldo di Francia [1955]. The latter treatment is probably the clearest.

Throughout this paper we use SI units.

## 2.2 The field on the interface

Consider an incident monochromatic plane wave propagating in the negative  $z$ -direction that is linearly polarized,

$$\mathbf{E} = \mathbf{E}_{\text{inc}} \exp[i(k_1 \hat{\mathbf{k}} \cdot \mathbf{r} + \omega t)] \quad (z > f) \quad (2.1)$$

with  $k_1$  the wavenumber in medium 1 and the electric field amplitude vector

$$\mathbf{E}_{\text{inc}} = (\cos \alpha, \sin \alpha, 0), \quad (2.2)$$

where  $\alpha$  is the angle of polarization. From here on, we will take  $\alpha = 0$  and suppress the harmonic time dependence.

It is assumed that the lens obeys the sine condition [BORN AND WOLF, 1997], i.e. rays travelling parallel to the  $z$ -axis emerge at the same lateral distance from the axis as they entered it.

The meridional plane is spanned by the incident unit wave vector  $\hat{\mathbf{k}}$  and the unit wave vector after refraction  $\hat{\mathbf{n}}$ , with

$$\hat{\mathbf{k}} = \begin{pmatrix} 0 \\ 0 \\ -1 \end{pmatrix}, \quad \hat{\mathbf{n}} = - \begin{pmatrix} \sin \theta \cos \phi \\ \sin \theta \sin \phi \\ \cos \theta \end{pmatrix}. \quad (2.3)$$

The effect of refraction on the polarization angle will be neglected. From the Fresnel equations it follows that this is justified as long as the incoming wave vector does not make an appreciable angle with the normal of the refracting surfaces that make up the lens system. For practical objectives, this seems to be a reasonable assumption. Now the field  $\mathbf{E}_{S_1}$  in the exit pupil can be written as the sum of an unchanged component ( $\mathbf{E}_s$ ) of  $\mathbf{E}_{\text{inc}}$  which is perpendicular to the meridional plane and a rotated component ( $\mathbf{E}_p$ ) which lies in the meridional plane [RICHARDS AND WOLF, 1959; VISSER AND WIERSMA, 1992]. The first component lies in the direction of  $\hat{\mathbf{k}} \times \hat{\mathbf{n}}$ . The

second is normal to both  $\hat{k}$  and  $\hat{k} \times \hat{n}$ , and points after refraction in the direction of  $\hat{n} \times (\hat{k} \times \hat{n})$ . Hence,

$$\mathbf{E}_s = \frac{\mathbf{E}_{\text{inc}} \cdot (\hat{k} \times \hat{n})}{|\hat{k} \times \hat{n}|^2} (\hat{k} \times \hat{n}), \quad (2.4)$$

$$\mathbf{E}_p = \frac{\mathbf{E}_{\text{inc}} \cdot (\hat{k} \times (\hat{k} \times \hat{n}))}{|\hat{k} \times (\hat{k} \times \hat{n})| |\hat{n} \times (\hat{k} \times \hat{n})|} (\hat{n} \times (\hat{k} \times \hat{n})). \quad (2.5)$$

The now normalized directions of decomposition are given by

$$\frac{\hat{k} \times \hat{n}}{|\hat{k} \times \hat{n}|} = \begin{pmatrix} -\sin \phi \\ \cos \phi \\ 0 \end{pmatrix}, \quad (2.6)$$

$$\frac{\hat{n} \times (\hat{k} \times \hat{n})}{|\hat{n} \times (\hat{k} \times \hat{n})|} = \begin{pmatrix} \cos \theta \cos \phi \\ \cos \theta \sin \phi \\ -\sin \theta \end{pmatrix}, \quad (2.7)$$

$$\frac{\hat{k} \times (\hat{k} \times \hat{n})}{|\hat{k} \times (\hat{k} \times \hat{n})|} = \begin{pmatrix} \cos \phi \\ \sin \phi \\ 0 \end{pmatrix}. \quad (2.8)$$

Indulging in a little algebra, we find for the components  $\mathbf{E}_s$  and  $\mathbf{E}_p$

$$\mathbf{E}_s = \cos^{1/2} \theta \sin \phi \begin{pmatrix} \sin \phi \\ -\cos \phi \\ 0 \end{pmatrix} \quad (2.9)$$

and

$$\mathbf{E}_p = \cos^{1/2} \theta \cos \phi \begin{pmatrix} \cos \theta \cos \phi \\ \cos \theta \sin \phi \\ -\sin \theta \end{pmatrix}. \quad (2.10)$$

Both components have been multiplied by a factor  $\cos^{1/2} \theta$  to account for the aplanatic energy projection by the lens [STAMNES, 1986]. (Note that  $\mathbf{E}_s$  has no  $z$ -component, as is expected.) So the field in the exit pupil  $S_1$  is given by

$$\mathbf{E} = \mathbf{E}_{S_1} \exp[ik_1 \hat{n} \cdot \mathbf{r}] \quad (\text{in exit pupil}), \quad (2.11)$$

where

$$\mathbf{E}_{S_1} = \mathbf{E}_s + \mathbf{E}_p. \quad (2.12)$$

The reader may be assured that indeed  $\nabla \cdot \mathbf{E} = 0$ , since  $\hat{n} \cdot \mathbf{E}_{S_1} = 0$ .

Next consider how the field through the spherical segment on  $S_1$  between the angles  $\theta$  and  $\theta + d\theta$  is changed upon reaching the corresponding ring at the interface. Two factors have to be considered, namely a phase factor and an amplitude factor, both angle-dependent, which we are now about to determine.

The path length for a ray travelling at an angle  $\theta$  from  $S_1$  to the interface equals  $f - t(\theta)$ , with

$$t(\theta) = (f - d)/\cos \theta, \quad (2.13)$$

where  $f$  is the focal length of the lens and  $d$  the distance from the exit pupil to the interface (see Fig. 2.1). So the phase factor  $F(\theta)$  that is introduced is

$$F(\theta) = \exp \left[ ik_1 \left( f - \frac{f - d}{\cos \theta} \right) \right]. \quad (2.14)$$

$k_i$  is the wave number in medium  $i$ , for which

$$k_i \equiv (\omega^2 \varepsilon_i \mu_i)^{1/2} \quad (i = 1, 2), \quad (2.15)$$

where  $\omega$  denotes the angular frequency, and the square root is taken such that  $\text{Im}(k_i) \leq 0$ .

The area of the spherical segment on  $S_1$  is proportional to  $f^2$ , whereas the area of the corresponding ring on the interface is proportional to  $t^2(\theta)/\cos \theta$ . Conservation of energy requires that the amplitude of the electric field is inversely proportional to the square root of the ratio of the respective areas. Hence the amplitude factor  $K(\theta)$  that is introduced reads

$$K(\theta) = \frac{f \cos^{3/2} \theta}{f - d}. \quad (2.16)$$

So we get for the electric field  $\mathbf{E}$  incident on the left-hand side of the interface at  $z_i = f - d$

$$\mathbf{E}_{\delta \downarrow 0}(\theta, \phi, z_i + \delta) = K(\theta) F(\theta) \mathbf{E}_{S_1}(\theta, \phi). \quad (2.17)$$

It should be noted that the use of a vectorial diffraction theory instead of a geometrical approach to calculate the field on the interface would have yielded the very same result. Such a theory, as is due to Richards and Wolf (Eq. (3.3) of [WOLF, 1959] and Eq. (2.17) of [RICHARDS AND WOLF, 1959]), describes the focused field as a superposition of plane waves. These waves travel in the direction of the focus one would have in the absence of medium 2 (i.e. the origin  $\mathcal{O}$  in Fig. 2.1), and have an amplitude  $E_s(\theta)$  given by Eq. (2.12). Consequently, application of this theory also leads to Eq. (2.17).

At the right-hand side of the interface, in medium 2, the amplitudes of the electric field components are multiplied by  $\eta_s$  and  $\eta_p$ , the Fresnel coefficients for transmission of the  $s$  and  $p$  components, respectively. These coefficients depend on the angle of incidence  $\theta$  and the refractive indices on either side of the interface. The index of refraction  $n_i$  is given by  $n_i = c\sqrt{\varepsilon_i\mu_i}$  ( $i = 1, 2$ ), with  $c$  the speed of light in vacuo. Whereas the  $s$ -component of the field remains otherwise unaffected, the component parallel to the plane of incidence ( $\mathbf{E}_p$ ) is also rotated. To find its new form consider the (normalized) direction of propagation  $\hat{q}$  of the refracted wave. It is obviously given by

$$\hat{q} = - \begin{pmatrix} \sin \theta' \cos \phi \\ \sin \theta' \sin \phi \\ \cos \theta' \end{pmatrix}, \quad (2.18)$$

with  $\theta'$  given by Snell's Law as  $\theta' = \sin^{-1}[(n_1 \sin \theta)/n_2]$ . After refraction  $\mathbf{E}_p$  is perpendicular to both  $\hat{q}$  and  $\hat{q} \times \hat{n}$ , i.e. it is then directed along  $\hat{q} \times (\hat{q} \times \hat{n})$ . Hence

$$\mathbf{E}_{p;\delta\downarrow 0}(z_i - \delta) = \eta_p \left| \mathbf{E}_{p;\delta\downarrow 0}(z_i + \delta) \right| \frac{\hat{q} \times (\hat{q} \times \hat{n})}{|\hat{q} \times (\hat{q} \times \hat{n})|}. \quad (2.19)$$

Also,

$$\mathbf{E}_{s;\delta\downarrow 0}(z_i - \delta) = \eta_s \mathbf{E}_{s;\delta\downarrow 0}(z_i + \delta), \quad (2.20)$$

where the  $(\theta, \phi)$  dependence is temporarily suppressed. So we find for the

total electric field on the right-hand side of the interface

$$\begin{aligned}
\mathbf{E}_{\delta\downarrow 0}(z_i - \delta) &= \mathbf{E}_{s;\delta\downarrow 0}(z_i - \delta) + \mathbf{E}_{p;\delta\downarrow 0}(z_i - \delta), \\
&= K(\theta)F(\theta)\cos^{1/2}\theta \left[ \eta_s \sin\phi \begin{pmatrix} \sin\phi \\ -\cos\phi \\ 0 \end{pmatrix} \right. \\
&\quad \left. + \eta_p \cos\phi \begin{pmatrix} \cos\theta' \cos\phi \\ \cos\theta' \sin\phi \\ -\sin\theta' \end{pmatrix} \right], \tag{2.21}
\end{aligned}$$

where we have used (2.9), (2.10) and (2.19). This is the final expression for the electric field after it has just traversed the interface.

As will be explained in the next section, in the formalism that we use, the vectorial quantity  $\hat{\mathbf{m}} \times \mathbf{E}$  fully determines the electric field at any point in medium 2 [STRATTON, 1941]. The normal  $\hat{\mathbf{m}}$  to the interface equals  $(0, 0, 1)$ , see Fig. 2.1. So

$$\begin{aligned}
\hat{\mathbf{m}} \times \mathbf{E}(\theta, \phi, z_i) &= K(\theta)F(\theta)\cos^{1/2}\theta \\
&\times \left[ \eta_s \sin\phi \begin{pmatrix} \cos\phi \\ \sin\phi \\ 0 \end{pmatrix} + \eta_p \cos\phi \begin{pmatrix} -\cos\theta' \sin\phi \\ \cos\theta' \cos\phi \\ 0 \end{pmatrix} \right]. \tag{2.22}
\end{aligned}$$

We have now arrived at our first goal. The relevant field quantity immediately to the right of the interface has been determined. The diffraction integral can now be applied to get an expression for the field near its new focal region in medium 2.

### 2.3 The m-theory

The derivation of the m-theory presented in this section essentially follows Toraldo di Francia [1955], Chap. 10, pp. 213–223. It is well known that a solution  $f(Q)$  of the inhomogeneous wave equation

$$\nabla^2 f + k^2 f = h(Q), \tag{2.23}$$

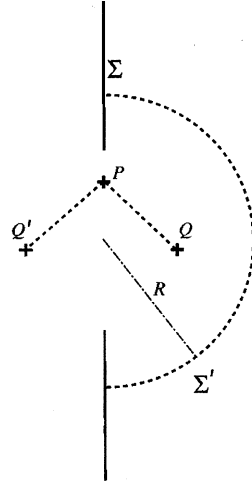


Figure 2.2: The geometry used for the construction of the Green functions  $G^{(\pm)}$ .

with  $k$  as the wavenumber, can be obtained in a form

$$f(Q) = - \int_V G(P, Q) h(P) dP, \quad (2.24)$$

where  $G(P, Q)$  represents the Green function pertaining to Helmholtz' equation and  $V$  is the three-dimensional support of the function  $h$ . Hence

$$\nabla^2 G(P, Q) + k^2 G(P, Q) = -\delta(Q - P). \quad (2.25)$$

Next, following Sommerfeld [1954], we construct the point  $Q'$  that is the mirror image of  $Q$  with respect to the plane  $\Sigma$  (see Fig. 2.2). Two new Green functions can then be defined as

$$G^{(\pm)}(P, Q) = G(P, Q) \pm G(P, Q'). \quad (2.26)$$

It follows from Eq. (2.25) that they satisfy

$$\nabla_p^2 G^{(\pm)}(P, Q) + k^2 G^{(\pm)}(P, Q) = -\delta(Q - P) \mp \delta(Q' - P). \quad (2.27)$$

Consider an arbitrary constant vector  $\mathbf{c}$ , with components  $\mathbf{c}_1$  parallel and  $\mathbf{c}_2$  perpendicular to the plane  $\Sigma$ . Define the vector function  $\Gamma$  as

$$\Gamma(P, Q) = \mathbf{c}_1 G^{(-)}(P, Q) + \mathbf{c}_2 G^{(+)}(P, Q). \quad (2.28)$$

Thus Eq. (2.27) yields

$$\begin{aligned} \nabla_P^2 \Gamma(P, Q) + k^2 \Gamma(P, Q) = & -(\mathbf{c}_1 + \mathbf{c}_2) \delta(Q - P) \\ & + (\mathbf{c}_1 - \mathbf{c}_2) \delta(Q' - P). \end{aligned} \quad (2.29)$$

Next, we derive an identity that will be of later use (cf. [STRATTON AND CHU, 1939]). Let  $\mathbf{A}$  and  $\mathbf{B}$  be two vector functions of position which together with their first and second derivatives are continuous throughout  $V$  and on the surface  $S$  that bounds  $V$ . The divergence theorem is applied to the vector  $\mathbf{A} \times (\nabla \times \mathbf{B})$ , giving

$$\int_V \nabla \cdot (\mathbf{A} \times (\nabla \times \mathbf{B})) dV = \int_S (\mathbf{A} \times (\nabla \times \mathbf{B})) \cdot \mathbf{m} dS, \quad (2.30)$$

where  $\mathbf{m}$  is a unit normal vector directed outward from  $S$ . Upon expansion of the integrand of the volume integral, a vector analog of Green's first identity is obtained:

$$\begin{aligned} & \int_V (\nabla \times \mathbf{A} \cdot \nabla \times \mathbf{B} - \mathbf{A} \cdot \nabla \times (\nabla \times \mathbf{B})) dV \\ & = \int_S (\mathbf{A} \times (\nabla \times \mathbf{B})) \cdot \mathbf{m} dS. \end{aligned} \quad (2.31)$$

The vector analog of Green's second identity ('Green's theorem') is obtained by reversing the roles of  $\mathbf{A}$  and  $\mathbf{B}$  in (2.31) and subtracting one expression from the other,

$$\begin{aligned} & \int_V (\mathbf{B} \cdot \nabla \times (\nabla \times \mathbf{A}) - \mathbf{A} \cdot \nabla \times (\nabla \times \mathbf{B})) dV \\ & = \int_S (\mathbf{A} \times (\nabla \times \mathbf{B}) - \mathbf{B} \times (\nabla \times \mathbf{A})) \cdot \mathbf{m} dS. \end{aligned} \quad (2.32)$$

Specializing the left-hand side of (2.32) to the case  $\mathbf{A} = \mathbf{E}$  and  $\mathbf{B} = \Gamma$ , it can be rewritten as

$$\int_V (\Gamma \cdot \nabla_P \times (\nabla_P \times \mathbf{E}) - \mathbf{E} \cdot \nabla_P \times (\nabla_P \times \Gamma)) dP. \quad (2.33)$$

Working out the triple products while using that  $\nabla^2 \mathbf{E} = -k^2 \mathbf{E}$ ,  $\nabla \cdot \mathbf{E} = 0$  together with Eq. (2.29) yields

$$-\int_V \mathbf{E} \cdot [\nabla_P (\nabla_P \cdot \Gamma)] dP - \mathbf{E}(Q) \cdot \mathbf{c} = -\mathbf{E}(Q) \cdot \mathbf{c}, \quad (2.34)$$

where we used that, as a consequence of Eq. (2.28),  $\nabla_P \cdot \Gamma = 0$  if  $P$  is on the plane  $\Sigma$ .

Proceeding with the right-hand side of Eq. (2.32) we get

$$\begin{aligned} & \int_{\Sigma} (\mathbf{E} \times (\nabla_P \times \Gamma) - \Gamma \times (\nabla_P \times \mathbf{E})) \cdot \mathbf{m} d\Sigma \\ &= \int_{\Sigma} \mathbf{E} \cdot (\nabla_P \times \Gamma) \times \mathbf{m} d\Sigma, \end{aligned} \quad (2.35)$$

where the contribution of the integration over the hemisphere  $\Sigma'$  has been omitted as it can be made arbitrarily small by letting  $R \rightarrow \infty$  (see Fig. 2.2). Also, we used the fact that the second term on the left-hand side of (2.35) is zero, since  $\Gamma$  is perpendicular to  $\Sigma$  for  $P$  on  $\Sigma$  because then  $G^{(-)} = 0$ . In addition,

$$(\nabla_P \times \Gamma) \times \mathbf{m} = (\nabla_P \times \Gamma)_{\parallel} \times \mathbf{m}, \quad (2.36)$$

where the subscript  $\parallel$  denotes the component parallel to the plane  $\Sigma$ . It is seen from (2.28) that

$$(\nabla_P \times \Gamma)_{\parallel} = 2\nabla_P G \times \mathbf{c}. \quad (2.37)$$

Using (2.36) and (2.37) on the right-hand side of (2.35) gives

$$\begin{aligned} & 2 \int_{\Sigma} [-(\mathbf{E} \cdot \nabla_P G)(\mathbf{c} \cdot \mathbf{m}) + (\mathbf{E} \cdot \mathbf{c})(\nabla_P G \cdot \mathbf{m})] d\Sigma \\ &= 2 \int_{\Sigma} \mathbf{c} \cdot (\mathbf{m} \times \mathbf{E}) \times \nabla_P G d\Sigma. \end{aligned} \quad (2.38)$$

Equating (2.34) and (2.38) (by virtue of (2.32)), and noticing that  $\mathbf{c}$  is an arbitrary vector, we finally find an expression of the field in a point  $Q$  in

terms of its tangential component along the plane  $\Sigma$  only<sup>1</sup>:

$$E(Q) = 2 \int_{\Sigma} (\mathbf{m} \times \mathbf{E}) \times \nabla_P G \, d\Sigma, \quad (2.39)$$

where now, in agreement with Toraldo di Francia's notation, the vector  $\mathbf{m}$  is the *inward* normal to  $\Sigma$ . Note that, as  $Q \rightarrow \Sigma$ , i.e. when the observation point approaches the plane of integration, the assumed boundary condition is regained.

## 2.4 The diffraction integral

The m-theory integral [SMYTHE, 1947; SEVERIN, 1951; TORALDO DI FRANCA, 1955] is used to calculate the diffracted field in medium 2. The solutions satisfy the Maxwell equations. The diffraction integral expresses the diffracted electric field  $\mathbf{E}(\mathbf{x})$  in terms of an integral over a plane of a function of the tangential component of  $\mathbf{E}$ . In a medium with material parameters  $\varepsilon_2$  and  $\mu_2$ , the integral reads

$$\mathbf{E}(\mathbf{x}) = 2 \int_S (\hat{\mathbf{m}} \times \mathbf{E}) \times \nabla G \, d\sigma. \quad (2.40)$$

For  $S$  we take the illuminated (circular) region of the interface, which means that we use Eq. (2.22) for  $\hat{\mathbf{m}} \times \mathbf{E}$ . The Green function  $G$  is defined as

$$G(\mathbf{p}, \mathbf{x}) = \frac{\exp(ik_2 |\mathbf{x} - \mathbf{p}|)}{4\pi |\mathbf{x} - \mathbf{p}|}, \quad (2.41)$$

from which

$$\nabla G = \left( \frac{1}{|\mathbf{x} - \mathbf{p}|} - ik_2 \right) G \hat{e}_G. \quad (2.42)$$

The unit vector  $\hat{e}_G$  is directed from a point  $\mathbf{p}$  on  $S$ , where the integrand is evaluated, to a point  $\mathbf{x}$  where the field is calculated:

$$\hat{e}_G = \frac{\mathbf{x} - \mathbf{p}}{|\mathbf{x} - \mathbf{p}|}. \quad (2.43)$$

---

<sup>1</sup>The name m-theory was coined by Karczewski and Wolf in two papers [KARCZEWSKI AND WOLF, 1966A; KARCZEWSKI AND WOLF, 1966B]. This is due to the fact that the integrand in Eq. (2.39) may be regarded as a magnetic dipole distribution.

The infinitesimal surface element  $d\sigma$  equals the surface element of a sphere with radius  $t(\theta)$  projected from the lens onto the interface (see Eq. (2.13)):

$$d\sigma = t^2(\theta) \tan \theta \, d\theta \, d\phi \quad (0 \leq \theta \leq \Omega), \quad (2.44)$$

with  $\Omega$  the semi-aperture angle of the lens. An equation similar to Eq. (2.40) for the diffracted field  $\mathbf{H}$  can also be derived [SEVERIN, 1951; TORALDO DI FRANCIA, 1955]. However, since we are interested in the intensity (which is proportional to  $|\mathbf{E}|^2$ ), we do not need that expression here. Notice that it is also possible to express the diffracted fields in terms of the tangential component of  $\mathbf{H}$ , rather than the tangential component of  $\mathbf{E}$  [SEVERIN, 1951].

For the moment we restrict ourselves to the case where the observation point  $\mathbf{x}$  lies on the optical or  $z$ -axis. There the intensity distribution is independent of the polarization angle  $\alpha$  (because of cylindrical symmetry). We then have for  $\hat{e}_G$

$$\hat{e}_G = -\frac{f-d}{s(\theta, z)} \begin{pmatrix} \tan \theta \cos \phi \\ \tan \theta \sin \phi \\ 1 - z/(f-d) \end{pmatrix}, \quad (2.45)$$

with  $|\mathbf{x} - \mathbf{p}|$  abbreviated as  $s(\theta, z)$ :

$$s(\theta, z) = [t^2(\theta) + z^2 - 2z(f-d)]^{1/2}, \quad (2.46)$$

where we have used Eq. (2.13). Computation of the integral (2.40) yields (using  $\omega^2 = k_i^2/\varepsilon_i\mu_i$  and  $k_0 = 2\pi/\lambda_0$ , with  $\lambda_0$  the free-space wavelength) that the  $\phi$ -dependence of the  $y$  and  $z$  components of the field is such that they vanish on integration. So after integration with respect to  $\phi$  the total electric field on the axis is given by its  $x$ -component, viz.

$$E_x(0, 0, z) = C \int_0^\Omega \exp[i(k_2s - k_1t)] g(\theta, z) \, d\theta, \quad (2.47)$$

with

$$C(z) = \frac{f}{2}(f-d)^2 \left( \frac{z}{f-d} - 1 \right) \exp[ik_1f] \quad (2.48)$$

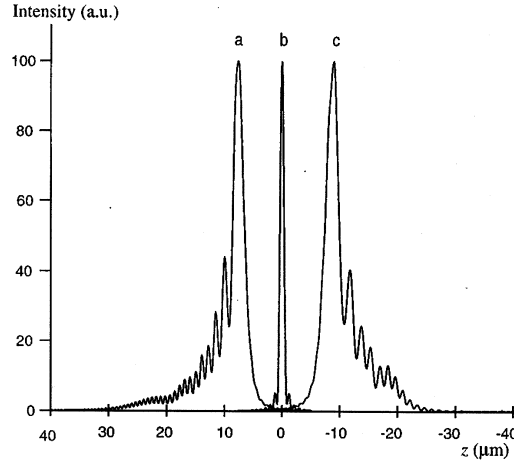


Figure 2.3: Axial intensity distribution (in arbitrary units) for  $n_1 = 1.51$  and  $n_2 = 1.33$  (curve (a)). In the middle is shown the intensity profile without contrast, i.e.  $n_1 = n_2 = 1.51$  (curve (b)). Curve c depicts the intensity for  $n_1 = 1.33$  and  $n_2 = 1.51$ . (For all curves:  $\Omega = 60^\circ$ ,  $\mu_1 = \mu_2 = \mu_0$ ,  $f = 10^{-2}$  m,  $f - d = 50$   $\mu$ m, and  $\lambda = 632.8$  nm). As in all following examples both media are lossless.

and

$$g(\theta, z) = \left( \frac{1}{s^3} - \frac{ik_2}{s^2} \right) (\eta_s + \eta_p \cos \theta') \tan \theta. \quad (2.49)$$

When the point of observation  $\mathbf{x}$  is not on the axis of symmetry, the function  $s(\theta, z)$  gets an additional  $\phi$ -dependence, and hence both  $G$  and  $\nabla G$  in Eq. (2.40) change. A reduction to a one-dimensional integral as just demonstrated, is then no longer possible.

## 2.5 Results

First, a refractive index mismatch gives rise to an aberration-like diffraction pattern. An example is presented in Fig. 2.3. Compared to the intensity distribution without refractive index contrast (curve (b)), we see that the interface induces a dramatic asymmetry and broadening of the intensity profile. A long tail with many relatively high secondary maxima extends in the direction of the interface (curve (a)). The intensity peak is shifted in the same direction.

Using geometrical reasoning it can be shown that the light can reach only a part of the optical axis behind the interface. Let  $h$  be the distance from the interface where a ray with an angle of incidence  $\theta_1$  crosses the  $z$ -axis. We then have

$$h(\theta_1) = (f - d) \frac{\tan \theta_1}{\tan \theta_2} = (f - d) \frac{n_2 \cos \theta_2}{n_1 \cos \theta_1}. \quad (2.50)$$

Here  $\theta_2$  is the angle of propagation after refraction. The index of refraction  $n_i$  for lossless media is given by  $n_i = c (\varepsilon_i \mu_i)^{1/2}$  with  $i = 1, 2$  and  $c$  the speed of light in vacuo. So only the part of the axis between  $h(0)$  and  $h(\Omega)$  is illuminated. For the parameters used for curve (a) of Fig. 2.3 we find that the geometrical shadow boundaries are at  $z = 6.0 \mu\text{m}$  and  $z = 21.8 \mu\text{m}$ . We find that the intensity profile falls indeed within this range.

Whereas for curve (a) of Fig. 2.3  $n_1 > n_2$ , curve (c) represents the intensity profile for the reverse case, namely  $n_1 < n_2$ . We find that the global appearance of the distribution is mirror-imaged with respect to the  $z = 0$  plane. In this case the geometrical shadow boundaries are at  $z = -6.8 \mu\text{m}$  and  $z = -23.5 \mu\text{m}$ . Again, we find a good agreement. All three curves have been normalized to 100. See also Fig. 2.7.

In Figs. 2.4 and 2.5 the iso-intensity lines ('iso-photes') in the  $xy$ - and  $xz$ -planes, respectively, are shown for the same parameters. In Fig. 2.4 the polarization is along the  $x$ -axis. Note that the intensity profile along that axis is somewhat broader than that along the other axis.

In Fig. 2.5 the polarization is again along the  $x$ -axis. In this plane, the intensity peak is narrower in the  $x$ -direction than in the direction of  $z$ . Also, a large number of minima is seen. Figs. 2.4 and 2.5 clearly differ in appearance from their respective counterparts without refractive index contrast [BOIVIN AND WOLF, 1965].

If we move the lens closer to the interface, how much deeper will the point of maximum intensity then lie? This question is answered in Fig. 2.6. For  $n_1 = n_2$  (curve (b)) the intensity peak follows the movement of the lens precisely. For  $n_1 > n_2$  (curve (c)), however, the peak shift lags behind. For the case that  $n_1 < n_2$  (curve (a)), the peak moves further than the lens does. From Eq. (2.50) follows that the paraxial geometrical prediction of the slope equals

$$\frac{\Delta_{\text{peak}}}{\Delta_{\text{lens}}} = - \frac{\partial h(\theta = 0)}{\partial d} = \frac{n_2}{n_1}. \quad (2.51)$$

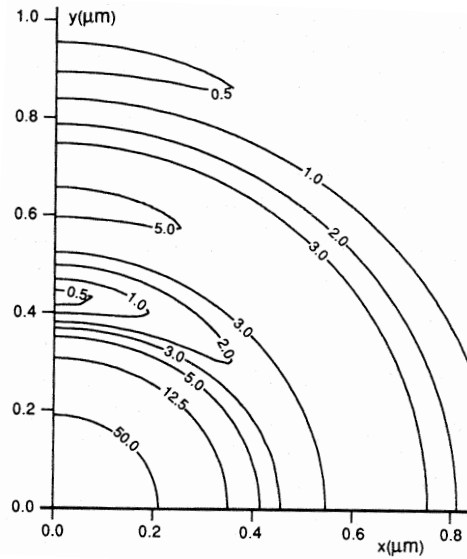


Figure 2.4: Iso-intensity lines (a.u.) in the  $xy$ -plane of maximum intensity ( $z = 7.54 \mu\text{m}$ ). ( $n_1 = 1.51$ ,  $n_2 = 1.33$ ,  $\Omega = 60^\circ$ ,  $\mu_1 = \mu_2 = \mu_0$ ,  $f = 10^{-2} \text{ m}$ ,  $f - d = 50 \mu\text{m}$ , and  $\lambda = 632.8 \text{ nm}$ ).

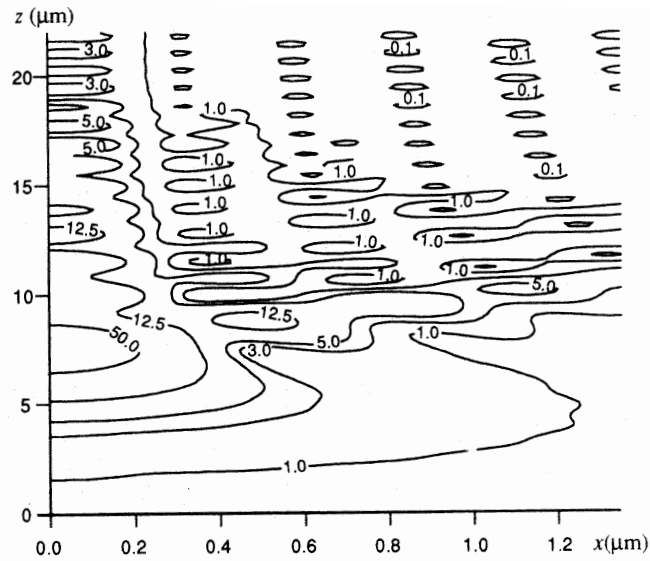


Figure 2.5: Iso-intensity lines (a.u.) in the  $zx$ -plane ( $y = 0$ ). ( $n_1 = 1.51$ ,  $n_2 = 1.33$ ,  $\Omega = 60^\circ$ ,  $\mu_1 = \mu_2 = \mu_0$ ,  $f = 10^{-2} \text{ m}$ ,  $f - d = 50 \mu\text{m}$  and  $\lambda = 632.8 \text{ nm}$ ). N.B. the scale of the two axes is different.

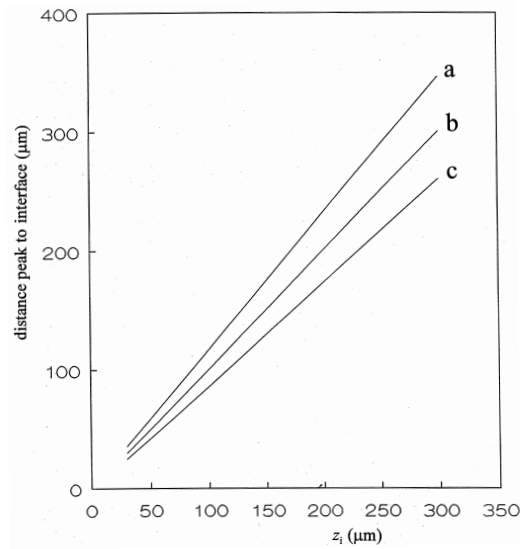


Figure 2.6: The distance between the peak and the interface is plotted versus the position of the lens. (N.B. the distance between the lens and the interface is given by  $d = f - z_i$ .) Only if  $n_1 = n_2$  (curve (b)) does the peak precisely follow the movement of the lens. If  $n_1 > n_2$  (curve (c)), the peak's position shifts less than that of the lens. For  $n_1 < n_2$  (curve (a)) the opposite holds. In all cases  $\Omega = 60^\circ$ ,  $\mu_1 = \mu_2 = \mu_0$ ,  $f = 10^{-2}$  m,  $n_1 = 1.33$ ,  $n_2 = 1.51$ , in the middle curve  $n_1 = n_2 = 1.33$ , and in the lower one  $n_1 = 1.51$ ,  $n_2 = 1.33$ .

As it turns out, this is an acceptable approximation for this range of  $n_i$ , even though  $\Omega$  is large (i.e. non-paraxial).

This effect has great consequences for (confocal) 3-D microscopy, in which one commonly uses oil-immersion objectives ( $n_1 = 1.51$ ) to study watery objects ( $n_2 = 1.33$ ). The shift of the object stage is frequently mistaken for the shift in the point that is imaged. As demonstrated by Visser and Oud [1994], objects may appear much larger (in the  $z$ -direction) than they actually are when this effect is not taken into account.

In Fig. 2.7 the peak intensity is shown for increasing refractive contrast. That is,  $n_2$  is kept at 1.33 while  $n_1$  varies between 1.33 and 1.51. With increasing  $n_1$  the intensity drops dramatically. This is due to two factors: (1) increasing phase differences between waves emanating from different points on the interface, and (2) a decrease in transmission through the interface.

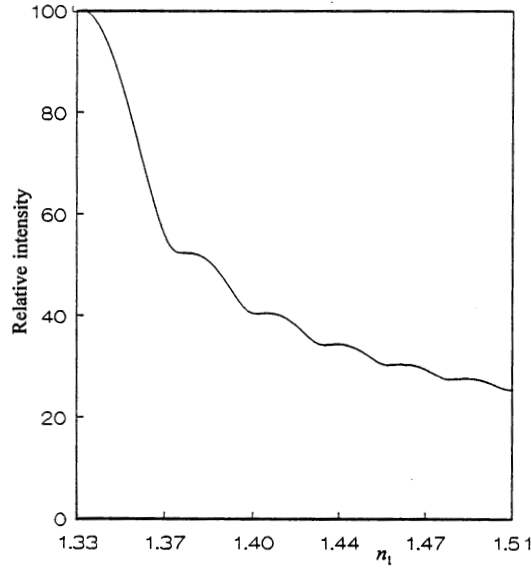


Figure 2.7: Peak intensity (a.u.) versus  $n_1$ . The index of refraction  $n_2$  is fixed at 1.33. ( $\Omega = 60^\circ$ ,  $\mu_1 = \mu_2 = \mu_0$ ,  $f = 10^{-2}$  m,  $f - d = 50 \mu\text{m}$ , and  $\lambda = 632.8$  nm.)

In our examples we have used parameters in the range of practical optics. However, the developed formalism is generally applicable.

## 2.6 Conclusions

We have studied the effects of a plane interface on an incident focused electromagnetic wave. The interface causes a strong broadening of the intensity distribution as compared to the case where there is no interface. Also, the intensity profile becomes highly asymmetrical.

It was found that an increase in the difference (or contrast) in refractive indices  $n_1 - n_2$  leads to a dramatic drop in intensity.

Moving the lens over a distance  $\Delta_{\text{lens}}$  with respect to the interface, causes a shift in the position of the peak intensity called  $\Delta_{\text{peak}}$ . A result with important applications (e.g. for microscopy) is that the intensity peak does not precisely follow the movement of the lens. Instead it was found that  $\Delta_{\text{peak}}/\Delta_{\text{lens}} \sim n_2/n_1$ . In practice, this factor can differ significantly from 1.

**Acknowledgement**

The authors wish to thank Prof. A.T. de Hoop for critical comments.



## **Chapter 3**

# **Comparison of different theories for focusing through a plane interface**

*based on S.H. Wiersma, P. Török, T.D. Visser and P. Varga,  
J. Opt. Soc. Am. 14, pp. 1482–1490 (1997)*

The problem of light focusing by a high-aperture lens through a plane interface between two media with different refractive indices is considered. We compare two recently published diffraction theories and a new geometrical optics description. The two diffraction approaches exhibit axial distributions with little difference. The description based on geometrical optics is shown to agree well with the diffraction optics results. Also, some implications for three-dimensional imaging are discussed.

### 3.1 Introduction

The effect of a dielectric interface on the electromagnetic field has been studied by several workers [GASPER ET AL., 1976; LING AND LEE, 1984; CHANG ET AL., 1994] and [STAMNES, 1986], Chap. 16, pp. 482–500. These theories are usually approximations of some rigorous solutions [LING AND LEE, 1984], however exact solutions of either Maxwell's equations or the wave equation have also been obtained [GASPER ET AL., 1976; CHANG ET AL., 1994].

The subject of focusing of electromagnetic waves by a high-numerical-aperture lens into a homogeneous medium was described by Richards and Wolf [WOLF, 1959; RICHARDS AND WOLF, 1959]. Their work may be regarded as the vectorial generalization of the Debye diffraction formula [DEBYE, 1909]. The focused electromagnetic field is given as a superposition of plane waves, whose propagation vectors all fall inside the geometrical light cone. In a recently published paper, Török *et al.* [1995a] gave a rigorous solution for the problem of focusing through a plane interface, which satisfies both Maxwell's equations and the homogeneous wave equation. This work may be considered as the extension of the Richards–Wolf theory to the case of focusing into an inhomogeneous medium. Another recently published study by Wiersma and Visser [1996] also took the Richards–Wolf theory as a starting point to describe the effect of a plane dielectric interface behind the lens.

Török *et al.* [1995a] obtained the electric and magnetic vectors in the second medium by means of a matrix formalism and then applied a coherent superposition of plane waves to obtain the diffraction pattern. It was shown independently by Wiersma and Visser [1996] (Chapter 2 of this thesis) that it is also possible to obtain the field in the second medium by means of another vectorial diffraction theory. This so-called m-theory [KARCZEWSKI AND WOLF, 1966A; KARCZEWSKI AND WOLF, 1966B] was introduced by several workers. Smythe [1947] and Toraldo di Francia [1955] both used it to describe diffraction by an aperture in a perfectly conducting screen. (The latter treatment is probably the clearest.) Severin [1951] generalized the same formalism to dielectrics. His approach uses the idea that the field in a half-space is completely determined by the tangential component of either the electric or the magnetic field on the plane that bounds the half-

space. It was his insight that this plane can be any mathematical plane, which need not coincide with a physical screen. The m-theory solutions satisfy Maxwell's equations, and the boundary values are reproduced when the observation point, where the field is calculated, is chosen on the plane.

The aim of the present study is to compare the two recently developed theories by Török *et al.* [1995a], and Wiersma and Visser [1996] since they use two completely different methods to describe the effect of a plane interface on a converging spherical wave. Also, a geometrical analysis of this problem is presented, which provides a first approximation of the intensity distribution.

The organization of this paper is as follows. In Section 3.2 we derive the electric-field vector in the second medium. Next, following Török *et al.* [1995a] and Visser and Wiersma [1996], we briefly show in Section 3.3 how the plane wave and m-theory solutions are obtained. This section is concluded with a comparison of the vectorial m-theory and the scalar first Rayleigh–Sommerfeld integral. In Section 3.4 a geometrical optics approximation is presented which is capable of predicting some important features of the intensity distribution in the second medium. Numerical results obtained for the two diffraction theories and the geometrical optics approximation are compared for several examples in Section 3.5. In Section 3.6 some implications of the two theories for three-dimensional imaging are discussed.

## 3.2 The electric vector in the second medium

The geometry of our problem is depicted in Fig. 3.1. It was shown by Török *et al.* [1995a] that the electric vector amplitude in the second medium can be derived by successive application of certain coordinate transformations. These transformations handle the *s*- and *p*-polarized components separately. After introduction of the usual spherical polar coordinate system, with  $\phi$  denoting the azimuthal angle and  $\theta_j$  denoting the polar angle in the first ( $j = 1$ ) and the second ( $j = 2$ ) medium, the electric field in the second medium can be written as

$$\mathbf{E}^{(2)} = \mathbf{R}^{-1}[\mathbf{P}^{(2)}]^{-1} \mathbf{I} \mathbf{P}^{(1)} \mathbf{L} \mathbf{R} \mathbf{E}^{(0)}. \quad (3.1)$$

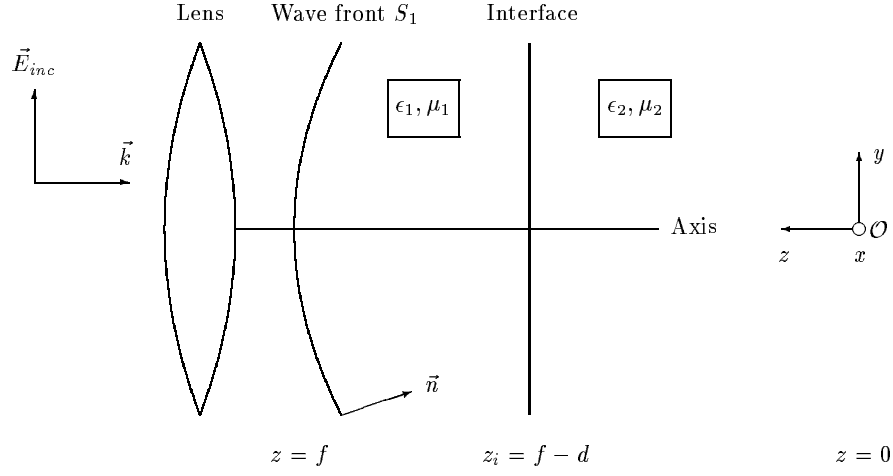


Figure 3.1: Geometry of the system.

Here  $\mathbf{E}^{(0)} = (E_0, 0, 0)$  is the incident electric vector amplitude in front of the lens, which is taken as  $x$ -polarized;

$$\mathbf{R} = \begin{pmatrix} \cos \phi & \sin \phi & 0 \\ -\sin \phi & \cos \phi & 0 \\ 0 & 0 & 1 \end{pmatrix}, \quad (3.2)$$

which describes a rotation of the coordinate system around the optical axis;

$$\mathbf{L} = \begin{pmatrix} \cos \theta_1 & 0 & \sin \theta_1 \\ 0 & 1 & 0 \\ -\sin \theta_1 & 0 & \cos \theta_1 \end{pmatrix}, \quad (3.3)$$

which describes the effect of the lens on ray propagation;

$$\mathbf{P}^{(n)} = \begin{pmatrix} \cos \theta_n & 0 & -\sin \theta_n \\ 0 & 1 & 0 \\ \sin \theta_n & 0 & \cos \theta_n \end{pmatrix}, \quad (3.4)$$

which describes a rotation of the coordinate system around one of the lateral directions, and

$$\mathbf{I} = \begin{pmatrix} \tau_p & 0 & 0 \\ 0 & \tau_s & 0 \\ 0 & 0 & \tau_p \end{pmatrix}, \quad (3.5)$$

which describes the effect of the plane dielectric interface, with  $\tau_p$  and  $\tau_s$  the Fresnel transmission coefficients. From Eq. (3.1) it follows that the electric field immediately to the right of the interface is given by

$$\mathbf{E}^{(2)} = \cos^{1/2} \theta_1 \begin{pmatrix} \tau_p \cos \theta_2 \cos^2 \phi + \tau_s \sin^2 \phi \\ \tau_p \cos \theta_2 \sin \phi \cos \phi - \tau_s \sin \phi \cos \phi \\ -\tau_p \sin \theta_2 \cos \phi \end{pmatrix}. \quad (3.6)$$

Note that Eq. (3.6) can also be obtained from vectorial considerations, as was done by Wiersma and Visser [1996] (cf. Eq. (2.21) of Chapter 2 of this thesis). For the special case that  $\epsilon_1 = \epsilon_2$ , Eq. (3.6) reduces to the expression for the electric field given by Richards and Wolf [1959] for a single homogeneous medium.

Eq. (3.6) for the electric field is used by Török *et al.* [1995a] to obtain an angular spectrum representation in the second medium, whereas Wiersma and Visser [1996] use it in a diffraction integral over the interface. This will be explained in the next two subsections.

### 3.3 The diffraction optics solutions

#### 3.3.1 Plane wave solution

The basis of this solution is that the electromagnetic field just before the interface can be expressed as a superposition integral that adds up all possible plane waves propagating within the divergence angle of the high-aperture lens. Each plane wave is transmitted through the interface. Then we write a similar expression for the field in the second medium, just after the interface. These two expressions must give the same field at the interface or, in other words, the first integral is used as a boundary condition for the second integral. In the first medium and at the interface  $z_i = \lim_{\delta \downarrow 0} f - d + \delta$  (see Fig. 3.1), the incident electric field in an angular spectrum representation is given by [RICHARDS AND WOLF, 1959]

$$\mathbf{E}_1(x, y, z_i) = -\frac{ik_1}{2\pi} \iint_{\Omega_1} \frac{\mathbf{a}(s_{1x}, s_{1y})}{s_{1z}} \exp[ik_1(s_{1x}x + s_{1y}y + s_{1z}z_i)] ds_{1x} ds_{1y}. \quad (3.7)$$

The transmitted field in the second material, at the close vicinity ( $z_i = \lim_{\delta \downarrow 0} f - d - \delta$ ) of the interface is given by

$$\begin{aligned} \mathbf{E}_2(x, y, z_i) = & -\frac{ik_1}{2\pi} \iint_{\Omega_1} \mathbf{M} \frac{\mathbf{a}(s_{1x}, s_{1y})}{s_{1z}} \\ & \times \exp[ik_1(s_{1x}x + s_{1y}y + s_{1z}z_i)] ds_{1x} ds_{1y}, \end{aligned} \quad (3.8)$$

where  $\mathbf{M}$  is an operator describing the transition of the strength vector  $\mathbf{a}$  through the interface,  $k_j$  is the wavenumber,  $\hat{s}_j = (s_{jx}, s_{jy}, s_{jz})$  is the unit vector along a typical ray in the first ( $j = 1$ ) and the second ( $j = 2$ ) medium, and  $\Omega_1$  is the semi-aperture angle of the lens. We represent the field inside the second medium again as a superposition of plane waves. This representation is a solution of the time-independent wave equation and the Maxwell equations, and can be written as

$$\mathbf{E}_2(x, y, z) = -\frac{ik_2}{2\pi} \iint_{\Omega_2} \mathbf{F}(\hat{s}_2) \exp[ik_2(s_{2x}x + s_{2y}y - s_{2z}z)] ds_{2x} ds_{2y}. \quad (3.9)$$

Here  $\mathbf{F}(\hat{s}_2)$  is a function determined by the boundary condition (3.8). By expanding Eq. (3.9) and using spherical polar coordinates we find that the axial distribution of the linearly polarized electric field in the second medium is given by

$$\begin{aligned} E_{2x}(z) = & \frac{ik_1 f l_0}{2} \int_0^{\Omega_1} \sqrt{\cos \theta_1} \sin \theta_1 \exp[i(f-d)(k_1 \cos \theta_1 - k_2 \cos \theta_2)] \\ & \times (\tau_s + \tau_p \cos \theta_2) \exp(-ik_2 z \cos \theta_2) d\theta_1, \end{aligned} \quad (3.10)$$

where  $f$  is the focal length of the lens and  $l_0$  is an amplitude factor. It is emphasized that when off-axis points are computed, the expression for  $\mathbf{E}_2 = (E_{2x}, E_{2y}, E_{2z})$  consists of a linear combination of three integral functions, each containing only a single integral. This makes the numerical evaluation much faster, compared to the case where multiple integrals are to be evaluated.

It is worthwhile analyzing Eq. (3.10). The factor  $\exp[i(f-d)(k_1 \cos \theta_1 - k_2 \cos \theta_2)]$  introduces a phase term in the integral and thus represents an aberration. The amplitude factor  $(\tau_s + \tau_p \cos \theta_2)$  may be regarded as a

polarization-dependent apodization function. The term  $\sqrt{\cos \theta_1}$  is introduced because the lens is assumed to obey the sine condition, and, finally,  $\exp(-ik_2 z \cos \theta_2)$  is the well-known defocus phase factor. It is important to point out that the integration is carried out with the parameters of the first medium, but the integrand is a mixture of quantities of the first and the second media, which also means that when irregular (evanescent) waves are computed [TÖRÖK ET AL., 1996A] it is not necessary to introduce complex contour integration.

### 3.3.2 The m-theory solution

As derived in Section 2.3 of Chapter 2, the m-theory only requires knowledge of the tangential component of the electric field on the integration surface. The electric field within the integration volume, i.e. to the right of the interface in Fig. 3.1, is then completely determined. This is in agreement with the uniqueness theorem [STRATTON, 1941]. As the integration surface  $\Sigma$  we take the plane immediately to the right of the interface, described by  $z = \lim_{\delta \downarrow 0} f - d - \delta$ . In principle,  $\Sigma$  extends to infinity. In the following, the integration area is limited to the intersection of the geometrical light cone with the interface. So, for a high Fresnel number lens obeying the sine condition, this approximation is reasonable as long as the interface does not lie too close to the geometrical focus of the lens at  $z = 0$ . The field that is incident on the interface is taken as the field in the absence of the second medium. The electric field on the integration surface just after the interface is then given by Eq. (3.6).

We recall the expression for the m-theory integral, Eq. (2.39) of Section 2.3 in Chapter 2:

$$\mathbf{E}(Q) = 2 \int_{\Sigma} [\mathbf{m} \times \mathbf{E}(P)] \times \nabla G(P, Q) d\Sigma, \quad (3.11)$$

with  $\mathbf{E}(P)$  given by Eq. (3.6). The normal  $\mathbf{m}$  on the interface  $\Sigma$  points in the positive  $z$ -direction (see Fig. 3.1). The Green function  $G$  is defined as

$$G(P, Q) = \frac{\exp(ik_2 s)}{4\pi s}; \quad (3.12)$$

thus

$$\nabla G = \left( \frac{1}{s} - ik_2 \right) G \frac{\mathbf{Q} - \mathbf{P}}{|\mathbf{Q} - \mathbf{P}|}, \quad (3.13)$$

where  $\mathbf{P}$  and  $\mathbf{Q}$  denote the position vectors of the points  $P$  and  $Q$ , respectively. Also,  $s = |\mathbf{P} - \mathbf{Q}|$ , so

$$s = [t^2(\theta_1) + z^2 - 2z(f - d)]^{1/2}, \quad (3.14)$$

with

$$t(\theta_1) = (f - d) / \cos \theta_1. \quad (3.15)$$

Hence,  $f - t(\theta_1)$  is the path that a ray, travelling at angle  $\theta_1$  from the initial spherical wavefront  $S$  to the interface, traverses. A phase factor  $F(\theta_1)$  and an amplitude factor  $A(\theta_1)$  account for the phase and amplitude change that a ray undergoes along this path:

$$F(\theta_1) = \exp [ik_1 (f - t(\theta_1))] \quad (3.16)$$

and

$$A(\theta_1) = \frac{f \cos^3 \theta_1}{f - d}. \quad (3.17)$$

From these quantities, following Wiersma and Visser [1996] (see Section 2.4 of this thesis), the electric field along the optical axis is given by

$$\begin{aligned} E_{2x}(z) &= \frac{f(f-d)}{2} [z - (f-d)] \int_0^{\Omega_1} (\tau_s + \tau_p \cos \theta_2) \\ &\quad \times \exp\{i[k_2 s + k_1(f-t)]\} \left( \frac{1}{s^3} - \frac{ik_2}{s^2} \right) \tan \theta_1 d\theta_1. \end{aligned} \quad (3.18)$$

It is interesting to compare the axial distribution given by the m-theory and the first Rayleigh–Sommerfeld diffraction integral ( $\text{RS}_1$ ) [MANDEL AND WOLF, 1995] for the general case of diffraction of a wave by a circular aperture  $\mathcal{A}$ . Assume that the aperture is centered on the  $z$ -axis at  $z = f - d$ . The first Rayleigh–Sommerfeld integral for a vector field  $\mathbf{E}$  reads

$$\mathbf{E}_{\text{RS}_1}(x, y, z) = -\frac{1}{2\pi} \int_{\mathcal{A}} \mathbf{E}_0(x_P, y_P, f-d) \frac{\partial}{\partial z} \left[ \frac{\exp(ik_2 R)}{R} \right] d\mathcal{A}, \quad (3.19)$$

with  $x_P$  and  $y_P$  in the aperture  $\mathcal{A}$ , and

$$R = \sqrt{(x - x_P)^2 + (y - y_P)^2 + (z - f + d)^2}. \quad (3.20)$$

As above, the field in the aperture  $\mathbf{E}_0$  is taken as the incident field. We have

$$\frac{\partial}{\partial z} \left[ \frac{\exp(ik_2 R)}{R} \right] = (z - f + d) \left( \frac{ik_2}{R^2} - \frac{1}{R^3} \right) \exp(ik_2 R), \quad (3.21)$$

from which

$$\mathbf{E}_{\text{RS}_1}(x, y, z) = -\frac{z - f + d}{2\pi} \int_{\mathcal{A}} \begin{pmatrix} E_x(P) \\ E_y(P) \\ E_z(P) \end{pmatrix} \left( \frac{ik_2}{R^2} - \frac{1}{R^3} \right) \exp(ik_2 R) d\mathcal{A}. \quad (3.22)$$

In order to compare this with the corresponding result from the m-theory (Eq. (3.11)), we express  $(\mathbf{m} \times \mathbf{E}) \times \nabla G$  with the help of Eqs. (3.13) and (3.14) in terms of

$$\mathbf{P} - \mathbf{Q} = (x_P - x, y_P - y, f - d - z)$$

and

$$s = R = |\mathbf{P} - \mathbf{Q}| = \sqrt{(x_P - x)^2 + (y_P - y)^2 + (z - f + d)^2},$$

and obtain

$$\begin{aligned} (\mathbf{m} \times \mathbf{E}) \times \nabla G &= -\frac{1}{4\pi} \left( \frac{1}{R^3} - \frac{ik_2}{R^2} \right) \exp(ik_2 R) \\ &\times \begin{pmatrix} (z - f + d)E_x(P) \\ (z - f + d)E_y(P) \\ (y - y_P)E_y(P) + (x - x_P)E_x(P) \end{pmatrix}. \end{aligned} \quad (3.23)$$

If we confine the calculation to the  $z$ -axis ( $x = y = 0$ ), then the axial field according to the m-theory is given by

$$\begin{aligned} \mathbf{E}_{\text{m-theory}}(0, 0, z) &= -\frac{z - f + d}{2\pi} \\ &\times \int_{\mathcal{A}} \begin{pmatrix} E_x(P) \\ E_y(P) \\ [y_P E_y(P) + x_P E_x(P)] / (z - f + d) \end{pmatrix} \\ &\times \left( \frac{ik_2}{R^2} - \frac{1}{R^3} \right) \exp(ik_2 R) d\mathcal{A}. \end{aligned} \quad (3.24)$$

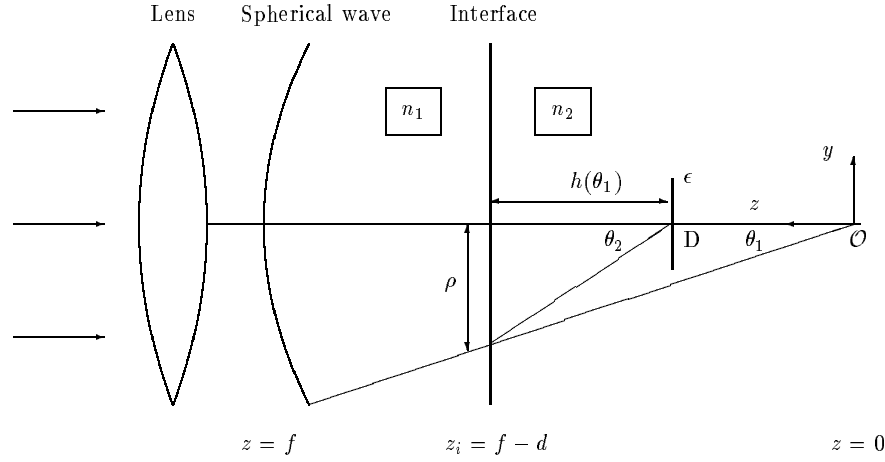


Figure 3.2: Ray tracing for focusing through an interface. A lens with focal length  $f$  and semi-aperture angle  $\Omega_1$  is placed at a distance  $d$  in front of an interface.

From a comparison of Eqs. (3.22) and (3.24), it is seen that the first Rayleigh–Sommerfeld integral and the m-theory predict the same axial field distribution, provided that in Eq. (3.22) the boundary condition for  $(E_x, E_y, E_z)$  in the aperture  $\mathcal{A}$  can be correctly specified, i.e. is taken as the column vector in the integrand of Eq. (3.24). This is an important finding, as the direct application of known diffraction theories is not possible because of the discontinuity at the interface. When, however, the field in the second medium, just after the interface, is specified on the plane of integration,  $\mathcal{A}$ , any diffraction theory can, in principle, be applied.

### 3.4 The geometrical optics approximation

In the previous sections the focusing of converging electromagnetic waves through an interface has been studied by using two different diffraction theories. In this section we show that a much simpler geometrical approach gives a surprisingly good approximation to the intensity distribution.

In contrast to diffraction theory, geometrical optics predicts that the intensity distribution is confined to a finite part of the  $z$ -axis (see Fig. 3.2). Let  $\rho$  denote the distance from the  $z$ -axis at which a ray incident under an

angle  $\theta_1$  crosses the interface. We then have

$$\tan \theta_1 = \frac{\rho}{f - d}. \quad (3.25)$$

If the refracted ray makes an angle  $\theta_2 = \arcsin(n_1 \sin \theta_1/n_2)$  with the  $z$ -axis, then

$$\tan \theta_2 = \frac{\rho}{h(\theta_1)}. \quad (3.26)$$

Eliminating  $\rho$  gives

$$h(\theta_1) = (f - d) \frac{\tan \theta_1}{\tan \theta_2} = (f - d) \frac{n_2 \cos \theta_2}{n_1 \cos \theta_1}, \quad 0 < \theta_1 \leq \Omega_1. \quad (3.27)$$

We note that this expression does not hold for the ray incident at  $\theta_1 = 0$ . However, since this ray corresponds to an infinitely small area of the incident beam, its contribution to the intensity distribution will be negligible. Eq. (3.27) defines two ‘shadow boundaries’ on the  $z$ -axis between which the intensity is concentrated. These boundaries, a marginal one,  $z_m$ , and a paraxial one,  $z_p$ , are at

$$z_m = f - d - h(\Omega_1), \quad (3.28)$$

$$z_p = f - d - \lim_{\theta_1 \downarrow 0} h(\theta_1) = (f - d) \left(1 - \frac{n_2}{n_1}\right). \quad (3.29)$$

The above derivation is only valid if no total internal reflection takes place and we may hence use Snell’s Law.

Every point on the optical axis within the shadow boundaries corresponds to a value of  $\theta_1$ . In order to determine this inverse function, we square Eq. (3.27) to obtain

$$h^2 (1 - \sin^2 \theta_1) = (f - d)^2 (n_2/n_1)^2 [1 - (n_1/n_2)^2 \sin^2 \theta_1]. \quad (3.30)$$

Hence

$$\sin^2 \theta_1(h) = \frac{(f - d)^2 (n_2/n_1)^2 - h^2}{(f - d)^2 - h^2}. \quad (3.31)$$

Using the relation  $h = f - d - z$  (see Fig. 3.2) we finally find that

$$\theta_1 = \arcsin \left[ \frac{(f - d)^2 [(n_2/n_1)^2 - 1]}{2z(f - d) - z^2} + 1 \right]^{1/2} \quad (n_1 \neq n_2). \quad (3.32)$$

In order to calculate the intensity on the  $z$ -axis, we make use of the geometrical law of intensities [BORN AND WOLF, 1997], Chap. 3, pp. 113–117. It should be realized that intensity within the framework of a vectorial diffraction theory is a scalar quantity, whereas in geometrical optics it is an energy flux through a surface.

Consider a disc-shaped detector  $D$ , with a radius  $\epsilon$ , placed perpendicular to the optical axis at a distance  $h$  from the interface (see Fig. 3.2). After we let the diameter of the detector become very small, the flux through its surface as a function of position can be compared with the axial intensity distribution that is predicted by the two vectorial theories.

Let a refracted ray travelling at an angle  $\theta_2$  hit the center of the detector. Also, the rays that intersect the optical axis at a distance  $\Delta h$  on either side of the detector are intercepted. In approximation we have for small detectors,

$$\Delta h \approx \frac{\epsilon}{\tan \theta_2}. \quad (3.33)$$

All these rays lie in the  $\sin \theta_1$  interval in the first medium between  $\sin[\theta_1(h + \Delta h)]$  and  $\sin[\theta_1(h - \Delta h)]$ , with  $\sin[\theta_1(h)]$  given by Eq. (3.31). As the lens is assumed to obey the sine condition

$$r = f \sin \theta_1, \quad (3.34)$$

where  $r = (x^2 + y^2)^{1/2}$  denotes the distance from the axis at which an incident ray enters the lens, all rays between  $r_I = f \sin[\theta_1(h + \Delta h)]$  and  $r_{II} = f \sin[\theta_1(h - \Delta h)]$  will be detected. If the incident beam has a homogeneous intensity distribution, then this implies that the relative total intensity at the detector plane equals

$$I(h; \epsilon) = \pi |r_I^2 - r_{II}^2| \cos[\theta_2(h)]. \quad (3.35)$$

The factor  $\cos \theta_2$  describes the usual flux dependence on the direction of propagation and the orientation of the detector surface.

### 3.5 Numerical results

The distribution of the intensity along the optical axis was computed from Eqs. (3.10) (for Theory 1, the plane wave solution) and (3.18) (for The-

ory 2, the m-theory). A program to evaluate these expressions was written in FORTRAN using the NAG (Numerical Algorithm Group Ltd., Oxford) subroutine package. The numerical computations were performed on an IBM 486DX4 computer. Results were directly visualized using the TECPLOT program. We present results for a lens with numerical aperture  $NA = n_1 \sin \Omega = 1.4$  and a glass/water interface ( $n_1 = 1.54$ ,  $n_2 = 1.33$ ). The focusing depths ( $f - d$ ) were 10, 50 and 100  $\mu\text{m}$ . The wavelength in vacuum was  $\lambda_0 = 488$  nm. The numerical results are shown in Figs. 3.3(a–c) where individual images are normalized to the intensity obtained for  $f - d = 10$   $\mu\text{m}$ . As the figures show, the two theories predict the axial location of the focus (main peak) with excellent agreement. The decrease in peak intensity throughout the computed range agrees well; somewhat greater differences (less than 9%) are found at greater focusing depths. The axial location of the side lobes is the same according to the two theories. It is interesting to note that Theory 1 gives less lobe structure on the negative side of the distributions, but initially it predicts higher lobes on the positive side. The agreement between the two theories is better at smaller focusing depths for the main peak, but as the focusing depth increases, the agreement becomes better for the side lobe structure and worse for the peak intensity. This stems from the different approximations made in Theories 1 and 2 (e.g. neglecting the evanescent waves in the angular spectrum representation (3.8) of Theory 1).

Results of Theory 2 are plotted in Fig. 3.4 for a lens with  $NA = 1.32$  and a wavelength of 632.8 nm (He-Ne laser). The focusing depth was 50  $\mu\text{m}$ . Curve (a) shows the axial intensity distribution for  $n_1 = 1.51$  and  $n_2 = 1.33$ , curve (b) for  $n_1 = n_2 = 1.51$  and curve (c) for  $n_1 = 1.33$  and  $n_2 = 1.51$ . As these figures show, the induced aberration has a profound broadening effect on the intensity distribution. Also, the global appearance of curves (a) and (c) are mirror imaged with respect to the  $z = 0$  plane.

The geometrical intensity, given by Eq. (3.35), is plotted in Fig. 3.5. The lens and media parameters for curves (a) and (b) correspond to those for curves (a) and (c) of Fig. 3.4, respectively. Apart from differences such as (1) a sudden jump from zero to a finite intensity at the geometrical shadow boundary instead of a gradually rising peak, and (2) a smooth instead of a jagged distribution, the overall form of the intensity shows the main characteristics of the electromagnetic diffraction pattern. Notice that the FWHM

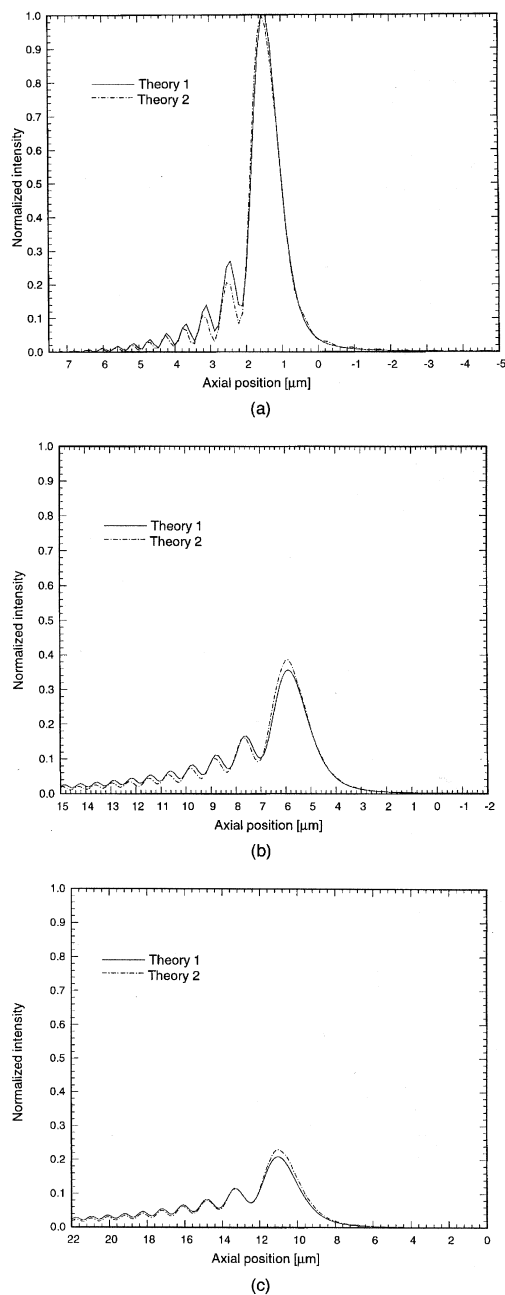


Figure 3.3: Comparison of Theories 1 and 2. The lens numerical aperture was  $\text{NA} = 1.4$  and computations were performed for a glass/water interface ( $n_1 = 1.54$ ,  $n_2 = 1.33$ ) with focusing depths  $f - d$  of 10, 50 and  $100 \mu\text{m}$ . Individual images are normalized to the intensity obtained for  $10 \mu\text{m}$  focusing depth.

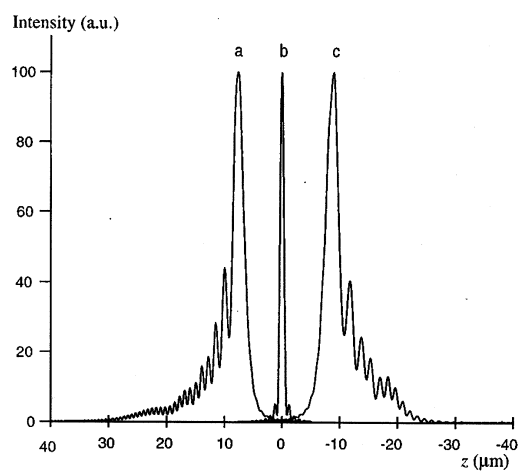


Figure 3.4: Results of Theory 2 for a lens with semi-aperture angle  $60^\circ$  and for a wavelength of 632.8 nm (He-Ne laser). The focusing depth  $f - d = 50 \mu\text{m}$ , focal length  $f = 1 \times 10^{-2} \text{ m}$ ,  $\mu_1 = \mu_2 = \mu_0$ . Curve (a) shows the axial intensity distribution for  $n_1 = 1.51$  and  $n_2 = 1.33$ , curve (b) for  $n_1 = n_2 = 1.51$  and curve (c) for  $n_1 = 1.33$  and  $n_2 = 1.51$ .

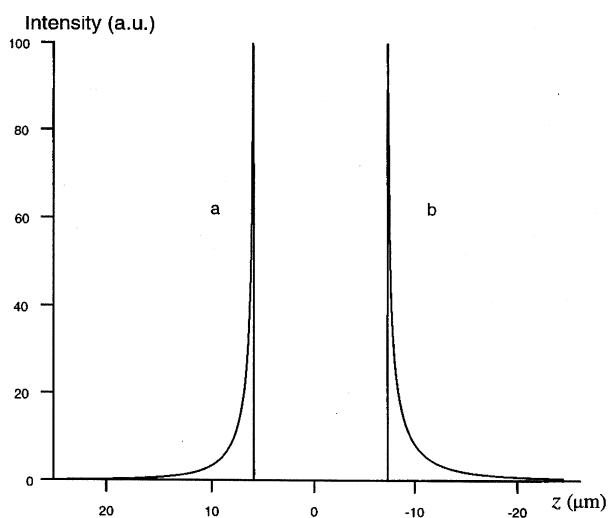


Figure 3.5: Intensity distributions according to geometrical optics. Curves (a) and (b) correspond to Fig. 3.4(a) and (c), respectively. The detector radius  $\epsilon = 1 \times 10^{-8} \text{ m}$ .

of the intensity peak depends through Eq. (3.33) on the radius  $\epsilon$  of the detector.

### 3.6 Consequences for 3-D imaging

Recently it has been pointed out that in 3-D microscopy the size of objects may be severely overestimated [VISSER AND OUD, 1994]. This is also found to be the case when point-like fluorescent objects are imaged [SHEPPARD AND TÖRÖK, 1997]. This elongation effect occurs if there is a refractive index mismatch between the immersion fluid of the objective lens and the cover glass on the one hand, and the medium in which the object is embedded on the other. Typically, the refractive index of the immersion oil is  $n_{\text{oil}} = 1.51$ . For watery biological objects, however, the refractive index is  $n_{\text{water}} = 1.33$ . As we show below, the apparent elongation factor may be quite large under these circumstances.

When a refractive index mismatch occurs there are two separate causes that contribute to the elongation effect:

1. The width of the illumination peak along the  $z$ -axis becomes comparable to the size of the object. If we denote the width of the peak by  $a$  and the true size of the object by  $b$ , then there is a distance  $a + b$ , rather than just  $b$ , where the two overlap and hence a light signal (e.g. fluorescence) is generated.
2. The shift of the object stage during  $z$ -scanning is frequently mistaken to be equal to the shift of the point that is imaged. In practice, however, the latter will be smaller ( $n_1 > n_2$ ) or larger ( $n_2 > n_1$ ).

In Fig. 3.4, curve (a), the first effect is elucidated. Here the vertical illumination distribution is depicted for the case of a watery object imaged by an immersion-oil objective with  $\text{NA} = 1.32$ . As can be seen, the full width at the first minimum (fwfm) of the main peak is  $3.4 \mu\text{m}$ . This is comparable with the typical size of cells ( $\sim 10 \mu\text{m}$ ). So, when the probe is scanned over the object along the  $z$ -axis, there is a trajectory of  $10 + 3.4 \mu\text{m}$  over which a fluorescent signal is generated. Notice that if we approximate a confocal imaging process by taking the square of the axial intensity distribution, then the fwfm does *not* change.

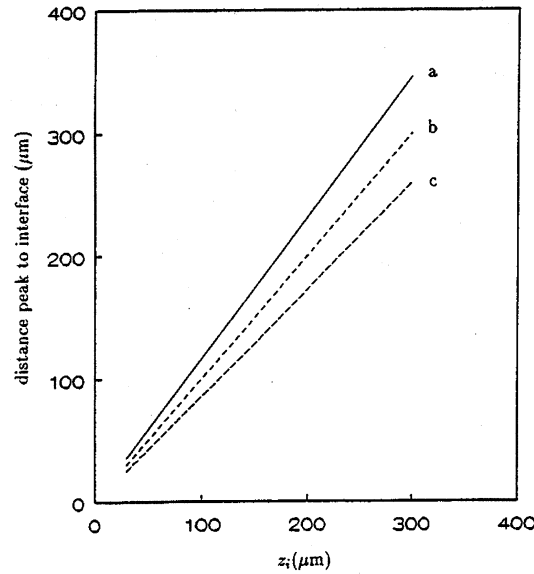


Figure 3.6: Distance between the peak and the interface plotted versus the position of the lens. Only if  $n_1 = n_2$  (curve (b)) does the peak precisely follow the movement of the lens. If  $n_1 > n_2$  (curve (c)) the peak position shifts less than that of the lens. For  $n_1 < n_2$  (curve (a)) the opposite holds. In all cases  $\Omega = 60^\circ$ ,  $\mu_1 = \mu_2 = \mu_0$ ,  $f = 10^{-2}$  cm, and  $\lambda = 632.8$  nm. In curve (a)  $n_1 = 1.33$ ,  $n_2 = 1.51$ , in curve (b)  $n_1 = n_2 = 1.33$ , and in curve (c)  $n_1 = 1.51$ ,  $n_2 = 1.33$ .

The second effect is shown in Fig. 3.6. It follows, in a good approximation, that a  $z$ -shift  $\Delta_z$  of the object stage (or equivalently the lens) results in a shift  $\Delta_z n_1/n_2$  of the object point that is imaged. Effects 1 and 2 together result in the following observation:

*An object with true  $z$ -dimension  $b$ , imaged with an illumination peak of width  $a$ , will appear to have a size:*

$$\text{Apparent size} = \frac{n_1}{n_2} (\text{true size} + \text{peak width}) . \quad (3.36)$$

In [VISSER AND OUD, 1994] cells of  $7.7 \mu\text{m}$  were studied at  $\lambda_0 = 514$  nm,  $n_1 = 1.518$ ,  $n_2 = 1.33$ ,  $\text{NA} = 1.32$ . Expression (3.36) then yields an elongation factor (apparent size divided by true size) of 1.64. This prediction agrees very well with the measured factor of  $1.74 \pm 0.30$ .

There is another interesting consequence of the first effect. If an object with a size much smaller than the size of the illumination distribution is imaged, then the axial scan produces the shape of the distribution rather than the shape of the object. This has been shown for scanning infra-red microscopy by Török *et al.* [1993]. In this way, so-called nanospheres may be used to obtain information on the diffraction pattern.

### 3.7 Conclusions

In this paper we have compared two different diffraction theories that describe the effect of a plane dielectric interface on a converging electromagnetic wave.

For shallow focusing depths our numerical results show, on comparing Theories 1 and 2, that the main axial peaks of the distribution show an excellent agreement. For greater focusing depths the agreement was found to be excellent for the higher order axial lobe structure.

We have also shown that the m-theory and the first Rayleigh–Sommerfeld integral produce the same axial distribution if the boundary conditions are specified correctly.

A geometrical optics approximation describing the main features of the aberrated intensity distribution has been developed. This provides a rapid method to estimate the location of the peak and gives an indication of whether the axial lobe structure is more pronounced on the positive or the negative side of the main peak.

The two diffraction theories can predict the value of the elongation factor that is observed in 3-D microscopy. This calculated elongation factor agrees well with experimental results.

### Acknowledgements

P. Török is on leave from the Central Research Institute for Physics of the Hungarian Academy of Sciences, Budapest. P. Török acknowledges partial support from Wellcome Trust, UK. The authors are grateful to Professor Emil Wolf for his comments on this manuscript.

## Chapter 4

# Annular focusing through a dielectric interface: Scanning and confining the intensity

*based on* S.H. Wiersma, T.D. Visser and P. Török,  
Opt. Lett. 23, pp. 415–417 (1998)  
and  
Pure Appl. Opt. 7, pp. 1237–1248 (1998)

We study the problem of light focusing by a high-aperture lens through a planar interface between two media with different refractive indices. It is demonstrated how, by using annular illumination, the intensity distribution can be significantly confined. A new scanning mechanism is proposed to continuously probe the intensity peak through the second medium. This mechanism may be applied in, for example, lithography and 3-D imaging.

## 4.1 Introduction

The influence of a plane dielectric interface on a converging spherical wave has recently been studied by several groups. Török *et al.* [1995a] use an angular spectrum representation in the Debye approximation. Wiersma and Visser [1996] employ the so-called m-theory. Dhayalan and Stamnes [1998] also use a plane-wave decomposition, but without the Debye approximation. Both Török *et al.* [1995a] and Wiersma and Visser [1996] take the classic papers by Wolf [1959] and Richards and Wolf [1959] as a starting point. Although the analysis in [TÖRÖK ET AL., 1995A] is very different from that in [WIERSMA AND VISSER, 1996], it was found that the numerical results of both studies are in good agreement [WIERSMA ET AL., 1997]. (Note that this comparison was for high Fresnel number systems, outside of the regime of the focal shift phenomenon.) Other studies dealing with the effect of a dielectric interface are [LING AND LEE, 1984; STAMNES AND JIANG, 1998; JIANG AND STAMNES, 1999B].

Focusing through a dielectric interface introduces spherical aberration. The aberrated wavefront may be expanded in terms of, for example, Zernike polynomials [BORN AND WOLF, 1997]. Spherical aberration may be suppressed by counterbalancing the terms in the expansion. This is the basis of adaptive optics and phase mask techniques which are both used to compensate optical path differences. It has, however, been shown by Török *et al.* [1995b] that interface focusing introduces higher order aberration terms which are likely to be difficult to correct by means of adaptive optics. For the same reason spherical aberration caused by interface focusing cannot be fully compensated by altering the tubelength of a lens [SHEPPARD AND GU, 1991] because this only compensates for lower order aberration terms.

A third possibility to reduce aberrations is to use annular illumination rather than an unobscured lens. It is the aim of this paper to explore this option.

Note that a phase mask is optimized for only one focusing depth, whilst adaptive optics solutions an and annulus can, at least in principle, be varied in a continuous manner. As will be explained, this allows one to scan the intensity through the second medium.

The analysis in this paper is fully vectorial. However, in order to increase physical insight, a geometrical optics analysis is presented in the

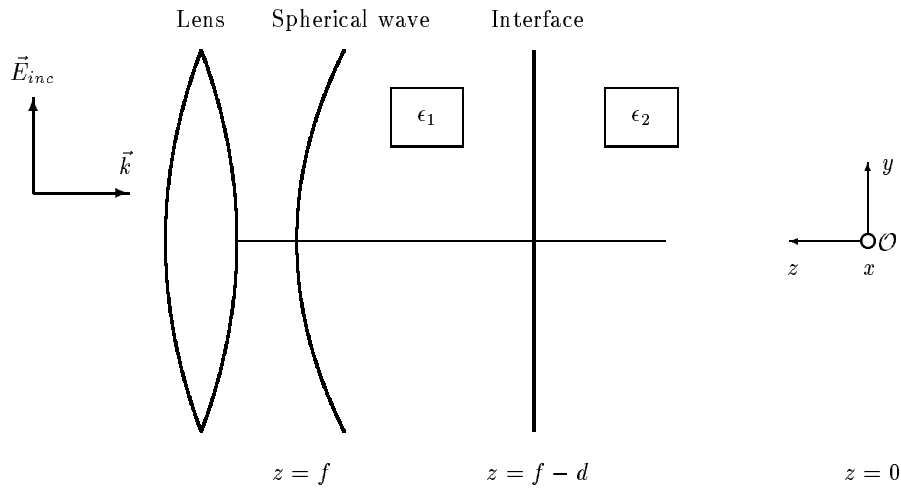


Figure 4.1: Geometry of the system. A linearly polarized plane wave is converted by a lens with focal length  $f$  and semi-aperture angle  $\Omega_1$  into a converging spherical wave. The medium left of the interface has permittivity  $\epsilon_1$ , the medium to the right of the interface has permittivity  $\epsilon_2$ . Both media are assumed to be non-magnetic ( $\mu = \mu_0$ ) and non-conducting ( $\sigma = 0$ ). The system is symmetric with respect to rotations around the  $z$ -axis.

Appendix.

In the examples we use (real-valued) refractive indices ( $n$ ) rather than permittivities ( $\epsilon$ ). The relation between the two is  $n^2 = \epsilon_r$ , with  $\epsilon_r = \epsilon/\epsilon_0$ , where  $\epsilon_r$  is the relative permittivity and  $\epsilon_0$  is the permittivity *in vacuo*.

In this paper we are concerned with the time-averaged electric energy density, hereafter simply called ‘the intensity’.

## 4.2 The effect of an interface on an unobscured focused beam

The geometry of our problem is depicted in Fig. 4.1. A lens focuses an incident, linearly polarized, plane wave through a dielectric interface. The interface is perpendicular to the direction of propagation ( $-z$ ). For the calculations in this section the results of [WIERSMA AND VISSER, 1996] are used.

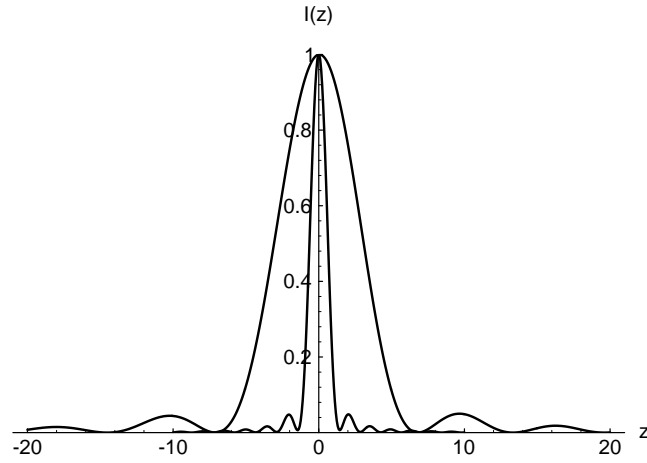


Figure 4.2: Intensity distribution along the  $z$ -axis (in  $\mu\text{m}$ ) for two semi-aperture angles when  $n_1 = n_2$ . The narrow peak is for  $\Omega_1 = 45^\circ$ , the broad distribution is for  $\Omega_1 = 20^\circ$ . The other parameters in both cases are  $\lambda_0 = 632.8 \text{ nm}$ ,  $n_1 = n_2 = 1.51$ ,  $f = 10^{-2} \text{ m}$ .

If there is no interface (i.e.  $n_1 = n_2$ ), then an increasing semi-aperture angle  $\Omega_1$  will result in a decreasing width of the peak of the axial intensity distribution, as is shown in Fig. 4.2. This situation changes completely when an interface is present. As is seen in Fig. 4.3, the axial distribution for  $\Omega_1 = 45^\circ$  is highly asymmetric and has a jagged appearance. For a *smaller* aperture angle, namely  $\Omega_1 = 20^\circ$ , the distribution is now much narrower. However, for  $\Omega_1 = 10^\circ$  it is seen that the peak is wider again. So, it seems that for a given configuration there exists an optimum value of the semi-aperture angle for which the axial diffraction pattern is the most localized. This can be understood by realizing that there are two competing processes at work. An increasing numerical aperture decreases the axial resolution as in Fig. 4.2. At the same time, however, an increasing aperture angle causes an increasing phase difference between the secondary Huygens sources at the interface, giving rise to a widening of the axial diffraction pattern [TÖRÖK ET AL., 1996B].

The broadening of the intensity distribution due to an interface (which increases with increasing focusing depth) has major implications for three-dimensional imaging (see also Section 3.6 of this thesis and [VISSER AND OUD, 1994; TÖRÖK ET AL., 1997]). For confocal microscopy, where high

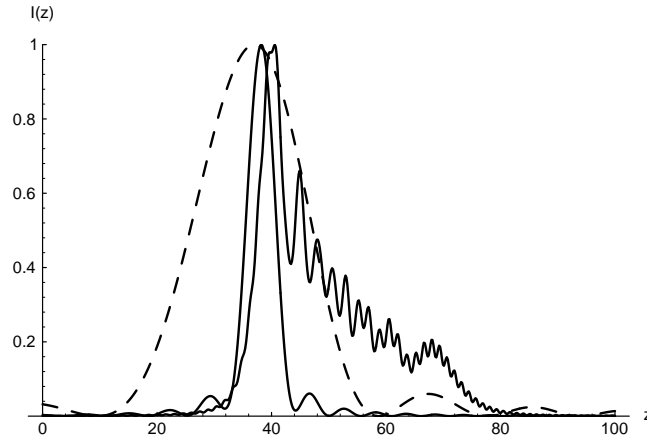


Figure 4.3: Comparison of the intensity distribution along the  $z$ -axis (in  $\mu\text{m}$ ) for three different semi-aperture angles. The wide symmetric peak is for  $\Omega_1 = 10^\circ$  (dashed curve), the narrow symmetric peak is for  $\Omega_1 = 20^\circ$ , and the broad, jagged distribution is for  $\Omega_1 = 45^\circ$ . The other parameters in all cases are  $\lambda_0 = 632.8 \text{ nm}$ ,  $n_1 = 1.51$ ,  $n_2 = 1.33$ ,  $f - d = 300 \mu\text{m}$ ,  $f = 10^{-2} \text{ m}$ .

numerical aperture oil-immersion lenses with  $n_{\text{oil}} = 1.51$  are commonly used to study biomedical objects with  $n_{\text{water}} = 1.33$ , this dependence of the peak width on  $\Omega_1$  indicates that lower aperture angles can improve the optical sectioning capabilities.

### 4.3 Stationary phase and geometrical optics

In [WIERSMA AND VISSER, 1996] it was derived (see Chapter 2 of this thesis) that for an unobscured lens the axial electric field in the second medium is given by

$$E_x(z) = C(z) \int_0^{\Omega_1} e^{ik_2s - ik_1t} g(\theta_1, z) d\theta_1, \quad (4.1)$$

with

$$C(z) = \frac{f}{2}(f-d)^2 \left( \frac{z}{f-d} - 1 \right) \exp(ik_1f), \quad (4.2)$$

$$g(\theta_1, z) = \left( \frac{1}{s^3} - \frac{ik_2}{s^2} \right) (\eta_s + \eta_p \cos \theta_2) \tan \theta_1. \quad (4.3)$$

The suffix  $x$  in Eq. (4.1) indicates that the incident plane wave is linearly polarized along the  $x$ -direction. Also,  $f - d$  is the distance between the focus of the lens and the interface,  $k_i$  ( $i = 1, 2$ ) is the wavenumber in medium  $i$ ,  $\eta_s$  and  $\eta_p$  are Fresnel transmission coefficients. The angle  $\theta_2$  follows from  $\theta_1$  through Snell's law. The functions  $s$  and  $t$  are defined as

$$t(\theta_1) = \frac{f - d}{\cos \theta_1}, \quad (4.4)$$

$$s(\theta_1) = (t^2 + z^2 - 2z(f - d))^{1/2}. \quad (4.5)$$

In order to get more insight into the physics of the situation, we now develop a stationary phase analysis of this integral [STAMNES, 1986], Chap. 8 and Section 16.2. The phase of the exponent in Eq. (4.1) is stationary if

$$\frac{d}{d\theta_1}(k_2 s - k_1 t) = 0, \quad (4.6)$$

which is readily translated into

$$\left(k_2 \frac{t}{s} - k_1\right) \frac{dt}{d\theta_1} = 0. \quad (4.7)$$

For  $f \neq d$ , one solution is  $dt/d\theta_1 = 0$ . From Eq. (4.4) it follows that this is for  $\theta_1 = 0$ . However, since the amplitude function  $g(\theta_1 = 0) = 0$ , this stationary end-point yields a contribution of order  $1/k$  to the integral and is neglected. The contribution of the non-stationary end-point at  $\theta_1 = \Omega_1$  is also of order  $1/k$ , and is neglected too. Another solution is

$$k_2 t = k_1 s. \quad (4.8)$$

Using that  $k_i = n_i k_0$ , with  $i = 1, 2$  and  $k_0$  the wavenumber *in vacuo* together with Eqs. (4.4) and (4.5) this gives

$$\frac{z^2}{t^2} - 2\frac{z}{t} \cos \theta_1 + 1 - \frac{n_2^2}{n_1^2} = 0. \quad (4.9)$$

Solving this for  $z/t$  yields

$$\begin{aligned} \frac{z}{t} &= \cos \theta_1 \pm \sqrt{\cos^2 \theta_1 - 1 + \left(\frac{n_2}{n_1}\right)^2} \\ &= \cos \theta_1 \pm \frac{n_2}{n_1} \sqrt{1 - \sin^2 \theta_2} \\ &= \cos \theta_1 \pm \frac{n_2}{n_1} \cos \theta_2. \end{aligned} \quad (4.10)$$

Using Eq. (4.10) together with Eq. (4.4) gives

$$z = f - d \pm \frac{n_2}{n_1}(f - d) \frac{\cos \theta_2}{\cos \theta_1}. \quad (4.11)$$

Defining the *positive* depth  $h$  below the interface as

$$h = f - d - z \quad (4.12)$$

gives

$$h = (f - d) \frac{n_2 \cos \theta_2}{n_1 \cos \theta_1}. \quad (4.13)$$

Eq. (4.13) expresses a relation between the axial position  $h$  and the angle  $\theta_1$  which gives the main contribution to the integral of Eq. (4.1). This is exactly Eq. (A.3) of Appendix A which was derived using Snell's Law. This is an illustration of the fact that for  $k \rightarrow \infty$  (as is implicitly assumed in stationary phase analysis) wave optics reduces to geometrical optics. It also means that the main contribution to the asymptotic expansion of Eq. (4.1) vanishes outside the so-called geometrical shadow boundaries (see also Appendix A).

We continue the analysis of Eq. (4.1) by squaring condition (4.13) and re-writing it as

$$\sin \theta_s(z) = \left[ \frac{h^2 - (f - d)^2 (n_2/n_1)^2}{h^2 - (f - d)^2} \right]^{1/2}, \quad (4.14)$$

where the suffix  $s$  indicates the value of  $\theta_1$  for which the phase is stationary at position  $z$ . Eq. (4.14) represents an interior stationary point. Hence, the asymptotic expansion of Eq. (4.1) is given in first order as [STAMNES, 1986; MANDEL AND WOLF, 1995]

$$E_x(z) \sim \left[ \frac{2\pi}{|k_2 s''(\theta_s) - k_1 t''(\theta_s)|} \right]^{1/2} g(\theta_s, z) C(z) e^{i(k_2 s(\theta_s) - k_1 t(\theta_s))} e^{\pm i\pi/4}. \quad (4.15)$$

Here the upper (lower) sign is taken according as to  $k_2 s''(\theta_s) - k_1 t''(\theta_s)$  is greater (smaller) than zero. Also, using condition (4.8),

$$k_2 s''(\theta_s) - k_1 t''(\theta_s) = \frac{k_2}{s} \left( 1 - \frac{k_1^2}{k_2^2} \right) t'^2. \quad (4.16)$$

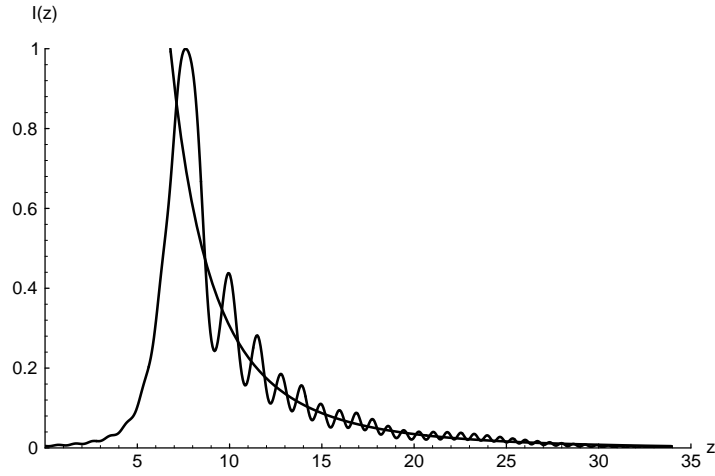


Figure 4.4: Comparison of an asymptotic approximation Eq. (4.17) (smooth curve) and the exact expression Eq. (4.1) (jagged curve) for the axial intensity. In this example  $\lambda_0 = 632.8$  nm,  $\Omega = 60^\circ$ ,  $f - d = 50$   $\mu$ m,  $n_1 = 1.51$ ,  $n_2 = 1.33$ .

So, for the intensity we find

$$I(z) = \frac{1}{4}\epsilon_2|E(z)|^2 \sim \frac{\epsilon_2\pi s(\theta_s)}{2k_2|1 - (k_1/k_2)^2|t'(\theta_s)^2}|g(z)C(z)|^2. \quad (4.17)$$

A comparison of the exact expression (4.1) and the asymptotic approximation (4.17) is depicted in Fig. 4.4. Note that the first order approximation shows no interference pattern. Also, contrary to the exact solution, it exists only between the two geometrical shadow boundaries. Finally, the asymptotic expression slightly displaces the maximum.

#### 4.4 Annular illumination: Localizing the intensity

From Fig. 4.4 it is seen that the intensity distribution can have many secondary maxima. Just as by decreasing the semi-aperture angle (Fig. 4.3), we can reduce the number of maxima by using an annular aperture. This has the additional advantage that the light can be ‘aimed’ to have a peak around any axial position  $z$ , provided that  $z$  lies between the geometrical shadow boundaries of the unobscured lens.

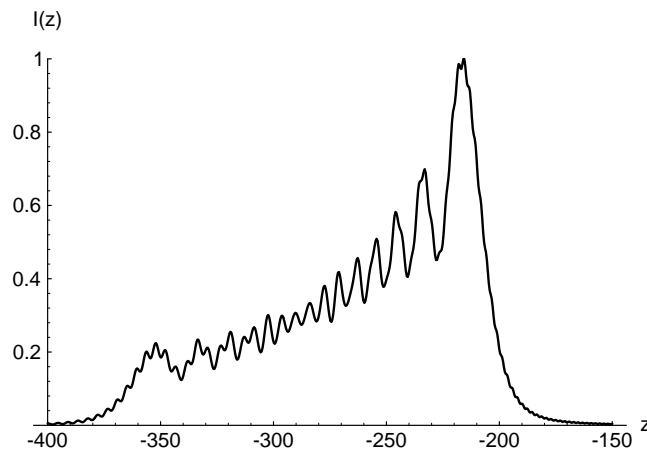


Figure 4.5: Intensity distribution according to Eq. (4.1) along the  $z$ -axis (in  $\mu\text{m}$ ) for an unobscured lens.  $\lambda_0 = 632.8 \text{ nm}$ ,  $\Omega_1 = 50^\circ$ ,  $f = 10^{-2} \text{ m}$ ,  $f - d = 200 \mu\text{m}$ ,  $n_1 = 1.00$ ,  $n_2 = 2.00$ . Note that the peak intensity here corresponds to 2.9% of the peak intensity of the case  $n_1 = n_2 = 1.00$ .

For a given configuration (i.e. the set of parameters  $\Omega_1$ ,  $f$ ,  $d$ ,  $\lambda_0$ ,  $n_1$  and  $n_2$ ) one can find for any position  $z$  between the shadow boundaries the value of  $\theta_s(z)$  through Eq. (4.14). From the considerations of the previous section it follows that by restricting the illumination to an interval around  $\theta_s(z)$  most of the intensity will be found in the vicinity of  $z$ . (In practice, the annulus can be placed at different positions: at the back focal plane [GAN ET AL., 1997], at the exit pupil or at the dielectric interface.) To illustrate this, consider the axial diffraction pattern for an unobscured lens shown in Fig. 4.5. The intensity distribution is relatively spread out, and exhibits many secondary peaks. It was found that the peak intensity in this case is 2.9% of that which occurs for  $n_1 = n_2 = 1.00$  (keeping all other parameters fixed).

Suppose now that we want to concentrate the intensity around the secondary peak at  $z = -302.3 \mu\text{m}$ . For this particular configuration  $\theta_s(z = -302.3 \mu\text{m}) = 41.2^\circ$ , according to Eq. (4.14). By using an annulus around this value, the light can indeed be localized around the prescribed  $z$  value. The dependence of  $I(z)$  on the annular interval limits  $\theta_{\text{low}}$  and  $\theta_{\text{high}}$  is depicted in Fig. 4.6. The optimized interval (i.e. giving the highest intensity) is determined numerically. The intensity distribution for this annulus is

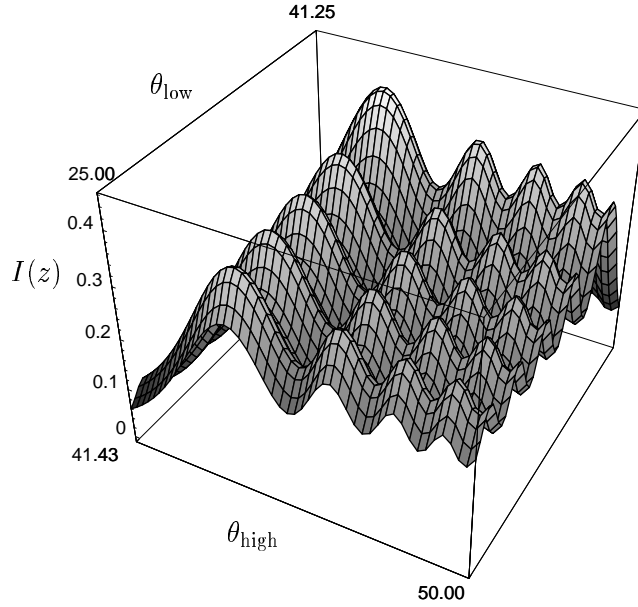


Figure 4.6: The intensity  $I(z = -302.3 \mu\text{m})$  as a function of the angular interval limits  $\theta_{\text{low}}$  and  $\theta_{\text{high}}$ . All parameters are as in Fig. 4.5.

shown in Fig. 4.7 (left curve). A sharply enhanced (51%) single peak centered around  $z = -302.3 \mu\text{m}$  is indeed obtained. Also, the number of secondary maxima and their heights are both strongly reduced. If we change the annulus, the intensity peak can be shifted to, e.g.,  $z = -246 \mu\text{m}$  (right curve). We conclude that by adjusting the annulus we can ‘aim’ the light to be focused anywhere between the geometrical shadow boundaries. Note that one can also localize the intensity around the peak of the distribution for the unobscured lens (i.e. at  $z = -215 \mu\text{m}$  in Fig. 4.5).

The optimized values of  $\theta_{\text{low}}$  and  $\theta_{\text{high}}$  as a function of  $z$  are depicted in Fig. 4.8. The optimal angular interval always includes the stationary phase angle  $\theta_s(z)$ . Note that  $\theta_{\text{low}}$  suddenly becomes nonzero around the position of the original maximum. This is related to the fact that the paraxial rays, which together make up the maximum peak for the case of an unobscured lens, gradually get out of phase with the rays around  $\theta_{\text{stat}}(z)$  as  $z$  becomes more negative. Therefore, from a certain  $z$ -value onwards, these paraxial rays are no longer part of the optimized annulus. Also, it is seen that from certain  $z$ -values on  $\theta_{\text{high}} = 50^\circ$ . This is due to the fact that  $\theta_{\text{high}}$  cannot

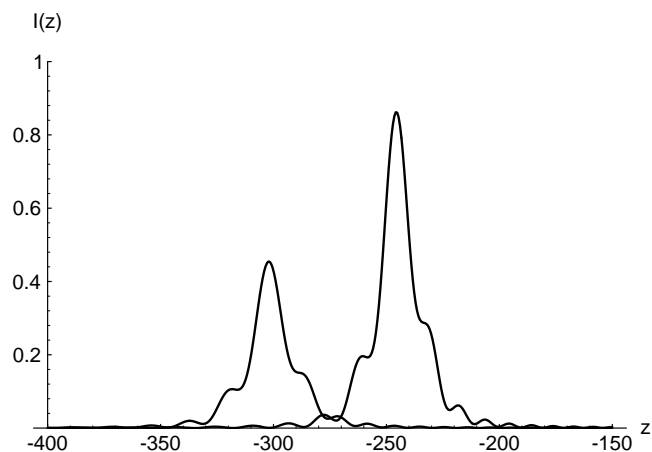


Figure 4.7: Intensity distributions along the  $z$ -axis (in  $\mu\text{m}$ ) for the optimized annuli  $[37.8^\circ, 44.2^\circ]$  (left curve), and  $[23.6^\circ, 34.3^\circ]$  (right curve). The peak intensity is increased by 51% and 48%, respectively. All parameters are as in Fig. 4.5.

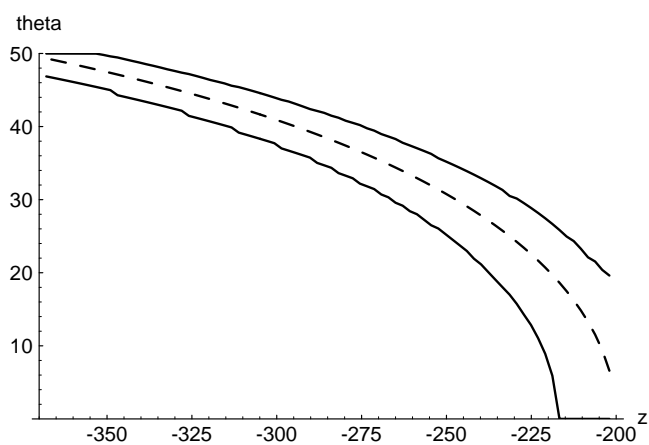


Figure 4.8: The stationary phase  $\theta_{\text{stat}}$  (dashed curve), and the two interval limits  $\theta_{\text{low}}$  (lower curve) and  $\theta_{\text{high}}$  (upper curve) which give an optimal intensity as a function of the axial position  $z$  (in  $\mu\text{m}$ ). All parameters are as in Fig. 4.5.

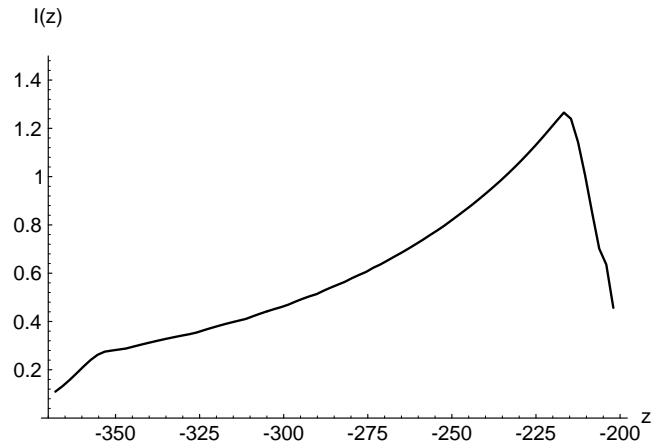


Figure 4.9: The maximum intensity that can be obtained by optimizing the annulus, as a function of the axial position  $z$  (in  $\mu\text{m}$ ). The normalization, as well as all other parameters, are as in Fig. 4.5.

exceed  $\Omega_1$ .

The maximum intensity, as produced by optimizing the angular interval, is shown in Fig. 4.9. Note that, although this is a smooth distribution, the general form of the diffraction pattern in Fig. 4.5 can still be recognized. For certain applications it may be desirable to have a constant peak intensity while scanning through the second medium. The curve in Fig. 4.9 indicates how the incident power should be adjusted as a function of  $z$  to obtain this.

## 4.5 Conclusions

We have analyzed the effect of a plane dielectric interface on a converging spherical wave. A relation between the requirement of stationary phase and the geometrical description of the focusing process was established.

It was found that by using a well-chosen annulus the axial intensity distribution can be significantly confined, and the secondary maxima strongly suppressed. Moreover, the local intensity can be increased in this manner.

It was shown how by continuously varying the annulus and the input power, a constant intensity peak can be scanned axially (within certain limits) through the second medium. This new scanning method has possible applications in, e.g., 3-D imaging and lithography.

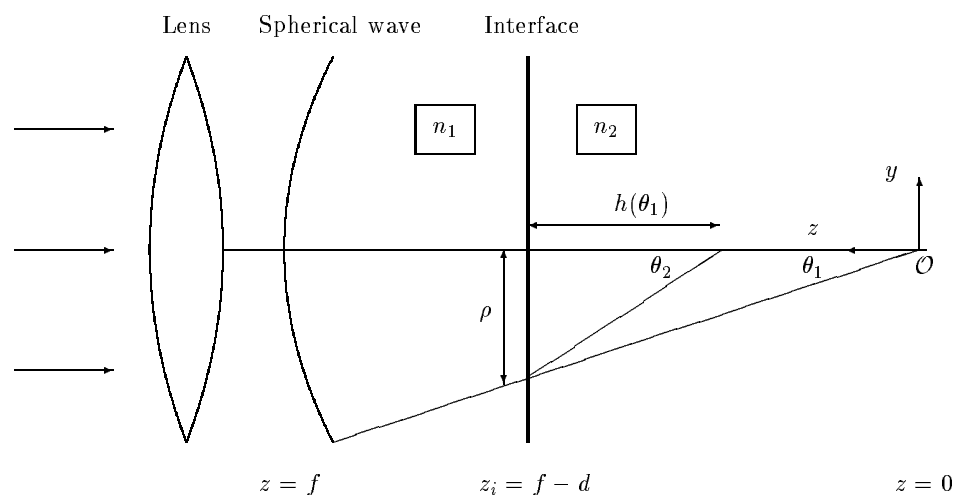


Figure 4.10: Ray tracing for focusing through an interface. A lens with focal length  $f$  and semi-aperture angle  $\Omega_1$  is placed at a distance  $d$  in front of an interface between two media. A typical ray which is incident under an angle  $\theta_1$  passes the interface at a distance  $\rho$  from the  $z$ -axis. After refraction, it crosses the axis at a distance  $h$  from the interface.

## Appendix A. Geometrical Optics Analysis

In this Appendix<sup>1</sup> we analyze our problem from a geometrical optics point of view. We discuss the axial focal displacement associated with the aberration caused by the interface, and the so-called geometrical shadow boundaries. The latter are relevant for the stationary phase analysis of Section 4.3.

Let  $\rho$  denote the distance from the  $z$ -axis at which a ray incident under an angle  $\theta_1$  crosses the interface (see Fig. 4.10). We then have

$$\tan \theta_1 = \frac{\rho}{f - d}. \quad (\text{A.1})$$

If the refracted ray makes an angle  $\theta_2 = \arcsin(n_1 \sin \theta_1 / n_2)$  with the  $z$ -axis,

<sup>1</sup>In this Appendix we elucidate the connection between geometrical optics and the stationary phase approximation. In Section 3.4 the axial intensity distribution according to geometrical optics was derived. It turns out that both the stationary phase approximation and the geometrical optics intensity distribution only exist between the two geometrical shadow boundaries.

then

$$\tan \theta_2 = \frac{\rho}{h(\theta_1)}. \quad (\text{A.2})$$

Here  $h(\theta_1)$  is the distance between the interface and the point where the refracted ray crosses the  $z$ -axis. Eliminating  $\rho$  gives

$$h(\theta_1) = (f - d) \frac{\tan \theta_1}{\tan \theta_2} = (f - d) \frac{n_2 \cos \theta_2}{n_1 \cos \theta_1}, \quad 0 < \theta_1 \leq \Omega_1. \quad (\text{A.3})$$

(Note that this expression does not hold for the ray incident at  $\theta_1 = 0$ .) From Fig. 4.10 it is clear that the refracted ray crosses the  $z$ -axis at  $z = f - d - h(\theta_1)$ . In other words, the interface introduces an axial focal displacement  $\Delta_f(\theta_1)$  of

$$\Delta_f(\theta_1) = (f - d) \left( 1 - \frac{n_2 \cos \theta_2}{n_1 \cos \theta_1} \right). \quad (\text{A.4})$$

For  $n_1 = n_2$  there is no focal displacement. In that case Eq. (A.4) reduces to  $\Delta_f = 0$ , as expected.

In contrast to diffraction theory, geometrical optics predicts that the intensity distribution is confined to a finite part of the  $z$ -axis in the second medium. Eq. (A.3) defines two ‘shadow boundaries’ on the  $z$ -axis between which the intensity is concentrated. Although, as remarked above, this equation does not hold for  $\theta_1 = 0$ , this ray corresponds to an infinitely small area of the incident beam, its contribution to the intensity distribution is negligible. Therefore, these shadow boundaries, a marginal one  $z_m$  and a paraxial one  $z_p$ , are at

$$z_m = f - d - h(\Omega_1), \quad (\text{A.5})$$

$$z_p = f - d - \lim_{\theta_1 \downarrow 0} h(\theta_1) = (f - d) \left( 1 - \frac{n_2}{n_1} \right). \quad (\text{A.6})$$

Note that for  $n_2 \neq n_1$  both  $z_p$  and  $z_m$  are finite. The above derivation is only valid if no total internal reflection takes place and we may hence use Snell’s Law.

Every point  $z$  on the optical axis within the shadow boundaries corresponds to a single value of  $\theta_1$ . In order to determine this inverse relation, Eq. (A.3) is squared to obtain

$$h^2 (1 - \sin^2 \theta_1) = (f - d)^2 (n_2/n_1)^2 [1 - (n_1/n_2)^2 \sin^2 \theta_1], \quad (\text{A.7})$$

or

$$\sin^2 \theta_1(h) = \frac{(f-d)^2 (n_2/n_1)^2 - h^2}{(f-d)^2 - h^2}, \quad (\text{A.8})$$

cf. Eq. (4.14). Using that  $h = f - d - z$  (see Fig. 4.10) we finally find that

$$\theta_1 = \arcsin \left[ \left( \frac{(f-d)^2 [(n_2/n_1)^2 - 1]}{2z(f-d) - z^2} + 1 \right)^{1/2} \right], \quad (n_1 \neq n_2). \quad (\text{A.9})$$

As is shown in Section 4.3, the main contribution to the intensity at axial position  $z$  comes precisely from the ray which is incident under  $\theta_s = \theta_1$  with  $\theta_1$  given by Eq. (A.9).



## **Chapter 5**

# **Reflection-induced spectral changes of the pulsed radiation emitted by a point source. Part I: Theory**

S.H. Wiersma, T.D. Visser and A.T. de Hoop, submitted for publication

We calculate the field emitted by a pulsed point source above a planar interface. It is found that the observed power spectrum can differ significantly from the emitted spectrum. Also, the observed power spectrum depends strongly on the wavespeeds in the two media and on the position of the observation point with respect to the interface. In this Chapter the necessary formalism is developed. Numerical results are presented in Chapter 6.

## 5.1 Introduction

The power density spectrum of the wavefield that is observed at a certain distance from its emitting source usually differs from the one of the source excitation. Examples of this are known in the fields of optics and acoustics. There are, within the linear regime, at least five different mechanisms which can cause this. First, we mention the Doppler effect which manifests itself when the source and the observer are in relative motion [VAN BLADEL, 1984]. Secondly, when a pulsed wave propagates through an absorbing medium, the interplay of dispersion and absorption (in accordance with the principle of causality) causes changes in the spectrum of the wave field [OUGHSTUN AND SHERMAN, 1997]. Thirdly, partially coherent sources give rise to so-called correlation-induced spectral changes [BOCKO ET AL., 1987]. A fourth, and closely related, mechanism is scattering by a random medium. An overview of the latter two processes and their consequences for the wavefield's power density spectrum are described in [MANDEL AND WOLF, 1995] and [WOLF AND JAMES, 1996]. In the present paper we study a fifth cause of spectral changes, namely reflection at an interface.

We analyze how reflection at a planar interface between two media with different wavespeeds changes the spectrum of a propagating wave emitted by a pulsed point source. This effect is studied both as a function of the wavespeeds in the two media and in its dependence on the point of observation relative to the source and the interface. As will be demonstrated, the changes in the observed power spectrum can be quite significant.

The analysis of the pulse propagation in the two-media configuration is carried out with the use of the modified Cagniard technique [CAGNIARD, 1939; DE HOOP, 1960]. This method has been successfully applied in electromagnetics [DE HOOP AND FRANKENA, 1960; DE HOOP, 1979], acoustics [DE HOOP AND VAN DER HIJDEN, 1984A; DE HOOP AND VAN DER HIJDEN, 1984B], and elastodynamics [DE HOOP AND VAN DER HIJDEN, 1985; VAN DER HIJDEN, 1987]. In the present study we consider scalar wavefields. In our numerical examples, the parameters are taken from acoustics. In addition, pulse time widths are chosen such that within the spectral regime dispersion can be neglected.

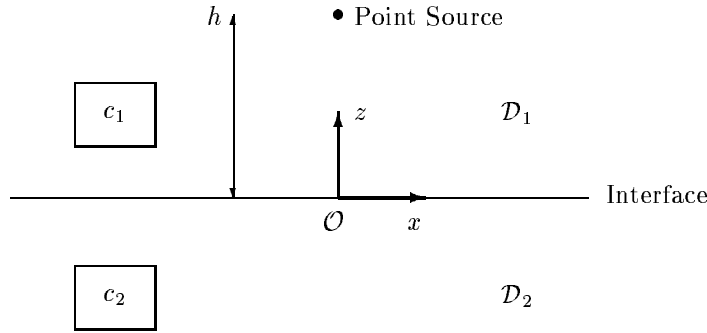


Figure 5.1: A point source above a planar interface. The source is located on the  $z$ -axis at a distance  $h$  from the interface between the two half-spaces  $\mathcal{D}_1$  and  $\mathcal{D}_2$ . The wave speeds in these two media are  $c_1$  and  $c_2$ , respectively.

## 5.2 Description of the configuration

The two-media configuration under consideration is made up of two half-spaces  $\mathcal{D}_1$  and  $\mathcal{D}_2$  (see Fig. 5.1). To locate position in the configuration, orthogonal Cartesian coordinates  $\{x, y, z\}$  with respect to a fixed reference frame are used. The reference frame is chosen such that the half-space  $\mathcal{D}_1$  coincides with  $\{z > 0\}$ , and the half-space  $\mathcal{D}_2$  with  $\{z < 0\}$ . The point source is located at  $\{0, 0, h\}$  with  $h > 0$ . The time coordinate is  $t$ . The wavespeeds in  $\mathcal{D}_1$  and  $\mathcal{D}_2$  are denoted by  $c_1$  and  $c_2$ , respectively. The scalar wave motion is described by the wave function  $u = u(x, y, z, t)$ . We write

$$u = u_0 + u_1 \quad \text{in } \mathcal{D}_1, \quad (5.1)$$

$$u = u_2 \quad \text{in } \mathcal{D}_2, \quad (5.2)$$

where  $u_0$  denotes the wave field incident on the interface  $\{z = 0\}$ ,  $u_1$  is the reflected wave field in  $\mathcal{D}_1$ , and  $u_2$  is the transmitted wave field in  $\mathcal{D}_2$ . Let  $f = f(t)$  be the pulse shape (“signature”) of the exciting point source, then the wave functions satisfy the following wave equations (partial differentiation is denoted by the operator  $\partial$ ):

$$(\partial_x^2 + \partial_y^2 + \partial_z^2 - c_1^{-2}\partial_t^2) u_0 = -f(t)\delta(x, y, z - h) \quad \text{for } z > 0, \quad (5.3)$$

$$(\partial_x^2 + \partial_y^2 + \partial_z^2 - c_1^{-2}\partial_t^2) u_1 = 0 \quad \text{for } z > 0, \quad (5.4)$$

$$(\partial_x^2 + \partial_y^2 + \partial_z^2 - c_2^{-2}\partial_t^2) u_2 = 0 \quad \text{for } z < 0. \quad (5.5)$$

We assume that  $f(t) = 0$  for  $t < 0$ . Then the wave motion that is causally related to the action of the source satisfies the causality condition  $u(x, y, z, t) = 0$  for  $t < 0$  and all  $\{x, y, z\}$ . As the boundary conditions to be satisfied across the interface we take

$$\lim_{z \downarrow 0} [u_0(z) + u_1(z)] = \lim_{z \uparrow 0} [u_2(z)] \quad \text{for all } \{x, y\}, \quad (5.6)$$

$$\lim_{z \downarrow 0} [\partial_z u_0(z) + \partial_z u_1(z)] = \lim_{z \uparrow 0} [\partial_z u_2(z)] \quad \text{for all } \{x, y\}. \quad (5.7)$$

They are representative for the electric field components parallel to the interface in a configuration of dielectric media as well as for the acoustic pressure in a configuration of constant volume density of mass (which implies, because of a difference in wavespeeds, a difference in compressibility in the two media [DE HOOP, 1995]).

The incident wave field is the spherical wave

$$u_0(x, y, z, t) = \frac{f(t - R_0/c_1)}{4\pi R_0} \quad \text{for } R_0 > 0, \quad (5.8)$$

where  $R_0 = [x^2 + y^2 + (z - h)^2]^{1/2}$ .

Let

$$\hat{f}(s) = \int_0^{\infty} \exp(-st) f(t) dt \quad \text{for } \text{Re}(s) > 0 \quad (5.9)$$

be the one-sided causal Laplace transformation with respect to  $t$ . Then, the power density spectrum of the source signature is defined as

$$I_f(\omega) = 10 \log_{10} \left( \left| \hat{f}(i\omega) \right|^2 \right), \quad (5.10)$$

where  $\omega$  is the angular frequency, and  $i$  the imaginary unit. The diagram in which the quantity  $10 \log_{10} (|\hat{f}(i\omega)/\hat{f}(0)|^2)$  is plotted as a function of frequency  $\omega/2\pi$  is denoted as the *spectral diagram*. Eq. (5.8) leads to

$$\hat{u}_0(s) = \hat{f}(s) \frac{\exp(-sR_0/c_1)}{4\pi R_0} \quad \text{for } R_0 > 0. \quad (5.11)$$

Hence, the spectral diagram of the emitted wave coincides with the one of the source signature. As we will show, this property no longer holds for the reflected wave  $u_1$ .

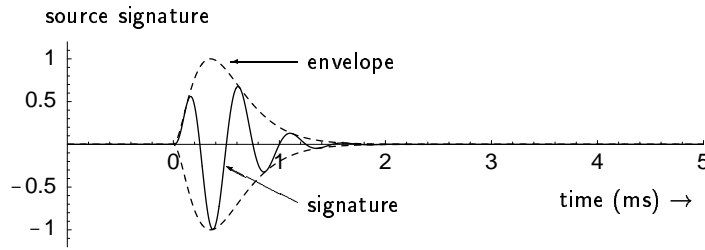


Figure 5.2: The source signature or pulse shape as given by Eq. (5.12) (solid line) and its envelope (dashed line). The source parameters are  $A = 1$ ,  $\alpha = 5.71 \times 10^3 \text{ s}^{-1}$ ,  $\nu = 2$ ,  $\omega_0/2\pi = 2 \text{ kHz}$ . The corresponding pulse rise time and time width are  $t_r = 0.35 \text{ ms}$ ,  $t_w = 0.65 \text{ ms}$ .

In our examples, we shall use the “power-exponential” modulated sinusoidal source signature [DE HOOP ET AL., 1995]

$$f(t) = \begin{cases} 0 & \text{for } t < 0, \\ A \left(\frac{\alpha t}{\nu}\right)^\nu \exp(-\alpha t + \nu) \sin(\omega_0 t) & \text{for } t \geq 0, \end{cases} \quad (5.12)$$

which is plotted in Fig. 5.2. Here  $A$  is the amplitude of the pulse,  $\omega_0 > 0$  the angular frequency of its sinusoidal carrier, while the parameters  $\alpha > 0$  and  $\nu > 0$  are related to the pulse rise time  $t_r$  and the pulse time width  $t_w$  of the modulating amplitude function (envelope) via

$$t_r = \nu/\alpha, \quad (5.13)$$

$$t_w = \alpha^{-1} \nu^{-\nu} \exp(\nu) \Gamma(\nu + 1), \quad (5.14)$$

in which  $\Gamma$  denotes the Euler gamma function. For this source signature, the corresponding spectral diagram

$$\hat{f}(s) = A \left(\frac{\alpha}{\nu}\right)^\nu \exp(\nu) \frac{\Gamma(\nu + 1)}{2i} \times \left[ \frac{1}{(s + \alpha - i\omega_0)^{\nu+1}} - \frac{1}{(s + \alpha + i\omega_0)^{\nu+1}} \right] \quad \text{for } \text{Re}(s) > 0. \quad (5.15)$$

is shown in Fig. 5.3.

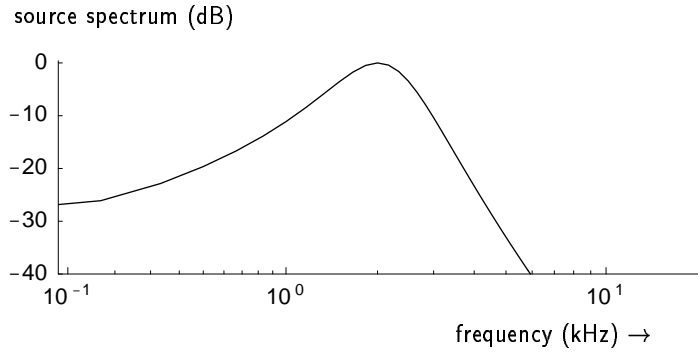


Figure 5.3: The spectral diagram (normalized to 0 dB) of the source signature of Fig. 5.2.

### 5.3 The modified Cagniard method

The reflection problem at hand will be solved with the aid of the modified Cagniard method. The first step in this method consists of subjecting the (causal) wave functions to a one-sided Laplace transformation with transform parameter  $s$ :

$$\hat{u}(x, y, z, s) = \int_0^{\infty} \exp(-st)u(x, y, z, t) dt. \quad (5.16)$$

We choose  $s \in \mathcal{R}$  and large enough to ensure the existence of the right-hand side. Under this transformation  $\partial_t = s$ . Furthermore, the by a factor of  $s$  scaled, spatial Fourier representation of  $\hat{u}(x, y, z, s)$  in the coordinates  $x$  and  $y$  parallel to the interface is given by

$$\hat{u}(x, y, z, s) = \left(\frac{s}{2\pi}\right)^2 \int_{-\infty}^{\infty} \int_{-\infty}^{\infty} \exp(-is\alpha x - is\beta y) \tilde{u}(\alpha, \beta, z, s) d\alpha d\beta. \quad (5.17)$$

In this representation,  $\alpha$  and  $\beta$  are the so-called slowness parameters. With this representation, we have  $\tilde{\partial}_x = -is\alpha$ ,  $\tilde{\partial}_y = -is\beta$ . As a result, the wavefunctions in the slowness domain satisfy the equations

$$\partial_z^2 \tilde{u}_0 - s^2 \gamma_1^2 \tilde{u}_0 = -\hat{f}(s) \delta(z - h) \quad \text{for } z > 0, \quad (5.18)$$

$$\partial_z^2 \tilde{u}_1 - s^2 \gamma_1^2 \tilde{u}_1 = 0 \quad \text{for } z > 0, \quad (5.19)$$

$$\partial_z^2 \tilde{u}_2 - s^2 \gamma_2^2 \tilde{u}_2 = 0 \quad \text{for } z < 0. \quad (5.20)$$

Here,

$$\gamma_{1,2} = \left( \frac{1}{c_{1,2}^2} + \alpha^2 + \beta^2 \right)^{1/2}, \quad (5.21)$$

with the square root chosen such that  $\gamma_{1,2} > 0$  for all real values of  $\alpha$  and  $\beta$ . The bounded solutions of these transformed wave equations are written as

$$\tilde{u}_0(\alpha, \beta, z, s) = \frac{\hat{f}(s)}{2s\gamma_1} \exp[-s\gamma_1|z-h|] \quad \text{for } z > 0, \quad (5.22)$$

$$\tilde{u}_1(\alpha, \beta, z, s) = \mathcal{R}(\alpha, \beta) \frac{\hat{f}(s)}{2s\gamma_1} \exp[-s\gamma_1(z+h)] \quad \text{for } z > 0, \quad (5.23)$$

$$\tilde{u}_2(\alpha, \beta, z, s) = \mathcal{T}(\alpha, \beta) \frac{\hat{f}(s)}{2s\gamma_1} \exp[-s(\gamma_1 h - \gamma_2 z)] \quad \text{for } z < 0, \quad (5.24)$$

where  $\mathcal{R}(\alpha, \beta)$  and  $\mathcal{T}(\alpha, \beta)$  are the interface reflection and transmission coefficients, respectively. From the application of the boundary conditions (Eqs. (5.6) and (5.7)) we obtain

$$\mathcal{R}(\alpha, \beta) = \frac{\gamma_1 - \gamma_2}{\gamma_1 + \gamma_2}, \quad (5.25)$$

$$\mathcal{T}(\alpha, \beta) = \frac{2\gamma_1}{\gamma_1 + \gamma_2}. \quad (5.26)$$

Note, in particular, that  $\mathcal{R}$  and  $\mathcal{T}$  remain bounded for all real values of the slowness parameters  $\alpha$  and  $\beta$ , since, for the chosen value of  $\gamma_{1,2}$  their denominator never vanishes. Substitution of Eqs. (5.22)–(5.24) into Eq. (5.17) leads to representations of  $\hat{u}_0$ ,  $\hat{u}_1$ , and  $\hat{u}_2$ , respectively.

The idea which is central to the modified Cagniard method is to transform the Fourier representations of the reflected and transmitted wavefields (Eqs. (5.23) and (5.24)) into expressions of a particular shape such that the

transformation from  $\hat{u}(x, y, z, s)$  to  $u(x, y, z, t)$  can be carried out by inspection. (Note that since  $s$  in Eq. (5.16) has been chosen to be real and positive, we cannot rely on Fourier's integral theorem for this purpose.) Taking into account the algebraic factors of  $s$  and  $f(s)$  in the expressions (5.17) and (5.22)–(5.24), we aim at representations of the type

$$\hat{u}(x, y, z, s) = s \hat{f}(s) \hat{g}(x, y, z, s), \quad (5.27)$$

in which the system's Green's function  $\hat{g}$  can be cast into the form

$$\hat{g}(x, y, z, s) = \int_{T_{\text{arr}}}^{\infty} \exp(-s\tau) g(x, y, z, \tau) d\tau, \quad (5.28)$$

where  $\tau$  is a real variable of integration. In view of Lerch's theorem on the uniqueness of the one-sided Laplace transformation [WIDDER, 1946], the time-domain equivalent of (5.27) then follows as

$$u(x, y, z, t) = \begin{cases} 0 & \text{for } -\infty < t < T_{\text{arr}}, \\ \partial_t \int_{T_{\text{arr}}}^t f(t - \tau) g(x, y, z, \tau) d\tau & \text{for } T_{\text{arr}} < t < \infty. \end{cases} \quad (5.29)$$

Evidently,  $T_{\text{arr}}$  can be identified as the arrival time of the relevant wave motion.

A comparison of Eq. (5.28) with Eqs. (5.17) and (5.22)–(5.24) learns that  $\tau$  is related to  $\alpha$  and  $\beta$  via

$$i(\alpha x + \beta y) + \gamma_1(z + h) = \tau \quad (5.30)$$

for the reflected wave, and

$$i(\alpha x + \beta y) + \gamma_1 h - \gamma_2 z = \tau \quad (5.31)$$

for the transmitted wave. As a consequence, to reach our goal we have to deviate from the real values of  $\alpha$  and  $\beta$  occurring in Eq. (5.17), which means that analytic continuations into complex values are needed. For this, we proceed as follows. First, in Eq. (5.17),  $\{\alpha, \beta\}$  are replaced by  $\{\zeta, q\}$  via

$$\begin{aligned} \alpha &= \zeta \cos(\theta) - q \sin(\theta), \\ \beta &= \zeta \sin(\theta) + q \cos(\theta), \end{aligned} \quad (5.32)$$

where  $x = r \cos(\theta)$  and  $y = r \sin(\theta)$  with  $0 \leq r < \infty$ ,  $0 \leq \theta < 2\pi$ . Under this transformation  $\alpha^2 + \beta^2 = \zeta^2 + q^2$  and  $d\alpha d\beta = d\zeta dq$ , while

$$\alpha x + \beta y = \zeta r. \quad (5.33)$$

Subject to Eq. (5.32), Eq. (5.17) transforms into

$$\hat{u}(x, y, z, s) = \left(\frac{s}{2\pi}\right)^2 \int_{-\infty}^{\infty} dq \int_{-\infty}^{\infty} \exp(-i\zeta sr) \tilde{u}(\zeta, q, z, s) d\zeta. \quad (5.34)$$

Next, in the inner integral,  $p = i\zeta$  is introduced as the variable of integration. This leads to

$$\hat{u}(x, y, z, s) = \frac{s^2}{4\pi^2 i} \int_{-\infty}^{\infty} dq \int_{-\infty}^{i\infty} \exp(-psr) \tilde{u}(\zeta, q, z, s) dp. \quad (5.35)$$

Furthermore, Eq. (5.21) transforms into

$$\gamma_{1,2}(p, q) = (\Omega_{1,2}^2(q) - p^2)^{1/2} \quad (5.36)$$

with

$$\Omega_{1,2}(q) = \left(\frac{1}{c_{1,2}^2} + q^2\right)^{1/2} > 0. \quad (5.37)$$

Finally, the integrand in the integral with respect to  $p$  is continued analytically into the complex  $p$ -plane, away from the imaginary axis. In this procedure, we keep  $\text{Re}(\gamma_{1,2}) \geq 0$ , which implies that branch cuts are introduced along  $\{\text{Im}(p) = 0, \Omega_{1,2} \leq |\text{Re}(p)| < \infty\}$ . To arrive at expressions of the type needed in (5.28), we now can deform the path of integration in the complex  $p$ -plane, under the application of Cauchy's theorem (which necessitates avoiding crossing the branch cuts).

In our further analysis, we will concentrate on obtaining the spectral diagram of the reflected wave in its dependence on the position of observation and on the on-axis spectral diagrams of the reflected waves as a special case.

## 5.4 The reflected wave in $\mathcal{D}_1$

On using Eqs. (5.23), (5.32) and (5.35) we obtain

$$\hat{u}_1(x, y, z, s) = \frac{s \hat{f}(s)}{4\pi^2 i} \int_{-\infty}^{\infty} dq \int_{-i\infty}^{i\infty} \exp[-s(pr + \gamma_1 H_1)] \frac{\mathcal{R}(p, q)}{2\gamma_1(p, q)} dp, \quad (5.38)$$

where  $H_1 \equiv z + h$ , ( $H_1 > 0$ ) is the vertically traversed distance. The inner integration is along the imaginary axis of the complex  $p$ -plane. In accordance with Eqs. (5.30) and (5.33) we deform this path of integration into the modified Cagniard path

$$pr + \gamma_1 H_1 = \tau, \quad (5.39)$$

with  $\tau$  real and positive. For a fixed value of  $\tau$ , we have either two complex conjugate solutions for  $p$  or two real-valued ones. The first two are given by

$$p = \begin{cases} p_1^{\text{BW}}(r, H_1, q, \tau), \\ p_1^{\text{BW}*}(r, H_1, q, \tau), \end{cases} \quad (5.40)$$

where

$$p_1^{\text{BW}} = \frac{r}{r^2 + H_1^2} \tau + i \frac{H_1}{r^2 + H_1^2} [\tau^2 - T_1^2(q)]^{1/2} \quad \text{for } T_1(q) < \tau < \infty, \quad (5.41)$$

with

$$T_1(q) = (r^2 + H_1^2)^{1/2} \Omega_1(q). \quad (5.42)$$

Here, the superscript BW is indicative for body-waves. This part, the body-wave part, goes to infinity as  $\tau \rightarrow \infty$  and has the asymptotic form

$$p_1^{\text{BW}} \sim \left[ \frac{r + iH_1}{r^2 + H_1^2} \right] \tau \quad \text{as } \tau \rightarrow \infty. \quad (5.43)$$

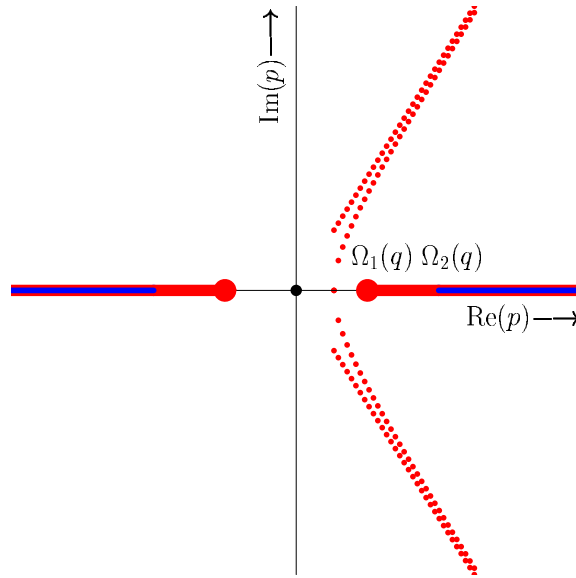


Figure 5.4: The modified Cagniard path in the complex slowness plane for  $c_1 > c_2$ . Only a body-wave contribution is present. Both the body-wave part and the asymptote are shown. The dots indicate equidistant time intervals.

From Eq. (5.43) it follows that these solutions can be used to join the original path of integration (the imaginary axis) via supplementing circular arcs at infinity. In view of Jordan's lemma, the latter yield a vanishing contribution. The point of intersection of the modified Cagniard path  $\{p = p_1^{\text{BW}}\} \cup \{p = p_1^{\text{BW}*}\}$  and the real  $p$ -axis occurs at  $\tau = T_1(q)$  and is located at

$$p = \frac{rT_1(q)}{r^2 + H_1^2}. \quad (5.44)$$

In the case  $c_1 > c_2$  (where from Eq. (5.37)  $\Omega_1(q) < \Omega_2(q)$  for all  $q$ ) this point lies to the left of the most left branch point  $p = \Omega_1(q)$ . Since, furthermore, the integrand is free from singularities in between the imaginary axis and the modified Cagniard path, the integral along the imaginary axis in Eq. (5.38) can be replaced by the one along  $\{p = p_1^{\text{BW}}\} \cup \{p = p_1^{\text{BW}*}\}$  (see Fig. 5.4).

In the case  $c_1 < c_2$ ,  $\Omega_1(q) > \Omega_2(q)$  for all  $q$ , and deviations from this simple situation may occur. In this respect the part of the real axis  $\{\text{Im}(p) =$

$0, -\Omega_2(q) < \text{Re}(p) < \Omega_2(q)$  comes into play as a second candidate for the modified Cagniard path. Details for this case will be discussed below.

**The case  $c_1 > c_2$**

As was explained above, in this case the point where the  $p_1^{\text{BW}}$  contour intersects the real axis lies in between 0 and the branch point  $\Omega_1(q)$  as defined in Eq. (5.37). Therefore, in this case, only a body-wave contribution exists. Introducing  $\tau$  as the variable of integration along the modified Cagniard path  $\{p = p_1^{\text{BW}}\} \cup \{p = p_1^{\text{BW}*}\}$  in Eq. (5.38) leads to

$$\hat{u}_1(x, y, z, s) = \frac{s \hat{f}(s)}{\pi^2} \int_0^\infty dq \int_{T_1(q)}^\infty \exp(-s\tau) \text{Im} \left[ \frac{\mathcal{R}(p_1^{\text{BW}}, q)}{2\gamma_1(p_1^{\text{BW}}, q)} \frac{\partial p_1^{\text{BW}}}{\partial \tau} \right] d\tau, \quad (5.45)$$

where we have used the fact that the integrand is an even function of  $q$  and that the integrand in  $p$  satisfies Schwarz's reflection principle of complex function theory. Interchanging the order of the integrations in Eq. (5.45) leads to

$$\hat{u}_1(x, y, z, s) = \frac{s \hat{f}(s)}{\pi^2} \int_{T_1(0)}^\infty d\tau \exp(-s\tau) \int_0^{A(\tau)} \text{Im} \left[ \frac{\mathcal{R}(p_1^{\text{BW}}, q)}{2\gamma_1(p_1^{\text{BW}}, q)} \frac{\partial p_1^{\text{BW}}}{\partial \tau} \right] dq, \quad (5.46)$$

in which  $A(\tau)$  follows, upon using Eqs. (5.42) and (5.37) and  $T_1(0) = (r^2 + H_1^2)^{1/2}/c_1$  as

$$A(\tau) = \left( \frac{\tau^2}{r^2 + H_1^2} - \frac{1}{c_1^2} \right)^{1/2}. \quad (5.47)$$

With this, we have arrived at the desired form as expressed by Eqs. (5.27) and (5.28) and the response function  $g(x, y, z, \tau)$  follows from Eq. (5.46) by inspection as

$$g_1(x, y, z, \tau) = \begin{cases} 0 & -\infty < \tau < T_1(0), \\ \frac{1}{\pi^2} \int_0^{A(\tau)} \text{Im} \left[ \frac{\mathcal{R}(p_1^{\text{BW}}, q)}{2\gamma_1(p_1^{\text{BW}}, q)} \frac{\partial p_1^{\text{BW}}}{\partial \tau} \right] dq & T_1(0) < \tau < \infty. \end{cases} \quad (5.48)$$

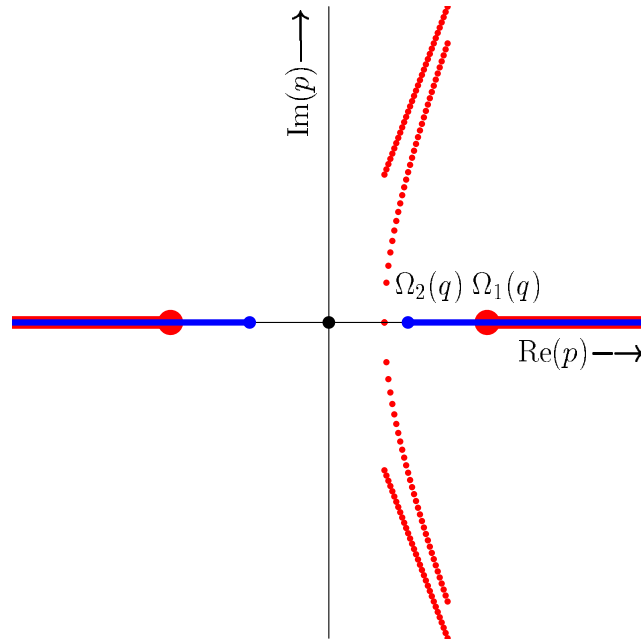


Figure 5.5: The modified Cagniard path in the complex slowness plane for the case  $c_2 > c_1$ , and no head-wave contribution. Both the body-wave part and the asymptote are shown. The dots indicate equidistant time intervals.

Substitution of this Green's function in Eq. (5.29) completes the solution of the reflected field for this case. Evidently,  $T_1(0)$  can be interpreted as the arrival time of the wave upon travelling from the image of the point source in the interface to the point of observation in  $\mathcal{D}_1$ .

### The case $c_1 < c_2$

Now, two situations can arise, depending on the point of observation.

(a) The body-wave modified Cagniard path crosses the real  $p$ -axis to the left of  $\Omega_2(q)$ . (Note that, since  $c_2 > c_1$ ,  $\Omega_2(q) < \Omega_1(q)$ , see Fig. 5.5). For this case the analysis is identical with the one for the previous case.

(b) The modified body-wave path ends on the real  $p$ -axis on the branch cut associated with  $\Omega_2(q)$ . Inspection of Eq. (5.44) learns that this happens in the region of space

$$\Theta > \Theta_{\text{crit}} = \arcsin(c_1/c_2), \quad (5.49)$$

where we defined

$$\sin(\Theta) = \frac{r}{(r^2 + H_1^2)^{1/2}}, \quad (5.50)$$

with  $0 \leq \Theta < \pi/2$ , and for the finite range in  $q$  given by

$$0 < q < \frac{1}{\cos(\Theta)} \left( \frac{1}{c_1^2} \sin^2(\Theta) - \frac{1}{c_2^2} \right)^{1/2} = B. \quad (5.51)$$

(We note that (5.49) is the condition for total internal reflection which accompanies the occurrence of head-waves.) Let  $T_1^{\text{HW}}(q)$  be the value of  $\tau$  corresponding to the branch point  $p = \Omega_2(q)$ , then

$$T_1^{\text{HW}}(q) = \Omega_2(q)r + \left( \frac{1}{c_1^2} - \frac{1}{c_2^2} \right)^{1/2} H_1, \quad (5.52)$$

where we used Eqs. (5.39) and (5.36). Now, the deformation of the original path of integration (the imaginary axis) into the modified Cagniard path under the application of Cauchy's theorem requires the body-wave part to be supplemented by a loop around the branch cut associated with  $\Omega_2(q)$ , and joining the points where the body-wave parts approach the real  $p$ -axis (see Fig. 5.6). The parametrization of this part in accordance with Eq. (5.39) leads to

$$p_1^{\text{HW}}(r, H_1, \tau) = \lim_{\delta \downarrow 0} \left[ \frac{r}{r^2 + H_1^2} \tau - \frac{H_1}{r^2 + H_1^2} [T_1^2(q) - \tau^2]^{1/2} + i\delta \right] \\ \text{for } H_1 \Omega_1(q) < \tau \leq T_1(q). \quad (5.53)$$

The superscript HW denotes head-waves [MAECKER, 1949]. (An interesting historical account of head-waves and their application in seismology is given by Mintrop [1930].) The additional loop is given by  $\{p = p_1^{\text{HW}}\} \cup \{p = p_1^{\text{HW}*}\}$ . Introducing  $\tau$  as the variable of integration in Eq. (5.38) gives

$$\hat{u}_1(x, y, z, s) = \frac{s \hat{f}(s)}{\pi^2} \int_0^B dq \int_{T_1^{\text{HW}}(q)}^{T_1(q)} \exp(-s\tau) \text{Im} \left[ \frac{\mathcal{R}(p_1^{\text{HW}}, q)}{2\gamma_1(p_1^{\text{HW}}, q)} \frac{\partial p_1^{\text{HW}}}{\partial \tau} \right] d\tau \\ + \frac{s \hat{f}(s)}{\pi^2} \int_0^\infty dq \int_{T_1(q)}^\infty \exp(-s\tau) \text{Im} \left[ \frac{\mathcal{R}(p_1^{\text{BW}}, q)}{2\gamma_1(p_1^{\text{BW}}, q)} \frac{\partial p_1^{\text{BW}}}{\partial \tau} \right] d\tau, \quad (5.54)$$



For the body-wave contribution of Eq. (5.54) we get the result obtained earlier in Eq. (5.46). So, finally,

$$g_1(x, y, z, \tau) = 0, \quad (5.58)$$

for  $-\infty < \tau < T_1^{\text{HW}}(0)$ ;

$$g_1(x, y, z, \tau) = \frac{1}{\pi^2} \int_0^{C(\tau)} \text{Im} \left[ \frac{\mathcal{R}(p_1^{\text{HW}}, q)}{2\gamma_1(p_1^{\text{HW}}, q)} \frac{\partial p_1^{\text{HW}}}{\partial \tau} \right] dq \quad (5.59)$$

for  $T_1^{\text{HW}}(0) < \tau < T_1(0)$ ;

$$\begin{aligned} g_1(x, y, z, \tau) = & \frac{1}{\pi^2} \int_{A(\tau)}^{C(\tau)} \text{Im} \left[ \frac{\mathcal{R}(p_1^{\text{HW}}, q)}{2\gamma_1(p_1^{\text{HW}}, q)} \frac{\partial p_1^{\text{HW}}}{\partial \tau} \right] dq \\ & + \frac{1}{\pi^2} \int_0^{A(\tau)} \text{Im} \left[ \frac{\mathcal{R}(p_1^{\text{BW}}, q)}{2\gamma_1(p_1^{\text{BW}}, q)} \frac{\partial p_1^{\text{BW}}}{\partial \tau} \right] dq \end{aligned} \quad (5.60)$$

for  $T_1(0) < \tau < D$ , and

$$g_1(x, y, z, \tau) = \frac{1}{\pi^2} \int_0^{A(\tau)} \text{Im} \left[ \frac{\mathcal{R}(p_1^{\text{BW}}, q)}{2\gamma_1(p_1^{\text{BW}}, q)} \frac{\partial p_1^{\text{BW}}}{\partial \tau} \right] dq \quad (5.61)$$

for  $D < \tau < \infty$ .

This concludes the calculation of the Green's function for this case. We observe that, according to Eq. (5.61), in the representation of  $g_1(x, y, z, \tau)$  three breakpoints in time occur. The first,  $\tau = T_1^{\text{HW}}(0)$ , marks the arrival time of the head-waves. The second,  $\tau = T_1(0)$ , marks the arrival of the body-wave. The third,  $\tau = D$ , is induced by the derivation and has no straightforward physical interpretation. Note that in the interval  $T_1(0) < \tau < D$  a head-wave contribution still persists, and that in the interval  $D < \tau < \infty$  only a body-wave contribution occurs.

## 5.5 The on-axis response

For the special case that the point of observation lies on the  $z$ -axis, i.e., on the line through the point source perpendicular to the interface, the analysis of the reflected field simplifies considerably and an analytic expression of the Green's function can be obtained. To see this, we substitute  $x = y = 0$  into Eq. (5.17) and use Eq. (5.23). This leads to

$$\hat{u}_1(0, 0, z, s) = \frac{s \hat{f}(s)}{8\pi^2} \int_{-\infty}^{\infty} \int_{-\infty}^{\infty} \exp[-s\gamma_1(z+h)] \frac{\mathcal{R}(\alpha, \beta)}{\gamma_1(\alpha, \beta)} d\alpha d\beta. \quad (5.62)$$

We note that in the integrand on the right-hand side the variables  $\alpha$  and  $\beta$  appear in the form  $\alpha^2 + \beta^2$  only. Therefore, it is now advantageous to introduce the polar variables of integration  $\kappa$  and  $\psi$  via

$$\alpha = \kappa \cos(\psi), \quad (5.63)$$

$$\beta = \kappa \sin(\psi), \quad (5.64)$$

with  $0 \leq \kappa < \infty$  and  $0 \leq \psi < 2\pi$ . This yields  $d\alpha d\beta = \kappa d\kappa d\psi$ , and

$$\gamma_{1,2}(\kappa) = (c_{1,2}^{-2} + \kappa^2)^{1/2}, \quad (5.65)$$

$$\mathcal{R}(\kappa) = \frac{\gamma_1(\kappa) - \gamma_2(\kappa)}{\gamma_1(\kappa) + \gamma_2(\kappa)}, \quad (5.66)$$

where we have used Eqs. (5.21) and (5.25). With this, Eq. (5.62) reduces to

$$\hat{u}_1(0, 0, z, s) = \frac{s \hat{f}(s)}{4\pi} \int_0^{\infty} \exp[-s\gamma_1(z+h)] \frac{\mathcal{R}(\kappa)}{\gamma_1(\kappa)} \kappa d\kappa. \quad (5.67)$$

In order to arrive at the desired form as expressed by Eqs. (5.27) and (5.28) we carry out the transformation

$$\gamma_1(\kappa)(z+h) = \tau, \quad (5.68)$$

with  $\tau$  real and positive. This leads to

$$\kappa^2 = \frac{\tau^2}{(z+h)^2} - \frac{1}{c_1^2}. \quad (5.69)$$

Rewriting all functions in Eq. (5.67) in terms of their dependence on  $\tau$  yields

$$\hat{u}_1(0, 0, z, s) = \frac{s\hat{f}(s)}{4\pi} \int_{T_{\text{arr}}}^{\infty} \exp(-s\tau) \frac{\mathcal{R}(\tau)}{z+h} d\tau, \quad (5.70)$$

where  $T_{\text{arr}} = (z+h)/c_1$ . Evidently,  $T_{\text{arr}}$  is the arrival time of the reflected wave at the point  $\{0, 0, z\}$ . In view of Eqs. (5.27)–(5.29) we find that the on-axis Green's function for the reflected field is now given by

$$g_1(0, 0, z, t) = \begin{cases} 0 & \text{for } -\infty < t < T_{\text{arr}}, \\ \frac{1}{4\pi} \frac{\mathcal{R}(\tau)}{z+h} & \text{for } T_{\text{arr}} < t < \infty. \end{cases} \quad (5.71)$$

This result for the on-axis Green's function for the reflected field may be compared with the one that results upon substituting  $r = 0$  into Eq. (5.34), i.e.

$$\hat{u}_1(0, 0, z, s) = \frac{s\hat{f}(s)}{8\pi^2} \int_{-\infty}^{\infty} dq \int_{-\infty}^{\infty} \frac{\mathcal{R}[(\zeta^2 + q^2)^{1/2}]}{\gamma_1} \exp[-s\gamma_1(z+h)] d\zeta, \quad (5.72)$$

where we have expressed that  $\mathcal{R}$  is a function of  $(\zeta^2 + q^2)^{1/2}$  only. To arrive at the form for the application of Lerch's theorem, we replace in the inner integral on the right-hand side the variable  $\zeta$  by  $\tau$  via

$$\gamma_1(z+h) = \tau. \quad (5.73)$$

This leads to

$$\zeta = \left[ \frac{\tau^2}{(z+h)^2} - q^2 - \frac{1}{c_1^2} \right]^{1/2}, \quad (5.74)$$

with the Jacobian

$$\frac{\partial \zeta}{\partial \tau} = \frac{\tau}{(z+h)^2 \zeta}. \quad (5.75)$$

Under this transformation, Eq. (5.72) takes the form

$$\begin{aligned} \hat{u}_1(0, 0, z, s) &= \frac{s \hat{f}(s)}{2\pi^2} \int_0^\infty dq \int_{T_0(q)}^\infty \exp(-s\tau) \\ &\quad \times \frac{\mathcal{R}(\tau)}{z+h} \left[ \frac{\tau^2}{(z+h)^2} - q^2 - \frac{1}{c_1^2} \right]^{-1/2} d\tau, \end{aligned} \quad (5.76)$$

with

$$T_0(q) = (z+h) \left[ q^2 + \frac{1}{c_1^2} \right]^{1/2}. \quad (5.77)$$

Interchanging the order of integration, we obtain

$$\begin{aligned} \hat{u}_1(0, 0, z, s) &= \frac{s \hat{f}(s)}{2\pi^2(z+h)} \int_{T_{\text{arr}}}^\infty \exp(-s\tau) \mathcal{R}(\tau) d\tau \\ &\quad \times \int_0^{Q_0(\tau)} \{ [Q_0(\tau)]^2 - q^2 \}^{-1/2} dq, \end{aligned} \quad (5.78)$$

with

$$Q_0(\tau) = \left[ \frac{\tau^2}{(z+h)^2} - \frac{1}{c_1^2} \right]^{1/2}. \quad (5.79)$$

Through the substitution

$$q = Q_0(\tau) \sin(\psi) \quad (5.80)$$

it is found that

$$\int_0^{Q_0(\tau)} \{ [Q_0(\tau)]^2 - q^2 \}^{-1/2} dq = \int_0^{\pi/2} d\psi = \pi/2. \quad (5.81)$$

Hence

$$\hat{u}_1(0, 0, z, s) = \frac{s \hat{f}(s)}{4\pi(z+h)} \int_{T_{\text{arr}}}^\infty \exp(-s\tau) \mathcal{R}(\tau) d\tau, \quad (5.82)$$

which is the same expression as in Eq. (5.70), but obtained in a different manner. The Green's function time-domain result is again given by Eq. (5.71). The Green's functions that were derived in this Chapter will be applied in Chapter 6 to calculate the power spectrum of the reflected field.

## **Chapter 6**

# **Reflection-induced spectral changes of the pulsed radiation emitted by a point source. Part II: Application**

S.H. Wiersma, T.D. Visser and A.T. de Hoop, submitted for publication

We calculate the field emitted by a pulsed point source above a planar interface. It is found that the observed power spectrum can differ significantly from the emitted spectrum. Also, the observed power spectrum depends strongly on the wavespeeds in the two media and on the position of the observation point with respect to the interface. The necessary formalism was developed in Chapter 5. In this Chapter numerical results are presented.

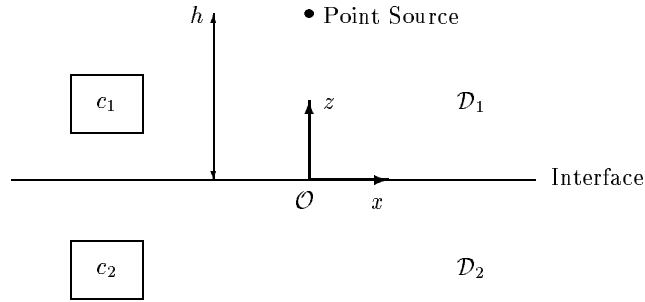


Figure 6.1: A point source above a planar interface. The source is located on the  $z$ -axis at a distance  $h$  from the interface between the two half-spaces  $\mathcal{D}_1$  and  $\mathcal{D}_2$ . The wave speeds in these two media are  $c_1$  and  $c_2$ , respectively.

## 6.1 Introduction

In Chapter 5 of this thesis we derived expressions for the reflected scalar wave field emitted by a pulsed point source located above a half-space. The two half-spaces are characterized by different wavespeeds. The configuration is depicted in Fig. 6.1. With the help of the modified Cagniard technique, Green's functions for the reflected field were obtained. In this Chapter, these Green's functions are applied to calculate the power density spectrum of the reflected wave field. It is found that this spectrum can differ substantially from that of the source excitation.

In our numerical examples, the parameters are taken from acoustics. In addition, pulse time widths are chosen such that within the spectral regime dispersion can be neglected.

The numerical integrations and the time convolutions resulting from the modified Cagniard method were carried out with the help of routines D01AJF and C06FKF of the NAG software library [NAG, 1998].

## 6.2 Numerical results

The numerical integrations and the time convolutions resulting from the modified Cagniard method were carried out with the help of the routines D01AJF and C06FKF of the NAG software library [NAG, 1998]. First we consider the case  $c_1 > c_2$ , which implies that there are no head-waves. An

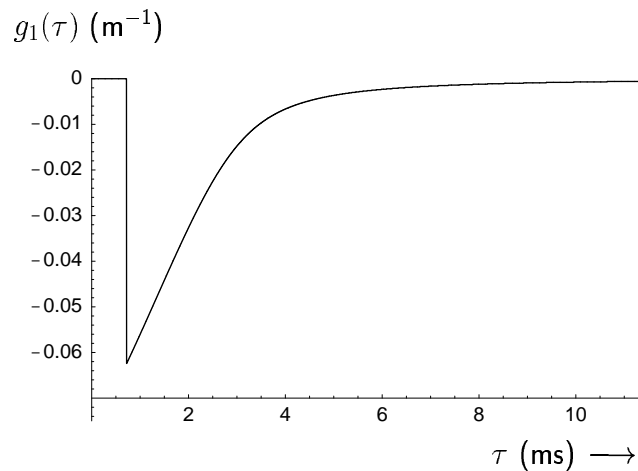


Figure 6.2: The Green's function  $g_1(\tau)$  as given by Eq. (5.48) for the case  $c_1 = 1500$  m/s,  $c_2 = 330$  m/s, and the source located at  $r = 0$  m,  $z = 0.3$  m. The observation point is at  $r = 1.0$  m,  $z = 0.1$  m. The body-wave arrival time is at  $\tau = 0.72$  ms.

example of the Green's function  $g_1(\tau)$  as given by Eq. (5.48) is shown in Fig. 6.2. At the body-wave arrival time  $\tau = T_1(0)$  it has a jump discontinuity and then tends to zero. We note that the function is negative (positive) when  $c_1 > c_2$  ( $c_1 < c_2$ ), in agreement with the behavior of the reflection coefficient (Eq. (5.25)). An example of the total field (i.e. the direct plus the reflected field)  $u(\tau)$  is given in Fig. 6.3.

In the previous two examples,  $c_1 > c_2$ . Upon interchanging the two wavespeeds, head-waves may occur. In that case the Green's function  $g_1(\tau)$  is given by Eq. (5.61). An example is depicted in Fig. 6.4. At the head-wave arrival time  $\tau = T_1^{\text{HW}}(0)$  the function is continuous and increases to a sharp maximum at the body-wave arrival time  $\tau = T_1(0)$ . The total field  $u(\tau)$  for the case when head-waves are present is depicted in Fig. 6.5. The contribution of the head-wave is clearly visible before the arrival of the direct wave. When the point of observation is moved further away from the point source the separation between the head-wave and the body-wave contributions becomes even more distinct. The case in point is illustrated in Fig. 6.6.

An example of the extent of the direct and reflected wavefronts in the half-space  $\mathcal{D}_1$  as calculated with Eqs. (5.29) and (5.61) is shown in Fig. 6.7.

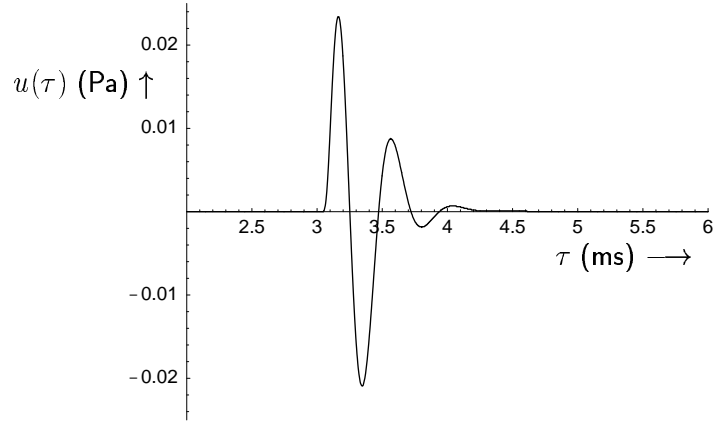


Figure 6.3: The total field  $u(\tau)$  for the case  $c_1 = 500$  m/s,  $c_2 = 330$  m/s. The source is at  $r = 0$  m,  $z = 0.3$  m. The observation point is at  $r = 1.5$  m,  $z = 0.05$  m. In this case the direct wave arrival time  $T_0^{\text{DIR}} = 3.04$  ms and the body-wave arrival time  $T_1(0) = 3.08$  ms. The source parameters are  $\omega_0 = 2\pi \times 10^3$  rad s $^{-1}$ ,  $\nu = 2$ , and  $\alpha = 8.71 \times 10^3$  s $^{-1}$ ,  $t_r = 0.23$  ms, and  $t_w = 0.42$  ms.

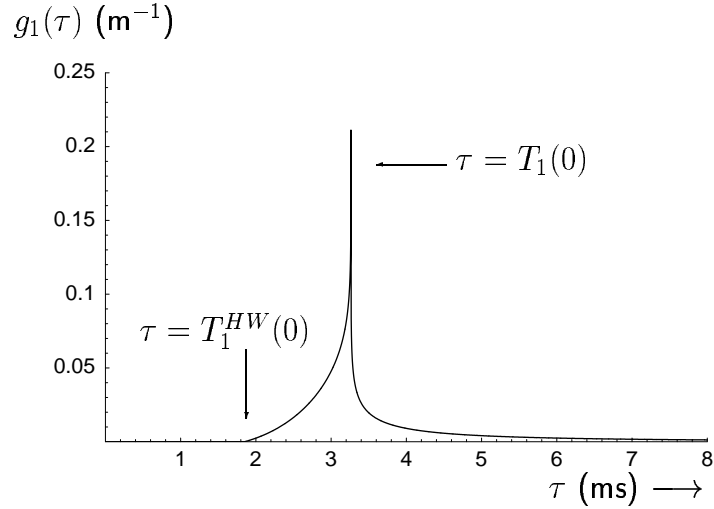


Figure 6.4: The Green's function  $g_1(\tau)$  as given by Eq. (5.61) for the case  $c_1 = 330$  m/s,  $c_2 = 1500$  m/s. The source is at  $r = 0$  m,  $z = 0.3$  m. The observation point is at  $r = 1$  m,  $z = 0.1$  m. In this case the head-wave arrival time  $T_1^{\text{HW}}(0) = 1.8$  ms and the body-wave arrival time  $T_1(0) = 3.3$  ms.

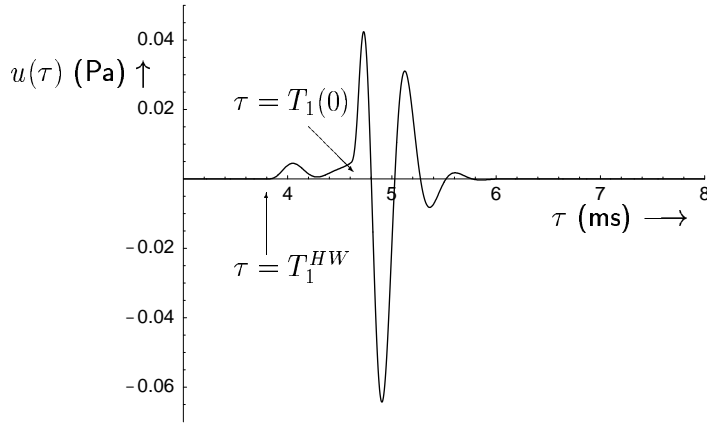


Figure 6.5: The total field  $u(\tau)$  for the case  $c_1 = 330$  m/s,  $c_2 = 500$  m/s. The source is at  $r = 0$  m,  $z = 0.3$  m. The observation point is at  $r = 1.5$  m,  $z = 0.05$  m. In this case the head-wave arrival time  $T_1^{HW} = 3.8$  ms, the direct wave arrival time  $T_0^{DIR} = 4.6$  ms and the body-wave arrival time  $T_1(0) = 4.7$  ms. The source parameters are as in Fig. 6.3.

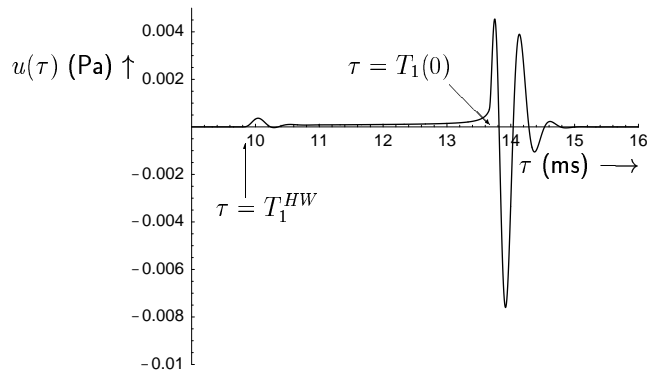


Figure 6.6: The total field  $u(\tau)$  for the case  $c_1 = 330$  m/s,  $c_2 = 500$  m/s. The source is at  $r = 0$  m,  $z = 0.3$  m. The observation point is at  $r = 4.5$  m,  $z = 0.05$  m. Notice that the head-wave contribution is separated from the body-wave contribution. In this case the head-wave arrival time  $T_1^{HW} = 9.79$  ms, the direct wave arrival time  $T_0^{DIR} = 13.66$  ms and the body-wave arrival time  $T_1(0) = 13.68$  ms. The source parameters are as in Fig. 6.3.

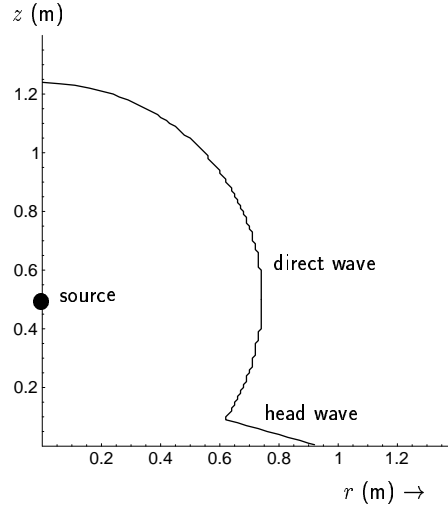


Figure 6.7: The position of the wavefront at  $t = 2.238$  ms for the case  $c_1 = 330$  m/s,  $c_2 = 1200$  m/s. The source is located at  $r = 0$  m,  $z = 0.5$  m.

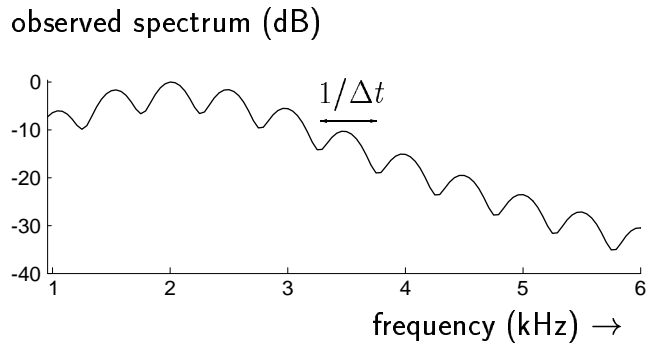


Figure 6.8: Part of the observed normalized power spectrum for on-axis observation. The source is located at  $r = 0$  m,  $z = 0.25$  m, and the observation point is at  $r = 0$  m,  $z = 1.25$  m. The wave speeds are  $c_1 = 250$  m/s,  $c_2 = 800$  m/s. The resulting time delay between the arrivals of the direct wave and the reflected wave is  $\Delta t = 2$  ms. As mentioned in Section 6.2, the spacing between the minima should be  $1/\Delta t = 0.5$  kHz, as is indeed the case. The source parameters are  $\omega_0 = 4\pi \times 10^3$  rad s $^{-1}$ ,  $\nu = 2$ ,  $\alpha = 8.71 \times 10^3$  s $^{-1}$ ,  $t_r = 0.23$  ms, and  $t_w = 0.42$  ms.

It is noted that the direct wave has a spherical wavefront, whereas the head-wave has a conical wavefront. It was verified that the sine of the angle between the head wavefront and the interface indeed equals  $c_1/c_2$ .

As a further test we examined the observed power spectrum under on-axis propagation and reflection. The result, shown in Fig. 6.8, reproduces the well-known effect from spectral interferometry [WALSMLEY, 1999]: the minima are equally spaced and the spacing between them equals  $1/\Delta t$ , where  $\Delta t$  is the time delay between the arrival times of the direct field and the reflected field. The spacing was found to be in excellent agreement with this prediction.

How the observed signal can differ from the signal that is emitted by the source is illustrated by Fig. 6.9. The source signal and its normalized power spectrum are shown in (a, b). The observation point is kept fixed and  $c_2$ , the wavespeed in the medium against which reflection takes place, is varied. Changing  $c_2$  varies the values of the reflection coefficient  $\mathcal{R}$  and the arrival time of (possible) head-waves. Even when no head-waves are present (c, d), the observed normalized power spectrum differs significantly from the one of the source. Upon increasing  $c_2$ , the interplay between head-wave, body-wave and the direct wave alters the shape of the observed signal and its power spectrum even more (e). It is noted that the maximum of the power spectrum is no longer at the carrier frequency  $\omega_0/2\pi$  (f). In case (e, f) the head-wave arrives after the direct wave. Upon further increasing  $c_2$  the arrival time of the head-waves decreases, and is earlier than that of the direct wave (g, i). Also, the indentations in the observed power spectrum become much more pronounced (h, j).

---

Figure 6.9 [shown on page 96]: The source signal (a) and its normalized power spectrum (b). The observed signal and its corresponding power spectrum are shown for different wave-speeds in the second medium. In all cases  $c_1 = 330$  m/s, the arrival time of the direct wave is  $\tau = 3.05$  ms, and the arrival time of the reflected body-wave is  $\tau = 3.39$  ms. For  $c_2 = 200$  m/s, there are no head-waves (c, d); for  $c_2 = 400$  m/s, the head-waves arrive at  $\tau = 3.36$  ms (e, f); for  $c_2 = 800$  m/s, the head-waves arrive at  $\tau = 2.63$  ms (g, h); for  $c_2 = 1200$  m/s, the head-waves arrive at  $\tau = 2.29$  ms (i, j). The source parameters are  $\omega_0/2\pi = 2 \times 10^3$  rad s<sup>-1</sup>,  $\nu = 2$ ,  $\alpha = 8.71 \times 10^3$  s<sup>-1</sup>,  $t_r = 0.23$  ms, and  $t_w = 0.42$  ms. The source is located at  $r = 0$  m,  $z = 0.3$  m and the observation point is at  $r = 1.0$  m,  $z = 0.2$  m.

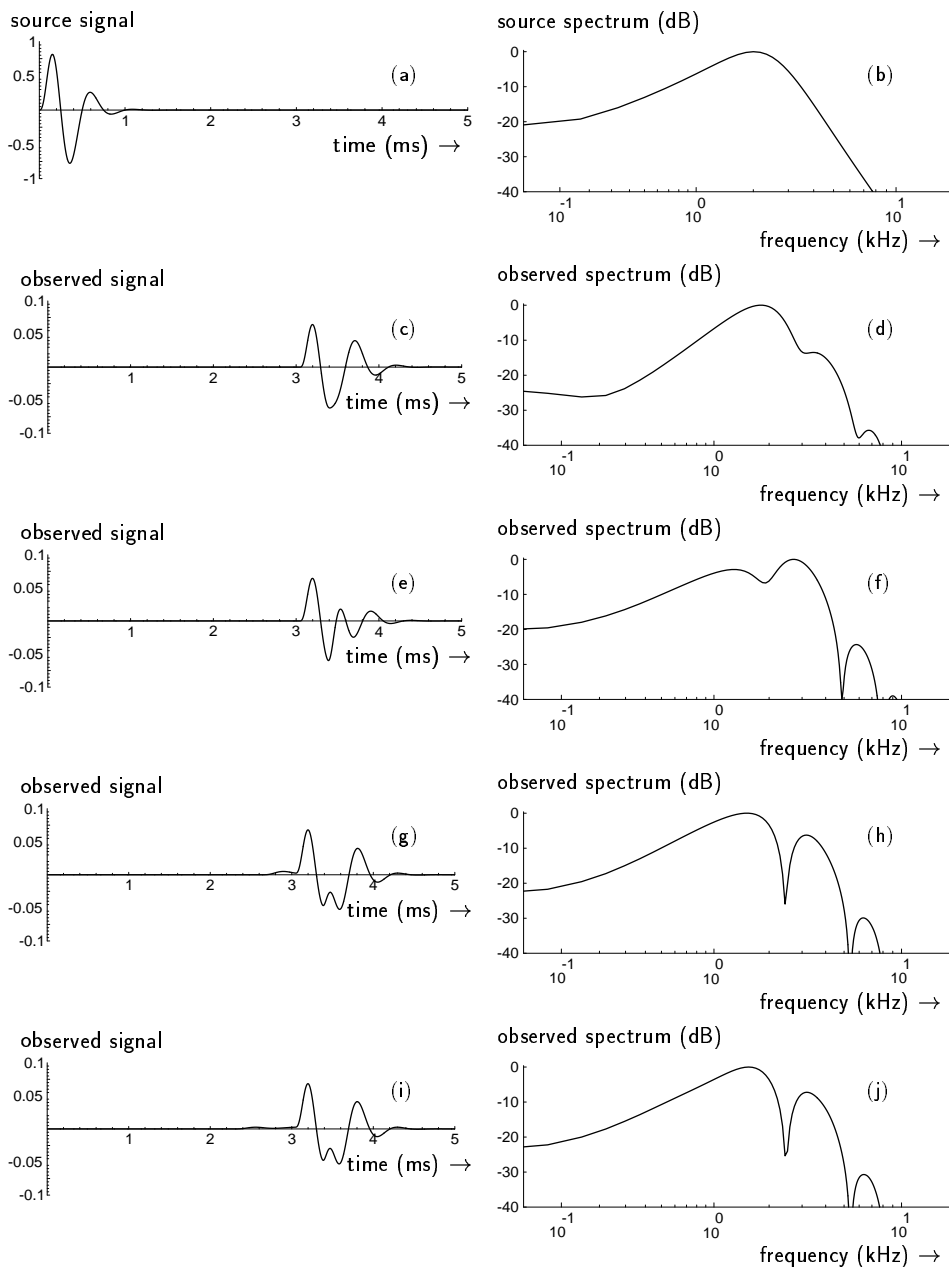


Figure 6.9: Caption on previous page

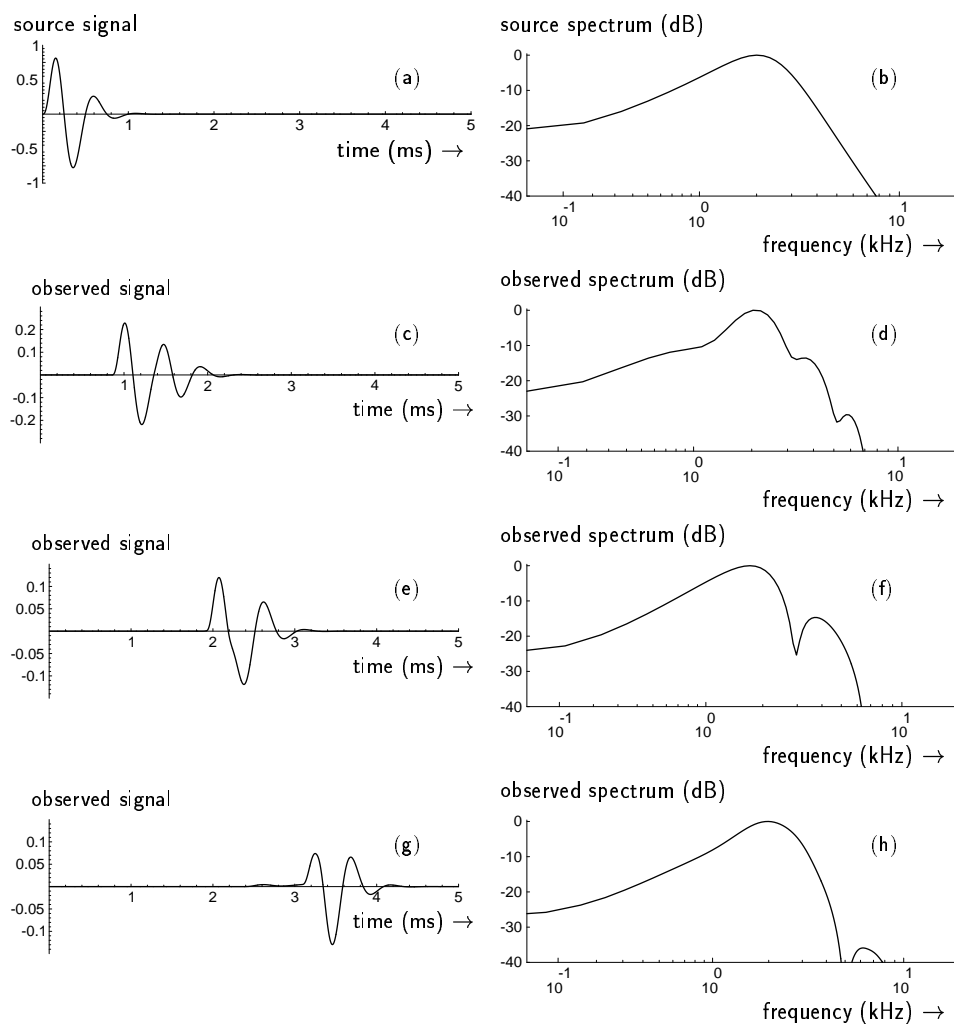


Figure 6.10: The source signal (a) and its normalized power spectral density (b). The observed signal and its corresponding power spectral density are shown for different observation points in the first medium. Observation point at  $r = 0.2$  m,  $z = 0.1$  m. The head-wave, direct-wave and body-wave arrival times are 1.35 ms, 0.86 ms, and 1.36 ms, respectively (c, d). Observation point at  $r = 0.6$  m,  $z = 0.1$  m. The head-wave, direct-wave and body-wave arrival times are 1.85 ms, 1.92 ms, and 2.19 ms, respectively (e, f). Observation point at  $r = 1.0$  m,  $z = 0.1$  m. The head-wave, direct-wave and body-wave arrival times are 2.35 ms, 3.09 ms, and 3.26 ms, respectively (g, h). In all cases  $c_1 = 330$  m/s,  $c_2 = 800$  m/s. The source is located at  $r = 0$  m,  $z = 0.3$  m. Its parameters are those of Fig. 6.9.

The dependence of the observed power spectrum on the position of the point of observation is illustrated in Fig. 6.10. In this example the source signal and its power spectrum are again those of Fig. 6.9. Upon changing the point of observation, the arrival times of the direct, head, and body-wave are altered. Also, the time delay between them changes. Even for an observation point relatively close to the source (c, d) the observed power spectrum already differs significantly from the source spectrum. When the point of observation is moved away from the source, the onset of the head-wave takes place earlier (e, g), and the observed spectra (f, h) deviate even more from the emitted spectrum (b).

We emphasize that the spectral changes that we have calculated cannot be attributed to any of the four other mechanisms that are mentioned in Section 5.1 but are purely reflection-induced.

### **6.3 Conclusions**

We have calculated the effect of reflection on the field of a pulsed point source using the modified Cagniard technique. It is found that the observed power spectrum can differ significantly from the power spectrum that is emitted by the source. Both its shape and the position of its maximum alter. The observed spectrum depends strongly on the wavespeed of the medium in which the source is embedded and the one of the half-space at which the field is reflected. Also, the location of the point of observation affects the spectrum.

### **Acknowledgements**

The second author wishes to thank Hans van den Berg of Wageningen University and Bert Jan Kooij of Delft University of Technology for stimulating discussions.

## Bibliography

- B.B. BAKER AND E.T. COPSON, *The Mathematical Theory of Huygens' Principle*, Second edition (Clarendon Press, Oxford, 1950).
- J. VAN BLADEL, *Relativity and Engineering* (Springer, Berlin, 1984). See, in particular, Chapter 5.
- M.F. BOCKO, D.H. DOUGLASS AND R.S. KNOX, "Observation of Frequency Shifts of Spectral Lines Due to Source Correlations", *Phys. Rev. Lett.* **58**, pp. 2649–2651 (1987).
- A. BOIVIN AND E. WOLF, "Electromagnetic field in the neighborhood of the focus of a coherent beam", *Phys. Rev.* **138**, pp. B1561–B1565 (1965).
- A. BOIVIN, J. DOW AND E. WOLF, "Energy flow in the neighborhood of the focus of a coherent beam", *J. Opt. Soc. Am.* **57**, pp. 1171–1175 (1967).
- M. BORN AND E. WOLF, *Principles of Optics*, Sixth edition (Cambridge University Press, Cambridge, 1997).
- M. BORN AND E. WOLF, *Principles of Optics*, Seventh (expanded) edition (Cambridge University Press, Cambridge, 1999).
- C.J. BOUWKAMP, "Diffraction theory", *Rep. Prog. Phys.* **17**, pp. 35–100 (1954).
- L. CAGNIARD, *Ondes Séismiques Progressives* (Gauthier-Villars, Paris, 1939). Translated and revised by E.A. Flinn and C.H. Dix as *Reflection and Refraction of Progressive Seismic Waves* (McGraw-Hill, New York, 1962).

- S. CHANG, J.H. JO AND S.S. LEE, "Theoretical calculations of optical force exerted on a dielectric sphere in the evanescent field generated with a totally-reflected focused gaussian beam," *Opt. Comm.* **108**, pp. 133–143 (1994).
- P. DEBYE, "Das Verhalten von Lichtwellen in der Nähe eines Brennpunktes oder einer Brennlinie", *Ann. der Phys.* **30**, pp. 755–776 (1909).
- V. DHAYALAN, PhD thesis, University of Bergen, Norway (1996).
- V. DHAYALAN AND J.J. STAMNES, "Focusing of electromagnetic waves into a dielectric slab I: Exact and asymptotic results", *Pure Appl. Opt.* **7**, pp. 33–52 (1998).
- G.W. FARNELL, "On the axial phase anomaly for microwave lenses", *J. Opt. Soc. Am.* **48**, pp. 643–647 (1958).
- X. GAN, C.J.R. SHEPPARD AND M. GU, "Effects of Fresnel diffraction on confocal imaging with an annular lens", *Bioimaging* **5**, pp. 153–158 (1997).
- J. GASPER ET AL., "Reflection and refraction of an arbitrary electromagnetic wave at a plane interface", *J. Opt. Soc. Am.* **66**, pp. 955–961 (1976).
- J.W. GOODMAN, *Introduction to Fourier Optics*, Second edition, Sec. 3.6.
- J.H.M.T. VAN DER HIJDEN, *Propagation of transient elastic waves in stratified anisotropic media* (North-Holland, Amsterdam, 1987).
- A.T. DE HOOP, "A modification of Cagniard's method for solving seismic pulse problems", *Appl. Sci. Res.* **B 8**, pp. 349–356 (1960).
- A.T. DE HOOP AND H.J. FRANKENA, "Radiation of pulses generated by a vertical electric dipole above a plane, non-conducting, Earth", *Appl. Sci. Res. B 8*, pp. 369–377 (1960).
- A.T. DE HOOP, "Pulsed electromagnetic radiation from a line source in a two-media configuration", *Radio Science* **14**, pp. 253–268 (1979).

- A.T. DE HOOP AND J.H.M.T. VAN DER HIJDEN, "Generation of acoustic waves by an impulsive line source in a solid/fluid configuration with a plane boundary", *J. Acoust. Soc. Am.* **74**, pp. 333–342 (1984a).
- A.T. DE HOOP AND J.H.M.T. VAN DER HIJDEN, "Generation of acoustic waves by an impulsive point source in a solid/fluid configuration with a plane boundary", *J. Acoust. Soc. Am.* **75**, pp. 1709–1715 (1984b).
- A.T. DE HOOP AND J.H.M.T. VAN DER HIJDEN, "Seismic waves generated by an impulsive point source in a solid/fluid configuration with a plane boundary", *Geophysics* **50**, pp. 1083–1090 (1985).
- A.T. DE HOOP, *Handbook of Radiation and Scattering of Waves* (Academic Press, London, 1995), Sections 2.6 and 5.4.
- A.T. DE HOOP, S. ZEROUG AND S. KOSTEK, "Transient analysis of the transmitting properties of a focused acoustic transducer with an arbitrary rim", *J. Acoust. Soc. Am.* **98**, pp. 1767–1777 (1995).
- CHR. HUYGENS, *Traité de la lumière* (Van der Aa, Leyden, 1690).
- D. JIANG AND J.J. STAMNES, "Theoretical and experimental results for two-dimensional electromagnetic waves focused through an interface", *Pure Appl. Opt.* **7**, pp. 627–641 (1998).
- B. KARCZEWSKI AND E. WOLF, "Comparison of three theories of electromagnetic diffraction at an aperture. Pt. I: Coherence matrices", *J. Opt. Soc. Am.* **56**, pp. 1207–1214 (1966a).
- B. KARCZEWSKI AND E. WOLF, "Comparison of three theories of electromagnetic diffraction at an aperture. Part II: The far field", *J. Opt. Soc. Am.* **56**, pp. 1214–1219 (1966b).
- G.P. KARMAN, M.W. BEIJERSBERGEN, A. VAN DUIJL AND J.P. WOERDMAN, "Creation and annihilation of phase singularities in a focal field", *Opt. Lett.* **22**, pp. 1503–1505 (1997).
- F. KOTTLER, in: *Progress in Optics*, Vol. IV, E. Wolf (ed.), pp. 283–314 (North-Holland, Amsterdam, 1965).

- F. KOTTLER, in: *Progress in Optics*, Vol. VI, E. Wolf (ed.), pp. 333–377 (North-Holland, Amsterdam, 1967).
- Y. LI AND E. WOLF, “Focal shifts in diffracted converging spherical waves”, *Opt. Comm.* **39**, pp. 211–215 (1981).
- Y. LI AND E. WOLF, “Focal shift in focused truncated gaussian beams”, *Opt. Comm.* **42**, pp. 151–156 (1982).
- Y. LI AND H. PLATZER, “An experimental investigation of diffraction patterns in low-Fresnel-number focusing systems”, *Opt. Acta* **30**, pp. 1621–1643 (1983).
- Y. LI AND E. WOLF, “Three-dimensional intensity distribution near the focus in systems of different Fresnel numbers”, *J. Opt. Soc. Am. A* **1**, pp. 801–808 (1984).
- Y. LI, “Three-dimensional intensity distribution in low-Fresnel-number focusing systems”, *J. Opt. Soc. Am. A* **4**, pp. 1349–1353 (1987).
- H. LING AND S-W. LEE, “Focusing of electromagnetic waves through a dielectric interface”, *J. Opt. Soc. Am. A* **1**, pp. 965–973 (1984).
- R.K. LUNEBURG, *Mathematical Theory of Optics*, Second edition (University of California Press, Berkeley, 1964), Chap. VI, pp. 319–323.
- H. MAECKER, “Quantitativer Nachweis von Grenzschichtwellen in der Optik”, *Ann. Physik* 6. Folge, Bd. 4, pp. 28–42 (1949).
- E.W. MARCHAND AND E. WOLF, “Boundary diffraction wave in the domain of the Rayleigh–Kirchhoff diffraction theory”, *J. Opt. Soc. Am.* **52**, pp. 761–767 (1962).
- E.W. MARCHAND AND E. WOLF, “Consistent formulation of Kirchhoff’s diffraction theory”, *J. Opt. Soc. Am.* **56**, pp. 1712–1722 (1966).
- L. MANDEL AND E. WOLF, *Optical Coherence and Quantum Optics* (Cambridge University Press, Cambridge, 1995).

- L. MINTROP, *Mitteilungen der Seismos-Gesellschaft II, Zur Geschichte des seismischen Verfahrens zur Erforschung von Gebirgsschichten und nutzbaren Lagerstätten* (Seismos, Hannover, 1930).
- NAG Fortran Library Mark 17, Numerical Algorithm Group Ltd., Oxford, UK.
- S. NEMOTO, “Waist shift of a Gaussian beam by plane dielectric interfaces”, *Appl. Opt.* **27**, pp. 1833–1839 (1988).
- K.E. OUGHSTUN AND G.C. SHERMAN, *Electromagnetic Pulse Propagation in Causal Dielectrics* (Springer, Berlin, 1997).
- B. RICHARDS AND E. WOLF, “Electromagnetic diffraction in optical systems. II. Structure of the image field in an aplanatic system,” *Proc. Roy. Soc. London Ser. A* **253**, pp. 358–379 (1959).
- H. SEVERIN, “Zur Theorie der Beugung elektromagnetischer Wellen”, *Z. Phys.* **129**, pp. 426–439 (1951).
- C.J.R. SHEPPARD AND P. TÖRÖK, “Effects of specimen refractive index on confocal imaging”, *J. Microscopy* **185**, pp. 366–374 (1997).
- C.J.R. SHEPPARD AND M. GU, “Aberration compensation in confocal microscopy”, *Appl. Opt.* **30**, pp. 3563–3568 (1991).
- S. SILVER, “Microwave aperture antennas and diffraction theory”, *J. Opt. Soc. Am.* **52**, pp. 131–139 (1962).
- W.R. SMYTHE, “The double current sheet in diffraction”, *Phys. Rev.* **72**, pp. 1066–1070 (1947).
- A. SOMMERFELD, *Optics* (Academic Press, New York, 1954), Chap. V, p. 200.
- J.J. STAMNES, *Waves in Focal Regions* (Adam Hilger, Bristol, 1986).
- J.J. STAMNES AND B. SPJELKAVIK, “Focusing at small angular apertures in the Debye and Kirchhoff approximations”, *Opt. Comm.* **40**, pp. 81–85 (1981).

- J.J. STAMNES AND D. JIANG, “Focusing of two-dimensional electromagnetic waves through a plane interface”, *Pure Appl. Opt.* **7**, pp. 603–625 (1998).
- J.A. STRATTON AND L.J. CHU, “Diffraction theory of electromagnetic waves”, *Phys. Rev. B* **56**, pp. 99–107 (1939).
- J.A. STRATTON, *Electromagnetic Theory* (McGraw-Hill, New York, 1941).
- G. TORALDO DI FRANZIA, *Electromagnetic Waves* (Interscience Publishers Inc., New York, 1955).
- P. TÖRÖK, G.R. BOOKER, Z. LACZIK AND R. FALSTER, “A new confocal SIRM incorporating reflection, transmission and double-pass modes either with or without differential phase contrast imaging”, *Inst. Phys. Conf. Ser.* **134**, pp. 771–774 (1993).
- P. TÖRÖK, P. VARGA, Z. LACZIK AND G.R. BOOKER, “Electromagnetic diffraction of light focused through a planar interface between materials of mismatched refractive indices: an integral representation”, *J. Opt. Soc. Am. A* **12**, pp. 325–332 (1995a).
- P. TÖRÖK, P. VARGA AND G. NÉMETH, “Analytical solution of the diffraction integrals and interpretation of wave-front distortion when light is focused through a planar interface between materials of mismatched refractive indices”, *J. Opt. Soc. Am. A* **12**, pp. 2660–2672 (1995b).
- P. TÖRÖK, C.J.R. SHEPPARD AND P. VARGA, “Study of evanescent waves for transmission near-field optical microscopy”, *J. Mod. Opt.* **43**, pp. 1167–1183 (1996a).
- P. TÖRÖK, P. VARGA, A. KONKOL AND G.R. BOOKER, “Electromagnetic diffraction of light focused through a planar interface between materials of mismatched refractive indices: structure of the electromagnetic field II”, *J. Opt. Soc. Am. A* **13**, pp. 2232–2238 (1996b).

- P. TÖRÖK, S.J. HEWLETT AND P. VARGA, “The role of specimen-induced spherical aberration in confocal microscopy”, *J. Microscopy* **188**, Part II, pp. 158–172 (1997).
- T.D. VISSER AND S.H. WIERSMA, “Spherical aberration and the electromagnetic field in high aperture systems”, *J. Opt. Soc. Am. A* **8**, pp. 1404–1410 (1991).
- T.D. VISSER AND S.H. WIERSMA, “Diffraction of converging electromagnetic waves”, *J. Opt. Soc. Am. A* **9**, pp. 2034–2047 (1992).
- T.D. VISSER AND J.L. OUD, “Volume measurements in 3-D microscopy”, *Scanning* **16**, pp. 198–200 (1994).
- I.A. WALMSLEY, “Measuring ultrafast optical pulses using spectral interferometry”, *Optics and Photonics News* **10**, No. 4, pp. 28–33 (1999), and references therein.
- D.V. WIDDER, *The Laplace Transform* (Princeton University Press, Princeton, 1946).
- S.H. WIERSMA AND T.D. VISSER, “Defocusing of a converging electromagnetic wave by a plane dielectric interface”, *J. Opt. Soc. Am. A* **13**, pp. 320–325 (1996).
- S.H. WIERSMA, P. TÖRÖK, T.D. VISSER AND P. VARGA, “Comparison of different theories for focusing through a plane interface”, *J. Opt. Soc. Am. A* **14**, pp. 1482–1490 (1997).
- E. WOLF, “Electromagnetic diffraction in optical systems I. An integral representation of the image field”, *Proc. Roy. Soc.* **253**, pp. 349–357 (1959).
- E. WOLF, “Non-cosmological redshifts of spectral lines”, *Nature* **326**, pp. 363–365 (1987).
- E. WOLF AND Y. LI, “Conditions for the validity of the Debye integral representation of focused fields”, *Opt. Comm.* **39**, pp. 205–210 (1981).

- E. WOLF AND D.F.V. JAMES, "Correlation-induced spectral changes",  
Rep. Prog. Phys. **59**, pp. 771–818 (1996).

## Samenvatting (summary in Dutch)

De Nederlandse titel van dit proefschrift luidt: “Focusering van elektromagnetische golven.” Focuseren is het concentreren van een uitgebreide bundel in een zo klein mogelijk gebied achter de lens. De eerste (scalaire) theoretische verhandeling hierover dateert van het begin van de vorige eeuw. Later zijn er meerdere theorieën opgesteld, ieder met hun eigen benaderingen en geldigheidsgebieden. Een belangrijke uitbreiding vormde de formulering van een elektromagnetische beschrijving in plaats van een scalaire. Voor moderne toepassingen met grote openingshoeken is een elektromagnetische beschrijving van het focuseren onontbeerlijk. Alle theorieën tot nu toe nemen aan dat het focuseren plaatsvindt in één medium (bijvoorbeeld lucht). In de praktijk is het eerder regel dan uitzondering dat het focuseren van elektromagnetische golven in een tweede medium plaatsvindt. Het is het doel van dit proefschrift om een beschrijving te geven van de effecten die optreden als er door een grensvlak van twee media heen wordt gefocuseerd.

Het focuseren door een grensvlak van twee media roept enkele belangrijke complicaties op. Allereerst wordt de intensiteit verminderd omdat er verliezen optreden als gevolg van reflectie aan het grensvlak (typisch verdisconteerd door de Fresnel coëfficiënten). Belangrijker nog, omdat de golven uit verschillende richtingen verschillende optische weglengtes afleggen door het tweede medium, zal er geen sprake meer zijn van een scherp focus maar veeleer van een gebied waarover de intensiteit wordt uitgesmeerd. De resultaten behaald in dit proefschrift zijn van belang voor verschillende toepassingen. Men denke bijvoorbeeld aan microscopie, “optical recording”, en “optical trapping”. In deze toepassingen is een scherp gedefinieerde piek van hoge intensiteit gewenst. Kennis van de eigenschappen en structuur van de verdeling van de intensiteit in het focale gebied is

dan ook van grote betekenis.

In Hoofdstuk 2 wordt het focale gebied bestudeerd van een bundel die door een grensvlak wordt gefocuseerd. Voor punten op de optische as wordt de elektrische energiedichtheid bepaald. Om de structuur van dit gebied nader te bekijken wordt ook voor enkele vlakken loodrecht op de optische as de energiedichtheid berekend. Het blijkt dat de doorgang door het grensvlak een aanzienlijke verbreding geeft van het diffractiepatroon, en als gevolg daarvan een sterk gereduceerde pieksterkte. Tevens is de symmetrie rond het focus, die we wel vinden bij het focuseren in één medium, verdwenen.

Hoofdstuk 3 bevat een vergelijking tussen twee recente theorieën over focusering door een grensvlak, nl. die van Hoofdstuk 2 en een praktisch gelijktijdig gepubliceerde van Török *et al.* Beide theorieën hebben verschillende uitgangspunten. Niettemin lopen de voorspellingen nauwelijks uiteen.

Een geometrisch-optische analyse (waarbij het golfkarakter van het licht wordt genegeerd) leert dat er een gebied wordt gedefinieerd op de optische as waarin het licht terechtkomt. De grenzen van dit gebied, de zogenaamde schaduwgrenzen, geven een verrassend goede indicatie van de breedte van het diffractiepatroon zoals dat door een volledig elektromagnetische behandeling voorspeld wordt. Het diffractiepatroon van de elektromagnetische theorie en de intensiteitsverdeling van de geometrisch-optische aanpak stemmen goed overeen. Met name de positie van de piek kan door de laatste met een redelijke nauwkeurigheid bepaald worden.

In 3-D afbeeldingstechnieken wordt vaak verondersteld dat de verplaatsing van de lens en de corresponderende verschuiving van het interferentiepatroon gelijk zijn. Dit is echter niet het geval. Een relatie wordt afgeleid tussen deze twee afstanden waarmee gerapporteerde anomalieën in volumemetingen verklaard worden.

Na vastgesteld te hebben hoe het diffractiepatroon eruit ziet wordt in Hoofdstuk 4 uitgelegd hoe het effect van het grensvlak geminimaliseerd kan worden, daarmee tegemoetkomend aan de eerder genoemde wens van een scherp focus. Er wordt een ringvormige belichting voorgesteld. Dit zou de grootte van het diffractiepatroon moeten beperken; immers, er zijn nu alleen golven in het spel die veel minder van elkaar in optische weglengte verschillen dan in het geval van een volledige belichting. Dit blijkt ook inderdaad het geval. Dorr middel van de methode van stationaire fase kan de

juiste ringvormige belichting bepaald worden. Daarmee is het nu mogelijk om het diffractiepatroon van de vele secondaire maxima te ontdoen en de maximale intensiteit op een willekeurig punt op de optische as (mits binnen de eerder genoemde schaduwgrenzen) te projecteren. Door de ring continu van grootte en positie te variëren is het tevens mogelijk om een maximale intensiteit – nu bestaande uit een enkele piek – door het tweede medium te *scannen*. Deze maximale intensiteit verschilt echter wel van punt tot punt. Correctie hiervoor d.m.v. een variatie van de output van de lichtbron zou het mogelijk maken om een optimale *constante* piekintensiteit door het tweede medium te bewegen. Dit nieuwe scanningmechanisme kan toegepast worden in lithografie en confocale microscopie.

Een ander aspect van de aanwezigheid van een grensvlak wordt besproken in de Hoofdstukken 5 en 6. De situatie is als volgt. Een punt boven het grensvlak zendt een (akoestische) puls uit. In een observatiepunt eveneens boven het grensvlak wordt bekeken hoe het signaal er uitziet in de tijd, en wordt het spectrum vergeleken met dat wat de puntbron uitzendt. Voor de analyse van dit probleem wordt gebruik gemaakt van de “gemodificeerde Cagniard methode.” Er zijn in principe drie bijdragen: direct waves, body-waves en head-waves. Direct waves zijn golven die rechtstreeks van bron naar observatiepunt reizen, zonder tussenkomst van het grensvlak. Deze zijn altijd aanwezig. De body-waves zijn de bijdragen die gevormd worden door de reflectie aan het grensvlak, en zijn ook altijd aanwezig. De head-waves treden alleen op als de golfsnelheid in het tweede medium groter is dan die van het eerste medium. Bovendien moet het observatiepunt ook geschikt gekozen worden. Deze golven propageren met de hogere snelheid van het tweede medium langs het grensvlak, en veroorzaken een vlak golf-front in het eerste medium. Door die hogere snelheid kunnen head-waves zelfs vóór de direct waves aankomen.

Het effect van dit samenspel van direct waves, body-waves en head-waves op het waargenomen spectrum is bestudeerd als functie van de snelheid in het tweede medium en de positie van het observatiepunt. Zeer grote verschillen met het uitgezonden spectrum worden voorspeld, die toenemen als de golfsnelheid in het tweede medium toeneemt t.o.v. die in het eerste medium, en als de afstand tussen bron en observatiepunt groter gekozen wordt.



# Dankwoord

Een woord van dank aan de mensen die betrokken zijn geweest bij de totstandkoming van dit proefschrift is hier op zijn plaats.

Dat een verzameling artikelen uiteindelijk de vorm van een proefschrift kon aannemen dank ik aan mijn promotor, Prof. Daan Lenstra. Het door hem gestelde vertrouwen heb ik als een flinke steun in de rug ervaren.

Bijzondere dank ben ik verschuldigd aan mijn co-promotor en vriend Taco Visser. Zijn energie en enthousiasme hebben mij op moeilijke ogenblikken er doorheen geholpen. De sessies met hem vormden voor mij een ijkpunt in de week. Een grote stimulans was zijn altijd cordiale begroeting “Dottore!”, die ik met een gepast “Maestro!” beantwoordde.

Mede-auteur Peter Török bedank ik voor zijn waardevolle bijdragen en de spreekwoordelijke Hongaarse zin voor gastvrijheid, die ons ten deel viel tijdens een bezoek aan zijn instituut in Cambridge. Het gerace over engelse binnenwegen in een klein autootje, bijna geheel gevuld door Peter’s gestalte, zal ik niet licht vergeten.

De Vrije Universiteit ben ik dank verschuldigd voor de gastvrijheid en de computerfaciliteiten mij geboden.

Tevens wil ik Arno Stobbe bedanken voor het ontwerpen en bouwen van een grafisch interface dat de (meeste) numerieke bewerkingen uit dit proefschrift op een PC mogelijk maakte. En verder natuurlijk om als kopvan-Jut te dienen aan de snookertafel.

Een woord van dank geldt ook Eric van der Steen. Zijn medewerking aan de technische realisatie van het omslag, en uiteraard onze samenwerking op heel andere terreinen dan de fysica, werd en wordt bijzonder op prijs gesteld.

En natuurlijk Alison. Zij kwam precies op tijd in mijn leven en heeft mij de tijd en ruimte gegeven om dit avontuur tot een goed einde te brengen.

Tenslotte wil ik onze kleine Alice niet onvermeld laten. Hoewel de wet van Lenz (ieder gevolg werkt de oorzaak van zijn ontstaan tegen) ook hier geldt, heeft zij, 'in blissful ignorance', ons leven (nog) meer inhoud gegeven.